MICROCOPY RESOLUTION TEST CHART

NATIONAL BUREAU OF STANDARDS-1963-A

FOR

AEROSPACE STUDIES

UNIVERSITY OF TORONTO

REPORT DOCUMENTATION PAGE

1a. REPORT SECURITY CLASSIFICATION Unclassified	**1b. RESTRICTIVE MARKINGS**
2a. SECURITY CLASSIFICATION AUTHORITY	**3. DISTRIBUTION/AVAILABILITY OF REPORT** Unlimited.
2b. DECLASSIFICATION/DOWNGRADING SCHEDULE	

4. PERFORMING ORGANIZATION REPORT NUMBER(S) UTIAS TN No. 256	**5. MONITORING ORGANIZATION REPORT NUMBER(S)** AFOSR·TR· 8 6 - 2 0 2 9

6a. NAME OF PERFORMING ORGANIZATION University of Toronto, Inst. for Aerospace Studies	**6b. OFFICE SYMBOL** *(If applicable)*	**7a. NAME OF MONITORING ORGANIZATION** AFOSR
6c. ADDRESS *(City. State and ZIP Code)* 4925 Dufferin St., Downsview, Ontario, Canada, M3H 5T6		**7b. ADDRESS** *(City. State and ZIP Code)* Same as 8c

8a. NAME OF FUNDING/SPONSORING ORGANIZATION Air Force Office of Scientific Research/NA	**8b. OFFICE SYMBOL** *(If applicable)* NA	**9. PROCUREMENT INSTRUMENT IDENTIFICATION NUMBER** AF-AFOSR-82-0096

8c. ADDRESS *(City. State and ZIP Code)* Bldg. 410, Bolling Air Force Base, DC 20332, U.S.A.	**10. SOURCE OF FUNDING NOS.**			
	PROGRAM ELEMENT NO.	**PROJECT NO.**	**TASK NO.**	**WORK UNIT NO.**
11. TITLE *(Include Security Classification)* An Interferometric Investigation of the	$61102F$	2307	$A1$	

12. PERSONAL AUTHOR(S) John Wheeler	Regular to Mach Reflection Transition Boundary in Pseudostationary Flow in Air

13a. TYPE OF REPORT Interim	**13b. TIME COVERED** FROM _____ TO _____	**14. DATE OF REPORT** *(Yr.. Mo.. Day)* April 1986	**15. PAGE COUNT** 150

16. SUPPLEMENTARY NOTATION

17. COSATI CODES			**18. SUBJECT TERMS** *(Continue on reverse if necessary and identify by block number)*
FIELD	**GROUP**	**SUB. GR.**	1. Pseudostationary oblique shock-wave reflections
			2. Regular-to-Mach reflection transition
			3. Nonstationary boundary-layer effects (Contd. on reverse)

19. ABSTRACT *(Continue on reverse if necessary and identify by block number)*

The regular (RR) to Mach reflection (MR) transition boundary in pseudostationary flow in air was investigated, with emphasis on the influence of the shock-induced boundary layer. Nearly 100 experiments were conducted in the region of the RR ↔ MR transition line over a range of incident-shock-wave Mach number $1.1 < M_s < 6.5$ by conducting experiments in the UTIAS 10 x 18 cm Hypervelocity Shock Tube. The wedge angles used were $42°$, $45°$, $47°$, and $48°$. Initial pressures were kept as low as possible to maximize viscous effects and ranged from 0.4 kPa to 100 kPa. A comparison was made between the boundary-layer thickness, and the deviation of the transition boundary from inviscid theory. This difference is often called the 'von Neumann paradox'.

(Continued on reverse.)

20. DISTRIBUTION/AVAILABILITY OF ABSTRACT	**21 ABSTRACT SECURITY CLASSIFICATION**
UNCLASSIFIED/UNLIMITED ☒ SAME AS RPT. ☒ DTIC USERS ☐	Unclassified

22a. NAME OF RESPONSIBLE INDIVIDUAL Dr. JAMES D. WILSON	**22b. TELEPHONE NUMBER** *(Include Area Code)* 767-4935	**22c. OFFICE SYMBOL** AFOSR/NA

18. Subject Terms (Continued)

4. Shock-tube flows   5. Interferometric measurements
6. 'von Neumann paradox'

19. Abstract (Continued)

It was found that the 'von Neumann paradox' was due to viscous effects. The deviation of the RR ↔ MR transition line from the 'detachment' criterion boundary was found to increase with a drop in initial pressure, in a manner consistent with boundary-layer theory. The effect of the endwall boundary layer on the RR ↔ MR transition line was more pronounced at low Mach number ($M_s < 2$), and a model is proposed to explain this behavior.

Initial pressure was also found to influence the height of the Mach stem in MR. Lower initial pressure (and hence greater viscous effects) reduced the height of the Mach stem, which was found to be smaller than the inviscid prediction in all MR experiments. An explanation for the reduction in Mach stem height is suggested, but the cause was not thoroughly investigated.

AN INTERFEROMETRIC INVESTIGATION

OF THE REGULAR TO MACH REFLECTION TRANSITION BOUNDARY

IN PSEUDOSTATIONARY FLOW IN AIR

by

John Wheeler

Submitted October 1985

ACKNOWLEDGEMENTS

ii

SUMMARY

The regular (RR) to Mach reflection (MR) transition boundary in pseudostationary flow in air was investigated, with emphasis on the influence of the shock-induced boundary layer. Nearly 100 experiments were conducted in the region of the RR↔MR transition line over a range of incident-shock-wave Mach number $1.1 < M_s < 6.5$ by conducting experiments in the UTIAS 10 x 18 cm Hypervelocity Shock Tube. The wedge angles used were 42°, 45°, 47°, and 48°. Initial pressures were kept as low as possible to maximize viscous effects and ranged from 0.4 kPa to 100 kPa. A comparison was made between the boundary-layer thickness, and the deviation of the transition boundary from inviscid theory. This difference is often called the 'von Neumann paradox'.

It was found that the 'von Neumann paradox' was due to viscous effects. The deviation of the RR↔MR transition line from the 'detachment' criterion boundary was found to increase with a drop in initial pressure, in a manner consistent with boundary-layer theory. The effect of the endwall boundary layer on the RR↔MR transition line was more pronounced at low Mach number ($M_s < 2$), and a model is proposed to explain this behavior.

Initial pressure was also found to influence the height of the Mach stem in MR. Lower initial pressure (and hence greater viscous effects) reduced the height of the Mach stem, which was found to be smaller than the inviscid prediction in all MR experiments. An explanation for the reduction in Mach stem height is suggested, but the cause was not thoroughly investigated.

TABLE OF CONTENTS

NOTATION

a   speed of sound in a gas

CMR   complex-Mach reflection

DMR   Double-Mach reflection

$f(\eta)$ boundary-layer velocity-distribution function

I   incident shock wave

k   thermal conductivity

kPa   kilopascal

K   kink, degrees Kelvin

l   length

L   horizontal distance from wedge corner

M   Mach stem

M_i Mach number in region (i)

MR   Mach reflection

p_i pressure in region (i)

P   reflection point in regular reflection (RR)

Pr   Prandtl number

$r(\eta)$ boundary-layer temperature-distribution function for adiabatic wall

R   reflected shock wave

R'   second reflected shock wave in double-Mach reflection

$s(\eta)$ boundary-layer temperature-distribution function for nonadiabatic wall

S   slipstream or contact surface

SMR   single-Mach reflection

t   time

T   triple point

T'   second triple point in double-Mach reflection

T_i	temperature in region (i)
u	flow velocity in the x-direction
U_i	flow speed in region (i)
v	flow velocity in the y-direction
$\mathring{A}$	Angstrom
γ	specific heat ratio
δ	angle between the incident and reflected shock waves
δ	boundary-layer thickness based on 99% freestream velocity
δ^*	boundary-layer displacement thickness
η	non-dimensional boundary-layer coordinate
θ_{bl}	boundary-layer flow entry angle
θ_i	flow-deflection angle through the shock wave when entering region (i)
θ_m	maximum possible flow-deflection angle through a shock wave
θ_s	flow-deflection angle through a shock wave which results in sonic flow behind shock
θ_v	characteristic vibrational temperature
λ	wavelength of light
μ	absolute viscosity
ν	kinematic viscosity
ρ	density
τ	shear stress, vibrational relaxation time
ϕ_i	incidence angle between the flow and shock wave in region (i)
χ	triple-point trajectory angle
χ'	second triple-point trajectory angle
ψ	stream function
ω'	reflected-shock-wave angle
Ω	boundary-layer flow entry angle at nominal distance x = 1 mm

Subscripts

0,1,2,3	thermodynamic regions
c	characteristic
e	external, freestream
exp	experimental
i	insulated
K	relative to kink
m	maximum
r	reference, rotational
s	shock, sonic
T	relative to triple point
t	translational
v	vibrational
w	wall

Superscripts

'	first-order derivative
''	second-order derivative
'''	third-order derivative

Chapter 1

INTRODUCTION

When energy is instantaneously released in a material, an explosion occurs and a shock wave is generated. The shock wave, which causes a sudden jump in pressure, temperature, and entropy, travels through the material as a result of molecular collisions. It loses strength by heating the material and raising its pressure as it races outward from the center of the explosion, and ultimately weakens to a sound wave.

If a planar shock wave intersects a wedge surface, four different reflection patterns can occur, depending on the strength of the shock and the wedge angle. The patterns are regular reflection (RR), single-Mach reflection (SMR), complex-Mach reflection (CMR), and double-Mach reflection (DMR) (see Figs. 1 to 4, from Ref. 30). The latter three as a group are called Mach reflection (MR). The four types have flow fields with different pressure, density and temperature distributions associated with them. The shock wave from an above-ground explosion in air would experience several of the reflection patterns as it intersected the ground on its travel outward [1,28].

There are many examples of both man-made and naturally occurring shock-wave phenomena [2]. In several of these, the process of oblique-shock-wave reflection is of great concern. For example, accurate prediction of the type of reflection and associated pressures is necessary for the design of shock-resistant structures. Applications range from chemical plants, where the potential for major explosions always exists, to mobile missile launchers which must be able to withstand a nuclear blast [3].

The study of oblique-shock-wave reflections began as far back as 1878 when Ernst Mach [4] did research on shock waves and observed RR and MR. In spite of this, it was not until the early 1940's that more thorough analytical and experimental work was done. At this time an analytical criterion for the transition from RR to MR in nonstationary flow (usually referred to as the 'detachment' criterion) was suggested by von Neumann [5,6].

Under the direction of Bleakney [7] a major study of nonstationary oblique-shock-wave reflection was carried out at Princeton University. Smith [8] did an extensive series of experiments and discovered SMR and CMR. He also found that RR persisted beyond the boundary predicted by the 'detachment' criterion. This persistence is often referred to as the 'von Neumann paradox'. Further experimentation by White [9] confirmed this persistence. White [9] also suggested a criterion for the transition from SMR to CMR, and discovered DMR, thus completing the identification of the four major types of oblique-shock-wave reflection. The most current analytical transition boundaries for inviscid frozen air are shown in Fig. 5.

Much work has been done since then in defining the regions of RR, SMR, CMR, and DMR. A study by Kawamura and Saito [10] again confirmed the persistence of RR into the predicted MR region for nonstationary flows. Gvozdeva et al [11] and Henderson and Lozzi [12] suggested criteria for the transition from SMR to CMR, and CMR to DMR but they were not substantiated. In the same study, Henderson and Lozzi [12] also offered the 'mechanical equilibrium' criterion for transition from RR to MR in nonstationary flows. Bazhenova et al [13] attempted to clarify experimentally the regions of RR, SMR, CMR, and DMR, but like other studies their range of Mach numbers and wedge angles was limited. Law and Glass [14] did experiments over a wider

range, and later Ben-Dor and Glass [15] established the generally accepted criteria for transition from SMR to CMR and CMR to DMR. A worthwhile additional necessary criterion for the SMR to CMR transition was later made by Shirouzu and Glass [16].

The necessary conditions for the transition from RR to MR in nonstationary flow are still not fully understood. Work by Hornung and Kychakoff [17] and Hornung, Oertel, and Sandeman [18] brought forth another hypothesis, the 'sonic' criterion. It is difficult to resolve experimentally from the 'detachment' criterion, and thus the 'von Neumann paradox' was still unsolved. It was suggested by Hornung et al [18] and later investigated by Hornung and Taylor [19] that the 'von Neumann paradox' was due to the viscous boundary layer which develops behind the shock on the wedge surface. Shirouzu and Glass [16] supported this theory but the evidence was still inconclusive.

Hornung and Taylor [19] investigated the influence of viscosity on the RR◄►MR transition boundary by doing experiments in argon. They held Mach number fixed, and varied the wedge angle to see the behavior of the size of Mach stem in MR. This was done for various initial pressures. They assumed transition to RR when the Mach stem size approached zero. Initial pressure was found to influence the position of the transition boundary.

It was the intent of this work to further explore the effect of the boundary layer on the RR◄►MR transition boundary, although from a different approach than Hornung and Taylor [19]. The approach taken here was to do experiments in air over a wide range of Mach numbers and initial pressures, and to find transition boundary points by doing both MR and RR experiments, in close proximity to the boundary.

In this investigation, the objectives were:

1. To determine precisely several RR↔MR transition boundary points by doing experiments very close to the boundary.

2. To use the lowest pressure possible to maximize viscous effects.

3. To obtain the deviation from inviscid theory of the reflected wave angle in RR at the RR↔MR transition boundary.

4. To predict the RR↔MR transition boundary in air for any initial pressure and incident-shock-wave Mach number.

The present research continues a long program of study of oblique-shock-wave reflection supervised by Professor I. I. Glass at the University of Toronto Institute for Aerospace Studies (UTIAS). Previous researchers include Molder [20], Weynants [21], Law and Glass [14], Ben-Dor [22], Ben-Dor and Glass [15,23], Ando [24], Ando and Glass [25], Lee and Glass [26], Shirouzu and Glass [16], Hu and Shirouzu [27], Hu [28], Deschambault [29], Deschambault and Glass [30], Hu and Glass [31,32] and Li and Glass [33].

Chapter 2

DESCRIPTION OF OBLIQUE-SHOCK-WAVE REFLECTION

In this chapter, the types of reflection and conditions associated with each are discussed for inviscid flow. The effects of viscosity on shock-wave reflection are treated in Chapter 3.

2.1 Dynamics of Oblique-Shock-Wave Reflection

When a shock wave passes over a wedge in a shock tube, two simultaneous processes occur [15]:

(a) deflection of the flow at the wedge corner, and

(b) reflection of the incident shock wave from the wedge surface.

The first of these, deflection at the corner, can take place via supersonic turning through an attached oblique shock wave (Fig. 6a,b), or subsonic turning with a detached shock wave (Fig. 6c). In the attached shock wave cases, the shock will be straight if the flow behind it is supersonic (Fig. 6a), or curved if the flow behind it is subsonic (Fig. 6b). The necessary conditions for each configuration are obtained from gasdynamics[34].

The reflection process can take place via RR, SMR, CMR, or DMR. The speed of the incident shock wave is constant. While there is some attenuation of the shock wave with time due to the wall boundary layer [36], it is not significant over very short wedge distances. The flow is pseudostationary, and consequently a frame of reference can be attached to the reflection point P in RR and the triple point T in MR. It can also be made self-similar by transforming the independent variables from x,y, and t to x/t and y/t [35]. Self-similarity makes the shock pattern and the flow-property distributions retain identical shapes, but increase in size linearly with time.

-5-

2.2 Types of Oblique-Shock-Wave Reflection

2.2.1 Regular Reflection (RR)

Regular reflection is shown schematically in Fig. 7. It is the simplest of the four types of reflection since it has only an incident shock wave I and a reflected shock wave R. The flow at reflection point P must remain parallel to the wedge. Therefore, the flow deflection through R must be equal and opposite to the deflection through I. This can be expressed as:

$$\theta_1 - \theta_2 = 0 \tag{2.1}$$

There are actually two possible solutions for the reflected-shock-wave angle, a strong and weak solution [34]. The weak solution is the only one which is usually found in practice. The simplicity of the shock configuration makes calculation of the flow properties fairly easy. Appendix A contains a description of the method of solution used by Hu and Shirouzu [27].

The reflected wave can be straight or curved near P depending upon the Mach number of the flow M_2 in region 2. If the flow in region 2 is supersonic, $M_2 > 1$, relative to P, the reflected wave must be straight since disturbances from the wedge corner can not propagate toward P (Fig. 8a). For subsonic flow, $M_2 < 1$, in region 2 relative to P, R will be curved (Fig. 8b) since disturbances are propagated from the corner to affect it.

2.2.2 Mach Reflection (MR)

Mach reflection is characterized by the appearance of a Mach stem M, and slipstream S (see Figs. 9 through 11). The necessary condition that flow remain parallel to the wedge surface implies that the Mach stem must be perpendicular to the wedge surface. The Mach stem often has some curvature [16], but is usually approximated as being straight for some analyses.

Consider the flow in the vicinity of triple point T. The flow can follow two paths; the first through regions 0, 1, and 2, and the second through regions 0 and 3. Regions 2 and 3 are separated by a contact surface or slipstream S. Across S, the pressures and flow direction must be equal, and the density, temperature, and entropy can differ. The boundary conditions are therefore:

$$\theta_1 - \theta_2 = \theta_3 \tag{2.2}$$

$$p_2 = p_3 \tag{2.3}$$

As mentioned previously, the flow at T can be considered pseudostationary, thus X remains constant as the shock travels up the wedge. The solution of MR is somewhat more difficult than for RR. Appendix A outlines the method of solution by Hu and Shirouzu [27], which also contains RR and MR solutions for a wide range of Mach number and wedge angle for various gases.

The unique properties of each type of Mach reflection are now described.

2.2.2.1 Single-Mach Reflection (SMR)

A schematic diagram of SMR is shown in Fig. 9. In SMR, unlike CMR and DMR, the reflected shock R is continuously curved from the triple point T to the wedge corner since the flow in region 2 is subsonic relative to T.

2.2.2.2 Complex-Mach Reflection (CMR)

Figure 10 shows a schematic diagram of CMR, which differs from SMR due to the appearance of a kink K in the reflected shock. The kink arises from a band of compression waves which converge on to the reflected shock at K [12].

-7-

The flow in region 2 is supersonic relative to T for CMR and DMR, and the reflected shock there is straight.

2.2.2.3 Double-Mach Reflection (DMR)

Figure 11 shows a schematic diagram of DMR, which differs from CMR due to the appearance of an additional Mach shock (stem) M' and slipstream S' at a new triple point T' (what used to be the kink K in CMR). The pattern of shock waves and slipstream is the same for both T and T'. By applying the gasdynamics equations in the same manner as for the solution at T, the flow velocities and states can also be solved for at T' [27].

2.3 Transition Criteria

2.3.1 RR⟷MR Transition

Several different criteria have been proposed for the transition from RR to MR. Each of these is now described.

2.3.1.1 'Detachment' Criterion

The 'detachment' criterion was proposed by von Neumann [5,6]. It stated that transition would occur when the flow deflection through the incident shock exceeded the maximum deflection possible, θ_{2m}, through the reflected shock (Fig. 7).

$$\theta_1 - \theta_{2m} = 0 \qquad (2.4)$$

At this point, the boundary condition of tangential flow at the wedge surface could no longer be satisfied with a RR or 'two-shock' configuration, and MR, a 'three-shock' configuration, would be necessary. This boundary is shown in Fig. 12.

Consider the shock polar [34] in Fig. 13. The shock polar is for a constant Mach number M_0 in region 0. The 'incident shock' curve represents all possible flow-pressure ratios in region 1 arising from a flow deflection θ_1 through an incident shock. Curves R1 to R5 represent possible flow-pressure ratios in region 2 after a deflection θ_2 through a reflected shock R. The 'Mach stem' curve represents possible states in region 3 arising from the flow through a Mach stem in MR. If any of the curves, R1 to R5, intersect the ordinate axis, RR is possible since the condition of no net deflection at the wedge surface is satisfied (Eq. 2.1). If any of the curves, R1 to R5, intersects the 'Mach stem' curve, then MR is possible, since the necessary conditions of equal pressure and flow direction in regions 2 and 3 are satisfied (Eqs. 2.2 and 2.3).

Five separate cases are represented by R1 to R5:

R1: Only RR is possible -- point a

R2: RR and MR possible -- point b

No net deflection, therefore X is equal to zero

for MR (Fig. 9)

R3: RR (pt. f) and MR (pt. c) both possible

R4: RR (pt. g) and MR (pt. d) both possible

Limit of RR reached

R5: Only MR is possible -- point e

The 'detachment' criterion states that as the wedge angle is decreased, the flow will follow path a-b-f-g (RR) and then jump back to d (MR). In effect it states that as wedge angle is decreased, with M_0 constant, RR will be maintained until it is no longer physically possible, and only then will MR occur. It should be noted that the jump from g to d has a sudden drop in pressure.

-9-

2.3.1.2 'Mechanical Equilibrium' Criterion

The 'mechanical equilibrium' criterion, which was proposed by Henderson and Lozzi [12], is shown in Fig. 12 for frozen air. They investigated the RR←→MR transition boundary in unsteady flow by reflecting shock waves from concave and convex wedge surfaces. During transition, both from RR to MR and MR to RR, neither unsteady expansion waves nor compression waves were seen. Some hysteresis was noted depending on whether transition was from RR to MR or MR to RR. Henderson and Lozzi [12] argued that the absence of unsteady expansion or compression waves implied that the transition process was steady, in 'mechanical equilibrium'. This criterion for transition was extended to the pseudosteady case, even though their experiments with flat wedge surfaces showed persistence of RR below the 'detachment' criterion boundary. These points which persisted into the MR region were presumed to be MR with Mach stems so small that they could not be seen.

On the shock polar diagram (Fig. 13) the 'mechanical equilibrium' criterion is represented by path a-b-c-d-e. Beginning at point a, as wedge angle is decreased the solution will continue to be one of RR. When point b is reached however, both RR and MR are possible. According to the criterion, points lying immediately on either side of the transition boundary should have the same flow-pressure ratio. Therefore, as wedge angle is further decreased, MR occurs and the flow is represented by points between b and c. As wedge angle is further decreased, the path goes to d and e.

At transition (point b):

$$\theta_1 - \theta_2 = \theta_3 = 0 \qquad (2.5)$$

-10-

By comparison, the 'detachment' criterion states that at b, when the wedge angle is further reduced, the flow remains as RR until point g is reached. Further reduction in wedge angle causes 'detachment' to occur and there is an immediate jump to point d, along with a sudden decrease in pressure ratio.

Many experimenters have shown RR to persist below the 'detachment' criterion boundary, which is well away from the 'mechanical equilibrium' boundary (Fig. 12). Some of Smith's data [8], which are quite extensive, clearly show the persistence of RR (Fig. 14). Some more recent data from Deschambault [29], which cover a wider range of Mach number, are shown in Fig. 15. It is the 'detachment' criterion that is now universally accepted for pseudostationary oblique-shock-wave reflection.

2.3.1.3 'Sonic' Criterion

Hornung and Kychakoff [17] and Hornung, Oertel, and Sandeman [18] proposed yet another theory, the 'sonic' criterion. From a physical point of view, they suggested that for a Mach stem to form, a length scale would have to arise as a result of signals transmitted from the wedge corner. For this to occur, the flow in region 2 relative to P in RR must be subsonic. This transition criterion is best expressed as:

$$\theta_1 - \theta_{2s} = 0 \qquad (2.6)$$

The boundary for this criterion is very close to that predicted by the 'detachment' criterion since the flow detachment angle θ_m and the sonic angle θ_s differ by only one or two degrees [34], and a resolution between the two is difficult to achieve experimentally.

Hornung et al [18] also hypothesized that the persistence of RR beyond the 'sonic' criterion boundary was due to the viscous boundary layer that is

-11-

induced behind the shock waves. Hornung and Taylor [19] later demonstrated that the transition boundary was affected by changes in initial pressure, in a relationship consistent with boundary-layer theory. However, their experiments were only for one particular Mach number in argon. A greater discussion of their work can be found in Chapter 3.

For the case of frozen air, a computer program was written to find the RR◄►MR transition boundary for any of the three transition criteria. This program is listed in Appendix B. The program contains provision for viscous effects, and can be easily modified to solve for any frozen gas. Its small size and simple construction makes it adaptable to microcomputers.

2.3.2 SMR◄►CMR Transition

The existence of CMR was first noticed by White [9] to occur when the Mach number in region 2 relative to the triple point was greater than one. This implies that transition may occur when:

$$M_{2_T} = 1 \tag{2.7}$$

A mechanism for the transition was proposed by Henderson and Lozzi [12] in terms of a band of compression waves. Law and Glass [14] and Ben-Dor and Glass [15] verified that transition occurs according to Eq. 2.7. Law and Glass [14] also predicted the location of the kink with the equation:

$$L_T / L_K = \rho_1 / \rho_0 \tag{2.8}$$

where L_T / L_K is the ratio of the horizontal distance from the wedge corner of T and K respectively (Fig. 16). Bazhenova et al [13], Ando and Glass [25], and Deschambault [29] found that this expression was not valid near the RR◄►MR boundary. They showed experimentally that the ratio approached unity.

An additional necessary criterion was added by Shirouzu and Glass [16]; that the angle between the incident and reflected shocks, δ, must exceed 90 degrees.

$$\delta > 90° \qquad (2.9)$$

This has been verified experimentally by Hu [28].

2.3.3 CMR◄►DMR Transition

Henderson and Lozzi [12] hypothesized that transition from CMR to DMR occurred when compression waves converged to form the second Mach stem, M' (Fig. 11). Supporting this idea, Law and Glass [14] and Ben-Dor and Glass [15] showed experimentally that transition occurred when the Mach number in region 2 relative to the kink equalled one:

$$M_{2_K} = 1 \qquad (2.10)$$

Chapter 3

INFLUENCE OF VIBRATIONAL EXCITATION AND VISCOSITY

3.1 Vibrational Excitation

At room temperatures, air behaves as a frozen gas. Only translational and rotational degrees of freedom are excited. For this frozen or perfect state, the specific heat ratio, γ, is constant, and the Rankine-Hugoniot relations (Ref. 34) can be applied for flow across a shock wave.

At high temperatures, occurring behind a strong shock wave, real-gas effects come into play. Vibrational excitation, dissociation, and ionization may be present. Dissociation and ionization occur only for very high Mach numbers [26], well outside the range of experiments in this study. As such, they will not be considered further.

To determine the effect of vibrational excitation, two things must be considered; the magnitude of excitation at equilibrium, and the rate at which equilibrium is approached.

3.1.1 Effect on the RR↔MR Boundary

At equilibrium, the extent of vibrational excitation depends only on temperature (see App. C). However, the relaxation length to equilibrium depends on the temperature and pressure of the gas. Oxygen is excited at a lower temperature than nitrogen. The effect of excitation of either constituent on the RR↔MR boundary is to lower it, as shown in Fig. 17.   It can be seen that the maximum effect of oxygen excitation occurs at $M_s \sim 6$, and the maximum effect of oxygen and nitrogen excitation occurs at $M_s \sim 10$. It was approximated that air consists of 20% oxygen and 80% nitrogen. A more detailed description of vibrational relaxation is contained in Appendix C.

For vibrational equilibrium, the flow across a shock wave does not have a closed-form solution as does a frozen flow. It must be solved numerically using the equations of continuity, momentum, energy, and the equation of state.

3.1.2 Role of Relaxation Length

Upon passing through a shock wave, the translational and rotational degrees of freedom are fully excited within a few mean free paths, the thickness of the shock. The vibrational degrees of freedom take much longer to reach equilibrium. The size of the relaxation zone is dependent on temperature and pressure (App. C).

To determine whether an assumption of frozen or equilibrium flow is appropriate, the relaxation length must be compared to a characteristic length of the region being studied behind the shock wave. If the relaxation length is much greater than the characteristic length, then the flow in the region of interest is in essence frozen. Conversely, if the relaxation length is much smaller than the characteristic length, then an assumption of equilibrium flow is more appropriate. Flows are considered in nonequilibrium where the relaxation length is of comparable size to the characteristic length, and must be treated in a more precise way.

3.2 Influence of Viscosity

3.2.1 Characteristics of Shock-Wave-Induced Boundary Layer

When a shock wave passes over a surface, it induces a velocity in the air behind the shock [36]. A boundary layer grows behind the shock wave, due to the friction between the moving air and the stationary wedge surface. This boundary layer has a significant effect on the flow at the

shock-wave-reflection point P. In a laboratory-fixed frame of reference, the flow velocity at the wall must be zero (Fig. 18a). It is convenient though, to attach the reference frame to the point where the shock intersects the surface (Fig. 18b). In this reference frame, the flow velocity at the wall must be that of the wall, relative to the shock. It should be noted that in this new shock-fixed reference frame, the boundary-layer displacement thickness, δ^*, has a negative value, or the wall acts as a sink. Instead of impeding the flow, the shear stress at the wall tends to 'sweep' the flow away from the shock wave.

The boundary-layer profile can be calculated by solving the transformed laminar-boundary-layer equations outlined by Mirels [37,38]. It will be shown later that the assumption of laminar flow is appropriate, based on the Reynolds number of the experiments performed. A summary of the equations used and method of solution is contained in Appendices D and E. Normalized velocity and temperature profiles are shown in Figs. 19 and 20 for the boundary layer behind a shock wave travelling at M_s = 2.0, at p_0 = 2 kPa and T_0 = 300 K. While the boundary-layer size is significantly affected by pressure, and to a lesser extent by temperature (see App. D), the shape of the profiles is scarcely influenced by either. Very rapid changes in velocity and temperature occur close to the wall. Half of the total change in velocity and temperature within the boundary layer occurs in the first 12% nearest the wall. It is interesting to note that the temperature and velocity profiles are quite similar, but at the outer edge of the boundary layer, the normalized temperature only reaches 0.98 compared to the normalized velocity of 0.99.

The most important thing about the equations is the dependence of the various size parameters on density or initial pressure, and the variation of boundary-layer size with distance from the shock wave.

-16-

The relationships are:

$$\delta,\ \delta^* \propto x^{\frac{1}{2}} \tag{3.1a}$$

$$\delta,\ \delta^* \propto \rho^{-\frac{1}{2}} \text{ or } p^{-\frac{1}{2}} \tag{3.1b}$$

This implies that if shock-wave reflection is influenced by viscous effects for a given gas, Mach number M_s and wedge angle θ_w are not sufficient to define the flow; initial pressure or density must also be specified. While viscosity may not have a great influence where the Reynolds number is high (high initial pressures), many shock-tube experiments are done at very low initial pressures where viscous effects are important.

3.2.2 Physical Model of the Reflection Process in RR with a Shock-Wave-Induced Boundary Layer

As noted before, many researchers have found significant differences between experiment and the 'detachment' criterion boundary, the 'von Neumann paradox' (Figs. 14 and 15). While this difference is one indication of possible viscous effects, additional information is gained by looking at the reflected wave angle in RR. If the wave angles near the reflection point P are measured off photographs from RR experiments, and the flow deflections through them calculated using the Rankine-Hugoniot equations, it is found that the flow deflection through the reflected wave R is not equal and opposite to that through the incident wave I. This difference in angles is defined as the displacement wedge angle, and is written as:

$$\theta_1 - \theta_2 = \theta_d \tag{3.2}$$

and is illustrated in Fig. 21. Displacement wedge angle, θ_d, is a measure of the deviation of RR experiments from inviscid theory.

-17-

Reflected wave angles ω' from RR experiments by Ben-Dor [22] and Deschambault [29] were obtained by remeasuring the angle δ between the incident and reflected shock waves at a distance of 1 mm from the reflection point P, and the results for displacement wedge angle θ_d are shown in Figs. 22 and 23 for $\theta_W = 50°$ and $60°$ respectively. Error in measurement should be quite small since the reflected wave R is straight in the vicinity of the reflection point P for these cases. Figure 22, which is for RR, has several theoretical curves corresponding to $\theta_d = 0°$, $1°$, and $2°$. The curve for $\theta_d = 0$ extends only up to $M_s = 1.8$, since for Mach numbers greater than this value and $\theta_W = 50°$, RR solutions do not exist. Similarily, for $\theta_d = 1°$, there are no RR solutions for $\theta_W = 50°$ in the range $2.1 < M_s < 3.4$. In Fig. 23, the curves cover the whole range of Mach number since RR solutions exist for all M_s when $\theta_W = 60°$.

In Fig. 22, where there is a great deal of data, the displacement wedge angle θ_d can be seen to increase as Mach number increases. In the most extreme case, for $M_s = 7.3$ and $\theta_W = 50°$, the displacement wedge angle θ_d exceeds $3°$. Concurrent with an increase in M_s, the experiments had lower initial pressures, and it is believed that this was the cause of the higher deviations. It is expected that the same phenomenon will influence the transition boundary. Figure 23 also shows a deviation from the inviscid prediction, but insufficient data makes trends indeterminate.

In a general sense, for both RR and MR, the boundary layer serves as a sink. Flow is drawn away from the region by the negative displacement thickness. If the negative thickness is added to the wedge surface to give a displaced wall, and the result treated as an inviscid approximation to the viscous flow field, a schematic representation of the physical processes involved is obtained [19]. This is illustrated in Fig. 24. According to the

-18-

model, an expansion fan exists at the foot of, and behind the incident shock wave, and compression waves subsequently coalesce to form the reflected shock wave. The compression waves are due to the decrease in rate of growth of the displacement thickness δ^*. The angle at which flow enters the boundary layer is henceforth referred to as 'boundary-layer flow entry angle', θ_{bl}, and its distribution with respect to x is of the form (see App. D):

$$\tan(\theta_{bl}) = \frac{1}{2} (\delta^*/x^{\frac{1}{2}}) \, x^{-\frac{1}{2}} = C_1 \, x^{-\frac{1}{2}} \tag{3.3}$$

where C_1 is a constant based on the flow properties in the freestream, external to the boundary layer. The variation of θ_{bl} with axial distance, as defined by Eq. 3.3, is shown in Fig. 25 for a typical boundary layer in air. At x=0, $\theta_{bl} = 90^{\circ}$ and the flow enters the boundary layer normal to the surface (see Fig. 24). At x = 1mm, θ_{bl} is nearly 0°, and the flow is nearly parallel to the surface. While this model gives a qualitative illustration of the flow processes involved, quantitative information in the immediate vicinity of the reflection point P can not be obtained from the simple model for the following reason. The expansion fan right at point P, which turns the flow normal to the wedge surface, is not an accurate representation of the real process, but the result of a singularity in the model which occurs at x = 0 (see Eq. 3.3) Since the distances being dealt with are so small, one must consider the mean free path of the gas molecules, and whether or not the flow still behaves as a continuum. As an example, for a RR at $M_s = 2.0$, $p_0 = 2.0$ kPa, and $T_0 = 300$ K, the mean free path of air is calculated to be 2.5×10^{-5} mm based on region 1 flow Since the concept of a continuum (which the model assumes) can only be applied over a scale greater than several mean free paths, it is unwise to believe any quantitative results within this distance of P. The expansion fan and subsequent compression waves within this distance of P are therefore probably quite different than what is drawn in the model. Accurate

-19-

modelling in this region would require kinetic theory which is beyond the scope of this work. Note also that the size of these features is so small that they can not be seen. The model is not based on what is known to occur, but what is believed will occur.

It is quite clear from the model that the reflection region is very complex. To calculate the growth of the boundary layer, the freestream conditions outside the boundary layer must be known. These change with distance from the reflection point however, ranging from region 1 flow properties just behind the incident shock wave, to region 2 flow properties further downstream. As a simplification, the boundary-layer growth is calculated assuming constant freestream conditions based on region 1 flow properties.

The results for boundary-layer size at a distance of 1 mm from the reflection point P are shown in Fig. 26. As anticipated, the displacement thickness δ^* is zero for $M_s = 1$ since there is no flow perturbation behind a Mach wave, and δ^* levels off at high M_s.

According to the prediction for boundary-layer growth, the boundary-layer flow entry angle θ_{bl} will range from $90°$ at point P, to 0 at $x = \infty$. However, only a small region near P should influence the reflection process. The size of this region is the characteristic length of the boundary layer. In the case of RR, the characteristic length is taken to be the distance from the reflection point P at which the experimentally determined displacement wedge angle θ_d, matches the predicted boundary-layer entry angle θ_{bl}. This characteristic length can be calculated by setting θ_{bl} equal to θ_d in Eq. 3.3, and solving for x. This definition of characteristic length is somewhat arbitrary. It is not expected that something unique occurs where θ_d and θ_{bl} match, but the distance x at which this happens is believed to be

-20-

representative of the scale of the region of the boundary layer which affects the reflection process.

3.2.3 Effect of Shock-Wave-Induced Boundary Layer on the RR◄►MR Transition Line

Henderson and Lozzi [12] performed shock-wave-reflection experiments with a symmetrical wedge in unsteady flow to eliminate any sidewall boundary-layer effects, and demonstrated that either the 'sonic' or 'detachment' criteria was correct. As noted previously, it is very difficult to experimentally resolve the difference between the two criteria. Hornung and Taylor [19] did an interesting set of experiments in argon to see the effect of initial pressure on the RR◄►MR transition boundary. Using a variable-angle wedge, they did four series of experiments, each with a different initial pressure. The Mach number was held constant. In each series, the wedge angle was varied, and they measured the size of the Mach stem in MR. The point at which the Mach stem would vanish was extrapolated from each series, and taken to be the point where transition would occur. The results of the four series showed that the RR◄►MR transition boundary was shifted downward. The magnitude of the shift was greater when the initial pressure was lower, in a manner consistent with Eq. 3.1b. Unfortunately, their results were only for one shock-wave Mach number, $M_s = 5.5$.

As seen in Figs. 22 and 23, the boundary layer alters the boundary condition of no net flow deflection at the wall (Eq. 3.2). To predict a new transition boundary, the 'detachment' criterion might still be used, though in a modified form. Recall that this criterion stated in principle that transition would occur when RR was no longer physically possible. At this point, the maximum possible deflection would occur through the reflected shock wave. Using this same criterion, but altering the boundary condition at the

-21-

wall (Eq. 2.1), the RR←→MR transition boundary criterion can be written as:

$$\theta_1 - \theta_{2m} = \theta_d \qquad (3.4)$$

The effect of various values of θ_d on the transition boundary is shown in Fig. 27. For each degree of displacement wedge angle, the boundary shifts downward by approximately $0.7°$. The shift in boundary varies linearly with θ_d over the range shown. The distribution of ω' along the RR←→MR transition boundary is shown in Fig. 28 for various values of θ_d. The reflected wave angle ω' is not affected much by θ_d. At high M_s, maximum shift of ω' is obtained, a reduction of ω' of $0.44°$ for every $1°$ shift in θ_d. Like the RR←→MR transition boundary, the shift in ω' varies linearly with θ_d.

It now remains necessary to experimentally determine the deviation of the RR←→MR transition boundary from the inviscid 'detachment' criterion boundary, and to correlate the results with the predicted boundary-layer size. This can be done by:

(1) conducting experiments to obtain several transition boundary points,

(2) measuring the reflected wave angle ω',

(3) calculating the net flow deflection through the incident and reflected shock waves to get the displacement wedge angle θ_d,

(4) equating this θ_d value to the predicted distribution of boundary-layer flow entry angle θ_{bl} using Eq. 3.3 to get a characteristic length.

A look at flow properties of the inviscid RR solution can indicate which parameters should affect the influence of the boundary layer on the reflection process, or displacement wedge angle θ_d. According to the simplified model of

-22-

Fig. 24, the boundary layer in RR forms in region 1, behind the incident shock wave. In addition, the reflected shock wave is due to the compressive effects of the displaced wall which must turn the flow in region 1 back parallel to this wall. The reflection process is therefore dependent on the flow parameters, M_1, p_1, T_1, θ_1 in region 1. The boundary layer has been modelled using the displacement thickness δ^*, which is a measure of the increase of mass flow in the boundary layer relative to the freestream. Displacement thickness is defined at freestream conditions M_1, p_1, T_1, and by using it to represent the boundary layer, the influence of p_1 and T_1 are accounted for. The effect of θ_1 and M_1 on the reflection process in the presence of a boundary layer is still unknown.

The variation of θ_1 and M_1 with M_s is shown in Figs. 29 and 30. It can be seen that the two parameters are relatively stationary at high Mach number ($M_s > 5.0$), and change quite rapidly at low Mach number ($M_s < 3.0$). The boundary-layer displacement thickness is also fairly constant for high M_s (Fig. 26). The three parameters which are believed may affect the RR⟷MR transition boundary shift due to viscosity, M_1, θ_1, and boundary-layer size (for fixed p_0) are all approximately constant at high M_s. It should therefore be anticipated that for a fixed initial pressure, the displacement wedge angle θ_d, and therefore the shift of the RR⟷MR transition boundary due to viscosity, should also be relatively invariant at high M_s. As a result, a viscous RR⟷MR transition boundary should be quite flat at high M_s (see Fig. 27).

Chapter 4

EXPERIMENTAL WORK

4.1 Shock-Tube Facility

Experiments were carried out in the UTIAS 10cm x 18cm Hypervelocity Shock Tube. This facility has the capability of both cold-gas driven and combustion driven runs. However, combustion driven runs were not attempted owing to the possibility of damaging the test-section windows when operating with high wedge angle [39]. A full description of the facility and its capabilities can be found in Boyer [40] and Ben-Dor and Whitten [41].

By increasing the pressure in the compression chamber on one side of a diaphragm until it ruptured, shock waves were sent down the channel. The driver gas was added slowly so that after the diaphragm ruptured, the shock speed would not be influenced during its time of travel by the additional mass flow. Shock speeds were controlled by varying the type of driver gas, the diaphragm thickness and pressure ratio across the diaphragm. The diaphragms consisted of several sheets of mylar polyester stacked together. The sheets were available in several nominal thicknesses, and by proper combination nearly any desired thickness could be achieved. There is a practical limit to the maximum thickness which can be used since very thick diaphragms do not break properly and their breaking pressure is unpredictable. For this reason, the maximum overall diaphragm thickness used was 1.07 mm. The driver gases used were CO_2 and He. Shock-wave Mach numbers up to $M_s = 6.5$ were achieved. While H_2 as a driver gas would give even higher shock speeds, the possible risk of explosion made its use undesirable. For test gas pressure under 26.7 kPa (200 torr), commercially available Medical Grade Air was used. All other runs used air from the laboratory as the test gas.

-24-

Initial gas temperature was measured by a mercury-bulb thermometer embedded in the shock tube wall. A minimum of 5 minutes was allowed between entry of the test gas and reading from the thermometer to allow the temperature to stabilize. The thermometer scale was marked at 0.1 C intervals.

The initial gas pressure was measured by a series of Wallace and Tiernan type FA 160 dial gauges. The range and maximum error of the gauges are shown below.

	Range	Absolute Error
1.	0 - 50 torr (6.67 kPa)	0.2 torr
2.	0 - 200 torr (26.7 kPa)	1.0 torr
3.	0 - 400 torr (53.3 kPa)	2.0 torr
4.	400 - 800 torr (106.7 kPa)	2.0 torr

To guard against possible leakage of air into the shock-tube test section, test gas pressure was checked at the time of admission, and also 5 minutes after. Leaks which would cause a variation in pressure of greater than 0.05 torr (6.7 Pa) at the time of firing the shock tube were unacceptable and the runs were aborted. This corresponds to a leak rate of approximately 0.01 torr/min. and was found to be extremely rare.

The incident-shock-wave speed was determined by measuring the time interval between a common starting point and several stations distributed down the channel. Time intervals were measured by 5 digital counters using a 1 MHz oscillator as a common time base. Trigger signals from each station were obtained using Atlantic LD-25 blast-wave pressure-transducers. Start signal for all the counters came from station D, and the 5 counters were stopped by signals from stations F, G, H, I, and J. A schematic diagram of the set-up is

-25-

shown in Fig. 31. To allow for deceleration of the shock wave, owing to the
sidewall boundary-layer growth, a second-order best-fit curve was applied to
the measurements from stations F, G, H, and I, and extrapolated to give a
velocity at the center of the test section. The interval at station J was not
used because the shock-wave speed changes significantly after it has passed
over the wedge.

Shock-wave-reflection patterns were recorded using a 23 cm dia.
field-of-view Mach-Zender interferometer. With the exception of 4 experiments
where shadowgraphs were taken, infinite-fringe interferograms were used. Two
wavelengths were used for the interferograms (3971 Å and 6943 Å) to establish
both qualitative and quantitative results. The 3971 Å interferograms give
twice as many fringes as the 6943 Å interferograms, but suffer from lack of
contrast. This type of recording was chosen because it gives a great deal of
quantitative density information, and the presence of fringes makes it easier
to see the Mach stem, even when it is quite small. The 4 shadowgraphs were
taken to compare resolution between them and the interferograms, and were
found to be inferior.

The light source for the interferometer was a giant-pulse ruby-laser
incorporating a TRG model 104A laser head, a TRG model 2113-1 harmonic
generator and TRG Pockels Q-switch. The flashlamp capacitor bank of the laser
and the Q-switch were fired at the appropriate times by delaying the trigger
signal from stations F and I respectively. The capacitor bank was fired at
900_s before the Q-switch in order to get a single giant pulse from the laser.
In this mode, the laser delivers 0.8 Joules of light energy in a 15 ns pulse.
Interferograms were recorded on Kodak Royal-X Pan film, and developed in Kodak
HC-110 developer. The negatives were developed using twice the recommended
time, to increase the effective film speed (nominal speed is 1250 ASA), and
contrast.

-26-

4.2 Range of Experiments

Experiments were done to determine several RR◄►MR transition boundary points. Equipment limitations often determined which initial pressure could be used. In the low Mach number range ($M_s < 1.5$), pressures had to be near atmospheric so that the pressure jump across the incident shock wave was sufficient to trigger the timing equipment and the laser. At very high Mach numbers ($M_s < 4.0$), very low initial pressures were needed to achieve sufficiently high pressure ratios across the diaphragm, but at the same time must be high enough to trigger the equipment. Low initial pressures are extremely beneficial since they enhance viscous effects.

Experiments were performed over a range $1.1 < M_s < 6.5$ using wedges of $42°$, $45°$, $47°$, and $48°$. Pressures ranged from 400 Pa (3 torr) at high M_s, to 101 kPa (760 torr) at very low M_s. Typically, to determine a particular transition boundary point, wedge angle and diaphragm thickness were held constant. Runs were then done at several different initial pressures. The Mach number for each run is thus slightly different since the pressure ratio across the diaphragm is altered. A transition point (p_0, M_s, θ_w) is thus obtained.

It is a desirable condition to vary the initial pressure, p_0, and shock Mach number, M_s, for a fixed wedge angle, θ_w, particularly when looking for a transition point at high Mach number. As discussed in Chapter 3, for a constant pressure it is expected that the RR◄►MR transition boundary on the (M_s, θ_w) plane is relatively flat at high M_s for p_0 constant. Experimentally then, if p_0 and θ_w are fixed, and M_s varied, one could conceivably be doing experiments parallel to the transition boundary, but not

-27-

crossing it. In the low M_s region where the inviscid transition boundary is quite steep, this problem should not occur.

It was attempted in one series of experiments (at low M_s) to hold the initial pressure constant and change the diaphragm thickness to control shock speed, but it was extremely difficult to find the proper combination of diaphragms to achieve the required breaking pressure and shock speed M_s. This method is not recommended. A variable-angle wedge or plunger to rupture the diaphragm at a desired pressure would solve most of these problems, but the UTIAS shock tube is not equipped for either. If further work in finding transition boundary points is to be done, it is highly recommended that both mechanisms be used to greatly simplify the experiments.

4.3 Measurement of Data from Interferograms

The one drawback to recording shock-wave reflections photographically is the inevitable problem of interpreting the data. Flaws in the optics and grain of the film limit the resolution of the interferograms, and can make determination of the type of reflection difficult and subjective. In the case of transition from RR to DMR, determination is rather simple. In DMR the two Mach stems are separate and distinct. Transition from RR to SMR or CMR is often difficult to see. The Mach stem in MR may be so small that its size is almost immeasurable, and the fringe distortion caused by the slipstream can be confused with that caused by the boundary layer.

One way of separating the two is to look at the shape of the fringe distortion. A slipstream should slope toward the wedge surface and distortion from it appear to decrease in size as distance from the Mach stem increases. A boundary-layer-induced distortion, if visible, should increase in size as distance from the reflection point increases.

Measurement of wave angles is also difficult. For optical reasons, the reflected shock wave appears to have a finite, measurable thickness (Figs. 39a and 39b). It also appears to be quite 'fuzzy' near the reflection point. It was found that a precise and accurate measurement of angle could only be made at distances of 1 mm or greater from the reflection point. The angle between the incident and reflected shock waves, δ, was measured by drawing lines tangent to the incident and reflected shock waves at a distance of 1mm from P, and trigonometrically determining the angle. Both first and second harmonic photographs were measured independently. If the angles measured from the two differed by more than 1.5°, they were remeasured until they were within 1.5°. The wave angle was taken as the average. Wave angles measured by different people using different techniques can differ by as much as 3° and is highly subjective. For this reason, one should not be too alarmed by different wave angles quoted for the same photograph.

Chapter 5

DISCUSSION OF RESULTS

In this chapter, the experimental results will be discussed in three separate and distinct sections:

(1) A qualitative look at some of the features observed of the 4 types of reflection

(2) An analysis of the transition boundary shift obtained, and its relationship to the boundary layer

(3) A brief observation of the effect of the boundary layer on the Mach stem in MR

5.1 Observed Features RR, SMR, CMR and DMR

Figures 39 through 42 illustrate the four types of reflection obtained, and reveal some interesting features of the flow. Figures 39a and 39b show a case of regular reflection (RR). No evidence of a Mach stem or slipstream is seen at the reflection point P. Some distortion at the wedge surface indicates the presence of a boundary layer.

There is no physical evidence that the structure of the reflected shock wave is like the physical model in Chapter 3 (Fig. 24). Rapid curvature of the reflected shock wave near the reflection point is not seen (Fig. 39b), contrary to the model. This would suggest that the size of region which dominates the reflection process may be smaller than can be seen in the interferogram, or that the model is inaccurate and a better one is needed.

For this set of experimental conditions, the theoretical, inviscid solution is that of Mach reflection (MR), with a triple-point-trajectory angle $x = 2.84$°. This is shown in Fig. 39a. The difference between theory   and

experiment is particularily notable in this case, since the initial pressure is quite high (p_0 = 100.8 kPa). With lower pressure, one would expect even greater disagreement between theory and experiment.

Figures 40a and 40b show a case of SMR. The Mach stem is quite evident, as is the slipstream. Again, the Mach stem is much smaller than the inviscid prediction. Clearly, the slipstream slopes toward the surface, and it is this feature which distinguishes it from the boundary layer. In some cases with an extremely small Mach stem, this is the only way to differentiate between RR and MR.

Figures 41a and 41b show a case of CMR. The exact position of the kink K is not certain due to the apparent thickness of the shocks, but the curvature reversal is quite clear. It is probable that some cases of CMR were judged to be SMR. Near the RR◄►MR boundary, the kink is very weak, and it is likely that in some marginal cases it can not be distinguished, even though it exists. The slipstream emanating from the triple point slopes down to interact with the boundary layer on the wedge surface. Note that this is a shadowgraph, so fringes do not appear. In one aspect, shadowgraphs are superior. The shocks tend to appear thinner and more well defined than in interferograms.

Finally, DMR is shown in Figs. 42a and 42b. Again, as with SMR and CMR, the triple point does not follow the predicted trajectory. In this case the difference is quite large (2.8°), likely due to the low initial pressure (p_0 = 1.47 kPa), and the resultant large viscous effects.

5.2 RR◄►MR Transition Boundary Shift

A summary of the 98 experiments performed is contained in Table 1. In addition, they are plotted in the (M_s, θ_w) plane for each wedge angle in Figs.

-31-

32 to 38. From the series of experiments, several points were selected which were felt to represent the limit of RR, transition boundary points. The selection of transition points from experimental data is often not clear and as a result subjective. The difficulty comes about in part from the fact that both Mach number and initial pressure change in a series, a limitation dictated by the equipment available (see Chapter 4). Ideally, for a fixed wedge angle, as the initial pressure is dropped the Mach number will increase gradually. All the experiments will be one type of reflection, and then at some point the type of reflection will change from RR to MR or MR to RR. As Mach number is further increased the type of reflection would not change back. In this ideal situation the point of transition is quite distinct. Remember that a transition point is defined by M_s, θ_w, and p_0. Although far from ideal, this behavior can be seen in Figs. 32, 33, 35a, 35b, and 38. A transition point is relatively easy to pick.

In Figs. 34, 36, and 37, the transition point is not so clear. The regions of RR and MR are not distinct from one another, and there is overlap. The progression of Mach number with decreasing initial pressure is not smooth. In cases where MR experiments appeared in what was thought to be a RR zone or vice versa, runs were repeated in an attempt to check their validity. However, in these three series of experiments, the RR and MR regions could not be clearly defined. It then became highly subjective in selecting a transition point. In Fig. 34 there is some overlap but it is not too bad. Figure 36 has quite a great deal of it, and the only portion where RR and MR are separate and distinct is near $M_s = 4.0$. Figure 37 has two RR points in an apparent MR zone ($M_s = 4.65, 5.28$) but these are not considered valid since they could not be repeated. Some of the overlap of regions at low M_s is undoubtedly due to misjudging of type of reflection. MR runs at low M_s are very difficult to distinguish from RR. The points which were judged to

represent the limit of RR, or transition, are indicated on each of the figures and summarized in Table 2.

An additional transition boundary point is taken from experiments by Deschambault [29]. In a series of experiments at (M_s = 3.71, θ_w = 49°, p_0 = 6 kPa) he obtained examples of both RR and MR. It was suggested that the RR case was actually MR, its Mach stem not having had time to grow sufficiently to be seen. In the RR case the shock had travelled 60% of the way up the wedge. In the MR case, the shock had travelled 80% of the way, and had a triple-point-trajectory angle χ = 1.3°. If the RR case were actually MR as suggested, then one might expect that with χ = 1.3°, the Mach stem would be approximately 1.4 mm high at 60% up the wedge surface. A Mach stem of this size would be quite visible. A more likely explanation for the difference is that the experiment lies at or very near the RR   MR transition boundary.

From an examination of Figs. 35a and 35b, it is quite clear that initial pressure has an effect on the position of the transition boundary. The two sets of runs, which have a different range of initial pressures, have significantly different Mach numbers at transition. The transition point corresponding to the lower initial pressure has a higher Mach number, which puts it further from the inviscid transition boundary. This is entirely expected as viscous effects should be more prominent for cases with lower initial pressure.

The analysis of the transition boundary points will take the following steps:

(1) Comparison of the selected transition boundary points with
      the inviscid 'detachment' criterion boundary

(2) Comparison of reflected wave angle ω' with that predicted
      by the 'detachment' criterion

-33-

(3) Reduction of experimentally determined displacement wedge

angle θ_d to a common initial pressure

(4) Comparison of θ_d to predicted boundary-layer size

(5) Calculation of characteristic length

(6) Prediction of a viscous RR⟷MR transition boundary for air

The selected transition boundary points are plotted against the inviscid 'detachment' criterion boundary in Figs. 43 and 44. Notice that the deviation from the inviscid boundary is much greater at high M_s, due primarily to low initial pressure. The highest deviation from the 'detachment' criterion boundary is $5.4^\sim$ in θ_w, which occurred for an experiment with $\theta_w = 45^\circ$, $M_s = 6.21$, $p_0 = 0.45$ kPa. This behavior, persistence of RR well below the 'detachment' criterion boundary at high M_s, is certainly not applicable to all gases. Experiments by Hu [28] in SF_6 and Ikui et al [42] in Freon-12 show persistence of DMR above the 'detachment' criterion boundary at high M_s. These two gases are unique since they both have a low specific heat ratio γ. One should therefore be cautious in extending the high M_s results of this investigation in air to other gases without doing a similar analysis.

In the low M_s regime (Fig. 43), some of the points seem quite close to the inviscid boundary, and the difference might be taken as insignificant. However, this is not the case. Only the steep slope of the boundary makes the differences appear quite small. Note also (Fig. 26) that the boundary layer should also be much smaller at low M_s.

It can also be shown that the 'detachment' criterion, which states that transition will occur when the maximum flow deflection possible occurs through the reflected shock wave, still seems to hold under the influence of

-34-

viscosity. In Fig 45, measured values of reflected-shock-wave angle ω' are compared to those predicted by a modified 'detachment' criterion (Eq. 3.4). The variation of reflected-shock-wave angle ω' with displacement wedge angle θ_d as predicted by Eq. 3.4 is quite small. Experimentally obtained ω' values are close to the predicted values, within experimental error in measurement. This implies that the concept of the 'detachment' criterion is still valid.

Due to experimental limitations, there was a wide variety of initial pressures. Valid comparison of results requires reduction to some standard. While it may at first seem desirable to reduce results to a common Reynolds number, this is not chosen for the following reasons. The boundary-layer size does not reduce to a simple dependence on Reynolds number (see App. D). Also, it would be a misleading representation since the only valid length scale, which is necessary to define a Reynolds number, is the characteristic length which may not be the same for all the experiments.

Instead it is chosen to reduce the results to a common initial pressure. From Eq. 3.1b it can be seen that any viscous effect can be scaled by initial pressure. Figure 46 displays the experimentally determined displacement wedge angle θ_d, a result of viscous effects, after reduction to an initial pressure of 2.0 kPa. Remember that θ_d is obtained by applying gasdynamics of frozen flow to calculate the flow deflection across the incident shock wave and the measured reflected shock wave. As anticipated, the displacement wedge angle θ_d, a measure of departure from the 'detachment' criterion boundary, is relatively constant at high M_s, with a value of approximately $4°$. At low M_s, θ_d is higher, near $6.5°$. This is an unexpected behavior since the predicted boundary-layer size is much smaller at low M_s (Fig. 26). The source of scatter of the two points near $M_s = 3.8$ is unknown.

-35-

To appreciate this difference quantitatively, Fig. 47 shows the ratio between a predicted boundary-layer size parameter, and the experimentally determined θ_d. As a measure of the predicted boundary-layer size, the boundary-layer flow entry angle θ_{bl} at a distance of 1 mm from the reflection point P is used (see Eq. 3.3), and given the special symbol Ω. This boundary-layer size parameter, Ω, was chosen instead of $\delta^*/x^{\frac{1}{2}}$ since it has the same sense as θ_d, both being angles. While less fundamental than $\delta^*/x^{\frac{1}{2}}$ it is a valid representation, for comparitive purposes, of boundary-layer size, since it is proportional to $\delta^*/x^{\frac{1}{2}}$.

$$\Omega = \theta_{bl}\Big|_{x=1mm} \tag{5.1}$$

The experimentally determined θ_d is much larger than θ_{bl} in the predicted boundary-layer at x = 1 mm. This indicates that the characteristic length of the boundary layer which dominates the reflection process is much less than 1 mm.

Since the displacement wedge angle has been determined experimentally, and the boundary-layer size $\delta^*/x^{\frac{1}{2}}$ has been predicted, the characteristic length can be determined by putting the two values into Eq. 3.3 and solving for x. This has been done and is shown in Fig. 48. The characteristic length ranges from 0.0025 mm at low M_s to 0.048 mm at high M_s. With values so small, it would be impossible to resolve any features in the region of reflection point P which is dominated by viscous forces. It is also so small that the previous assumption of frozen flow and laminar boundary layer in the region of interest is correct. The smallest vibrational relaxation length for the experiments was found to be 33 mm for O_2 in Exp. 62 for which $p_0 = 0.45$ kPa $T_0 = 24.8$ C, $M_s = 6.21$ (see Fig. C-1). In addition, the maximum Reynolds number was of the order of 10^3 based on the characteristic length, much less than

that at which transition to turbulent flow (10^5) might be expected to occur [36].

The inability to see any details of the viscous reflection process near P demonstrates the necessity for numerical codes which can simulate these processes. Inviscid numerical simulations of shock-wave reflections currently give excellent results [43], as do codes which approximate the effects of viscosity [51], but a solution of the Navier-Stokes equations very close to the reflection point P is still a step beyond. However, rapid technological advancement of supercomputers should make this possible in the near future.

It was shown in Fig. 47 that the ratio of experimentally determined displacement wedge angle θ_d to boundary-layer size parameter Ω was much greater at low M_s. In other words, a boundary-layer of a particular size will have much more effect on RR at low M_s than at high M_s. It is hypothesized that this ratio should be dependent on flow deflection θ_1 through the incident shock wave for the following reason. The ability of a boundary layer to influence a reflection process should be affected by the relative size of the forces involved. The effect of the boundary-layer is that of mass transfer from the reflection point P. The rate at which mass is transferred toward the wedge surface after deflection through the incident shock wave is proportional to $\sin(\theta_1)$. If the flow deflection through the incident shock wave is quite small, then the influence of the boundary layer should be quite significant compared to the mass transfer towards the wall which gives rise to the reflection process. At high M_s, the mass transfer in the boundary layer is less significant compared to the mass transfer toward the wall, so it has less effect on RR.

Figure 49 shows the ratio Ω / θ_d as a function of deflection angle θ_1 through the incident shock wave. θ_1 is very close to $\sin(\theta_1)$. The relationship appears to be close to linear, as might be expected for the hypothesis given above.

The net result of all this is a prediction (based on experimental results) of a viscous RR◄►MR transition boundary for air. If a linear relationship between Ω / θ_d and $\sin(\theta_1)$ is assumed (see Fig. 49), and the result applied to the predicted values of θ_1 and boundary-layer size parameter Ω (Eq. 5.1), a distribution of θ_d is obtained. When substituted into the modified 'detachment' criterion (Eq. 3.2) the result is a new RR◄►MR transition boundary. This is shown in Fig.50, for a nominal initial pressure of 5.0 kPa. Scaling to any other initial pressure is simple, since the difference between the inviscid and viscous boundaries is a direct function of initial pressure (Eq. 3.1b). Note that Fig. 50 is quite similar to Fig. 27 since the experimental values for θ_d were found to be constant at high M_s, which is precisely what is plotted in Fig. 27, curves of constant θ_d.

5.3 Behavior of X Near RR◄►MR Boundary

In the series of experiments for wedge angles of 47 and 48 , many MR cases were obtained, with reasonable variation of initial pressure. It is expected that the boundary layer on the wedge surface will act as a sink and 'pull' the triple point down toward the wedge. The boundary-layer size, and presumably its influence, should increase with decreasing initial pressure (see Eq. 3.1b). The difference between the inviscid prediction of triple-point-trajectory angle χ and the experimentally obtained value should therefore be affected by initial pressure. This difference is plotted in

Figs. 51 and 52 for two sets of experiments. On each graph, a best-fit curve of the form:

$$X_{inv} - X = C_1 + C_2\, p_0^{-\frac{1}{2}} \qquad (5.2)$$

is plotted. This form is anticipated since the boundary-layer size is affected by initial pressure or density in that way (see App. D). There is a fair amount of scatter in the data, but the trend is quite clear. As the initial pressure gets lower, the viscous forces increase and the difference between the inviscid prediction of X and the experimentally measured value increases. Theoretically, as the initial pressure gets extremely large, the viscous forces should become negligible and the solution should approach the inviscid case. Extrapolating the best-fit curves to $p_0 = \infty$ gives:

$$\text{for } \theta_w = 48° \qquad X_{inv} - X = 0.64°$$

$$\text{for } \theta_w = 47° \qquad X_{inv} - X = -0.95°$$

The fact that a non-zero value is obtained may be due in large part to the scatter of data involved. The scatter itself may be affected by the distance up the wedge that the shock has progressed when the interferogram was taken (see below). Hornung and Taylor [19] did 24 experiments, and were able to extrapolate their results more closely to the inviscid RR⟷MR transition boundary. It is anticipated that if many more experiments were done here, a more accurate curve might be drawn, with less scatter of data.

The influence of the boundary layer on the triple-point-trajectory angle X should be dependent on their proximity to each other. As the Mach stem grows, it gets further from the boundary layer. If the boundary layer is thought of as a sink, its influence on X should drop off with distance. Therefore, as the Mach stem grows, the boundary-layer influence diminishes, so

that the growth of the Mach stem, and therefore χ, is inherently non-linear with time. The existence of viscosity eliminates the self-similarity that exists for the inviscid process. Any comparison of the triple-point trajectory angle with inviscid predictions should be done with respect to initial pressure especially when the initial pressure and χ are quite small.

Chapter 6

CONCLUSIONS

Many RR◄·►MR transition boundary points in air were determined experimentally by performing shock-tube runs very close to the boundary. Reflected wave angles were found to be consistent with the 'detachment' criterion for pseudostationary flow. As anticipated, initial low pressures enhance viscous effects. As the pressure is lowered, the transition boundary shifts downward on the (M_s, θ_w) plane, giving rise to the 'von Neumann paradox', in agreement with many experimenters. Viscous effects have been found to be the cause of the 'von Neumann paradox'.

By reducing the experimental results to a common initial pressure, a new viscous RR◄·►MR transition boundary for air was drawn and found to be in good agreement with the 100 experiments. The new transition boundary does not appear to be valid for gases with low values of γ such as Freon-12 and SF_6 at high Mach number.

For a given pressure, the boundary layer has a greater effect on the transition boundary at lower Mach number, even though the physical size of the boundary layer is smaller. It is hypothesized that the degree of influence is inversely proportional to flow deflection through the incident shock wave, due to the relative size of the mass flow toward the wedge surface behind the incident shock and the mass flow in the boundary layer.

The model used to approximate the influence of viscous forces could not be substantiated experimentally, and is assumed to be approximate. It did however indicate that the characteristic length of the flow is of the order of 0.01 mm, and therefore that the assumptions of laminar boundary layer and frozen flow as used herein were appropriate. It is felt that correct and

accurate modelling of the reflection process will probably come about through numerical codes which incorporate the influence of viscosity through a solution of the Navier-Stokes equations.

While not directly investigated, results from MR experiments demonstrate that viscosity also affects the size of the Mach stem. Lower initial pressure reduces the size of the Mach stem, but scatter of the limited data does not make for a precise quantitative assessment. This is one area of study which should be investigated further.

In the most general sense, viscosity plays a very significant role in oblique-shock-wave reflection. The RR$\leftrightarrow$MR transition boundary is lowered a significant amount (up to 5°), and the Mach stem size in MR is reduced. Previous studies which investigated oblique-shock-wave reflection without consideration of viscous effects are thereby missing an important factor. Definition of an experimental point in terms of M_s and θ_w is insufficient, for oblique-shock-wave reflections are a function of M_s, θ_w, and initial pressure.

REFERENCES

1. Baker, W. E., "Explosions in Air", University of Texas Press, Austin, 1973.

2. Glass, I. I., "Shock Waves and Man", University of Toronto, Institute for Aerospace Studies, Toronto, 1974.

3. Robinson, Clarence A. Jr., "Parallel Programs Advance Small ICBM", Aviation Week and Space Technology Magazine, p. 14, March 5, 1984.

4. Mach, E., "Uber den Verlauf der Funkenwellen in der Ebene und im Raume", Oesterreichische akademie der wissenschaften, Mathematisch-naturwissen-schaftliche klasse, sitzungsberichte, abt. II, v. 78, pp. 819-838, 1878.

5. von Neumann, J., "Oblique Reflection of Shocks", Explosives Research Report No. 12, Navy Dept., Bureau of Ordinance Re2c, Washington, D.C., 1943.

6. von Neumann, J., "Refraction, Interaction, and Reflection of Shock Waves", NAVORD Report 203-45, Navy Dept., Bureau of Ordinance, Washington, D.C., 1945.

7. Bleakney, W. & Taub, A. H., "Interaction of Shock Waves", Rev. Mod. Phys., Vol. 21, p. 584, 1949.

8. Smith, L. G., "Photographic Investigation of the Reflection of Plane Shocks in Air", OSRD Report No. 6271, or NORC Report No. A2350, 1945.

9. White, D. R., "An Experimental Survey of the Mach Reflection of Shock Waves", Tech. Report II-10, Dept. of Phys., Princeton University, 1951.

10. Kawamura, R. & Saito, H., "Reflection of Shock Waves - 1. Pseudo-Stationary Case", J. Phys. Soc. Japan, Vol. 11, No. 5, p. 584, 1956.

11. Gvozdeva, L. G., Bazhenova, T. V., Predvoditeleva, O. A. & Fokeev, V. P., "Mach Reflection of Shock Waves in Real Gases", Astronautica Acta, Vol. 14, p. 503, 1969.

12. Henderson, L. F. & Lozzi, A., "Experiments on Transition of Mach Reflection", J. Fluid Mech., Vol. 68, p. 139, 1975.

13. Bazhenova, T. V., Fokeev, V. P. & Gvozdeva, L. G., "Regions of Various Forms of Mach Reflection and its Transition to Regular Reflection", Astronautica Acta 3, p. 131, 1976.

14. Law, C. K. & Glass, I. I., "Diffraction of Strong Shock Waves by a Sharp Compressive Corner", CASI Trans., Vol. 4, No. 1, 1971.

15a. Ben-Dor, G. & Glass, I. I., "Domains and Boundaries of Non-Stationary Oblique Shock-Wave Reflexions. 1. Diatomic Gas", J. Fluid Mech., Vol. 92, p. 459, 1979.

15b. Ben-Dor, G. & Glass, I. I., "Domains and Boundaries of Non-Stationary Oblique Shock-Wave Reflexions. 2. Monatomic Gas", J. Fluid Mech., Vol. 96, p. 735, 1980.

16. Shirouzu, M. & Glass, I. I., "An Assessment of Recent Results on Pseudo-Stationary Oblique-Shock-Wave Reflections", Univ. of Toronto, UTIAS Report No. 264, 1982.

17. Hornung, H. G. & Kychakoff, G., "Transition from Regular to Mach Reflexion of Shock Waves in Relaxing Gases", Proc. 11th International Shock Tube Symposium, 1977

18. Hornung, H. G., Oertel, H. & Sandeman, R. J., "Transition to Mach Reflexion of Shock Waves in Steady and Pseudosteady Flow with and without Relaxation", J. Fluid Mech., Vol. 90, p. 541, 1979.

19. Hornung, H. G. & Taylor, J. R., "Transition from Regular to Mach Reflection of Shock Waves Part 1. The Effect of Viscosity in the Pseudosteady Case", J. Fluid Mech., Vol. 123, p. 143, 1982.

20. Molder, S., "Head-on Interaction of Oblique Shock Waves", Univ. of Toronto, UTIAS Tech. Note No. 38, 1960.

21. Weynants, R. R., "An Experimental Investigation of Shock-Wave Diffraction Over Compressive and Expansive Corners", Univ. of Toronto, UTIAS Tech. Note No. 126, 1968.

22. Ben-Dor, G., "Regions and Transitions of Nonstationary Oblique Shock-Wave Diffractions in Perfect and Imperfect Gases", Univ. of Toronto, UTIAS Report No. 232, 1978.

23. Ben-Dor, G. & Glass, I. I., "Nonstationary Oblique Shock-Wave Reflections: Actual Isopycnics and Numerical Experiments", AIAA J., Vol. 16, p. 1146, 1978.

24. Ando, S., "Pseudo-Stationary Oblique Shock-Wave Reflection in Carbon Dioxide - Domain and Boundaries", UTIAS Tech. Note No. 231, 1981.

25 Ando, S. & Glass, I. I., "Domains and Boundaries of Pseudostationary Oblique-Shock-Wave Reflections in Carbon Dioxide", 7th Int. Symp. of Military Applications of Blast Simulation, Medicine Hat, Alberta, 1981.

26. Lee, J. H. & Glass, I. I., "Domains and Boundaries of Pseudo-Stationary Oblique Shock-Wave Reflections in Air", Progress in Aerospace Sciences, Vol. 21, pp. 33-80, 1983.

27. Hu, T. C. J. & Shirouzu, M., "Tabular and Graphical Solutions of Regular and Mach Reflections in Pseudo-Stationary Frozen and Vibrational-Equilibrium Flows", Univ. of Toronto, UTIAS Report No. 283, 1985.

28. Hu, T. C. J., "Pseudo-Stationary Oblique-Shock-Wave Reflections in a Polyatomic Gas -- Sulfur Hexafluoride", Univ. of Toronto, UTIAS Tech. Note No. 253, 1985.

29. Deschambault, R. L., "Nonstationary Oblique-Shock-Wave Reflections in Air", Univ. of Toronto, UTIAS Report No. 270, 1983.

30. Deschambault, R. L. & Glass, I. I., "An Update on Nonstationary Oblique Shock-Wave Reflections, Actual Isopycnics and Numerical Experiments", J. Fluid Mech., Vol. 131, p. 27, 1983.

31. Hu, T. C. J. & Glass, I. I., "An Interferometric and Numerical Study of Pseudo-Stationary Oblique-Shock-Wave Reflections in Sulfur Hexa-Fluoride (SF_6)", Proc. 15th International Symposium on Shock Waves and Shock Tubes, California, 1985.

32. Hu, T. C. J. & Glass, I. I., "Blast-Wave Trajectories from a Height-of-Burst", AIAA paper to be published.

33. Li, J. C. & Glass, I. I., "Collisions of Mach Reflections with a 90-Degree Ramp", Proc. 15th International Symposium on Shock Waves and Shock Tubes, California, 1985.

34. Liepmann, H. W. & Roshko, A., "Elements of Gasdynamics", John Wiley and Sons, Inc., New York, 1957.

35. Jones, D. M., Martin, P. M. E. & Thornhill, C. K., "A Note on the Pseudo-Stationary Flow Behind a Strong Shock Diffracted or Reflected at a Corner", Proc. Roy. Soc. London, Sec. A, Vol. 209, p. 238, 1951.

36. Glass, I. I. & Hall, J. G., "Handbook of Supersonic Aerodynamics -- Section 18 Shock Tubes", NAVORD Report 1488 (Vol. 6), Washington D. C., 1959.

37. Mirels, H., "Laminar Boundary Layer Behind Shock Advancing into Stationary Fluid", NACA TN 3401, 1955.

38. Mirels, H., "Boundary Layer Behind Shock or Thin Expansion Wave Moving into Stationary Fluid", NACA TN 3712, 1956.

39. Deschambault, R. L., [private communication], 1983.

40. Boyer, A. G., "Design, Instrumentation and Performance of the UTIAS 4 in x 7 in Hypersonic Shock Tube", Univ. of Toronto, UTIAS Rept. No. 158, 1971.

41. Ben-Dor, G. & Whitten, B. T., "Interferometric Techniques and Data Evaluation Methods for the UTIAS 10 cm x 18 cm Hypervelocity Shock Tube", Univ. of Toronto, UTIAS Tech. Note No. 208, 1979.

42. Ikui, K , Matsuo, K., Aoki, T. & Kondoh, N., "Mach Reflection of a Shock Wave from an Inclined Wall", Memoirs of the Faculty of Engineering, Kyushu University, Vol. 41, No. 4, Dec. 1981.

43. Glaz, H. M., Colella, P., Glass, I. I. & Deschambault, R. L., "A Numerical Study of Oblique Shock-Wave Reflections with Experimental Comparisons", Proc. Roy. Soc. London, Sec. A, Vol. 398, p. 117, 1985.

44. Henderson, L. F., "The Three-Shock Confluence on a Simple Wedge Intake", The Aeronautical Quarterly, February, 1965.

45. White, D. R. & Millikan, R. C., "Vibrational Relaxation in Air", AIAA J., Vol. 2, p. 1844, 1964.

46. Lifshitz, A., ed., "Shock Waves in Chemistry", Marcel Dekker Inc., New York, 1981.

47. Vincenti, W. G. & Kruger, C. H., "Introduction to Physical Gas Dynamics", John Wiley and Sons, Inc., New York, 1965.

48. Du, X., Liu, W. S. & Glass, I. I., "Laminar Boundary Layers Behind Blast and Detonation Waves", UTIAS Report No. 259, 1982.

49. Liu, W. S., Du, X. X. & Glass, I. I., "Laminar Boundary Layers Behind Detonation Waves", Proc. Roy. Soc. London, Sec. A, Vol. 209, p.238, 1983.

50. Schlichting, H. R., "Boundary-Layer Theory", McGraw-Hill Book Company, New York, 1979.

51. Seiler, F., "Pseudo-Stationary Mach Reflexion of Shock Waves", Proc. 15th International Symposium on Shock Waves and Shock Tubes, California, 1985.

Table 1

SUMMARY OF EXPERIMENTS

Exp. No.	θ_w (deg)	M_s	p_0 (kPa)	T_0 (deg C)	ω' (deg)	χ (deg)	Reflection Type
33	42	1.185	100.82	22.4	58.2	----	RR
36	42	1.187	100.82	25.5	57.2	----	RR
34	42	1.205	77.62	25.0	----	0.15	SMR
35	42	1.229	70.28	24.0	----	0.17	SMR
32	42	1.235	66.95	23.4	----	0.27	SMR
31	42	1.268	50.28	22.1	----	0.55	SMR
30	42	1.301	38.67	22.9	----	0.62	SMR
59	45	1.280	46.68	25.3	53.5	----	RR
58	45	1.299	40.01	25.1	55.5	----	RR
21	45	1.315	17.08	23.8	55.2	----	RR
5	45	1.317	34.41	23.7	----	0.19	SMR
6	45	1.334	31.87	24.5	----	0.25	SMR
20	45	1.344	31.77	23.2	----	0.16	SMR
22	45	1.358	28.54	22.5	----	0.22	SMR
24	45	1.373	25.07	24.4	----	0.28	SMR
25	45	1.392	23.61	23.1	----	0.31	SMR
28	45	1.393	24.27	23.0	----	0.39	SMR
27	45	1.398	23.47	22.6	----	0.41	SMR
26	45	1.403	21.74	23.1	----	0.34	SMR
19	45	1.408	21.44	23.9	----	0.37	SMR
23	45	1.410	30.14	23.8	----	0.45	SMR
8	45	1.435	18.67	25.4	----	0.45	SMR

Exp. No.	θ_w (deg)	M_s	p_0 (kPa)	T_0 (deg C)	ω' (deg)	χ (deg)	Reflection Type
63	45	6.132	0.52	24.5	----	0.48	DMR
61	45	6.184	0.51	24.4	----	0.27	DMR
54	45	6.195	0.48	25.0	----	0.64	DMR
62	45	6.213	0.45	24.8	34.3	----	RR
56	45	6.236	0.43	24.5	33.9	----	RR
57	45	6.283	0.41	25.2	33.9	----	RR
55	45	6.399	0.36	25.1	----	0.21	DMR
60	45	6.411	0.36	24.0	34.4	----	RR
10	47	1.407	9.87	24.2	49.1	----	RR
39	47	1.453	58.15	25.4	----	0.18	SMR
17	47	1.464	16.54	22.7	48.8	----	RR
11	47	1.471	7.41	23.0	49.5	----	RR
40	47	1.509	12.96	25.9	----	0.17	SMR
38	47	1.533	17.26	24.7	----	0.27	SMR
12	47	1.540	11.04	23.9	----	0.19	SMR
18	47	1.556	19.87	22.7	----	0.45	SMR
15	47	1.583	18.52	22.8	----	0.59	CMR
13	47	1.588	9.20	23.0	----	0.40	CMR
16	47	1.594	17.34	22.8	----	0.59	CMR
14	47	1.668	7.20	23.3	----	0.56	CMR
44	47	4.645	2.01	24.1	33.1	----	RR
43	47	4.665	2.03	24.8	----	1.16	DMR
52	47	4.800	2.00	25.8	----	1.63	DMR
42	47	4.846	2.03	26.3	----	1.00	DMR
45	47	4.959	2.03	25.0	----	1.31	DMR
47	47	5.085	1.87	27.0	----	1.21	DMR

Exp. No.	θ_w (deg)	M_s	p_0 (kPa)	T_0 (deg C)	ω' (deg)	χ (deg)	Reflection Type
64	47	5.215	1.59	22.5	----	0.97	DMR
48	47	5.249	1.60	26.8	----	1.23	DMR
65	47	5.279	1.47	22.9	32.1	----	RR
49	47	5.314	1.47	27.0	----	0.73	DMR
66	47	5.338	1.41	22.0	----	0.53	DMR
68	47	5.339	1.29	24.3	----	0.41	DMR
67	47	5.366	1.33	23.4	----	0.81	DMR
51	47	5.381	1.33	24.0	31.7	----	RR
71	47	5.416	1.25	24.0	31.6	----	RR
70	47	5.497	1.19	23.7	32.4	----	RR
69	47	5.545	1.09	23.3	33.6	----	RR
95	48	1.445	74.68	24.2	47.0	----	RR
91	48	1.466	69.35	24.3	47.0	----	RR
97	48	1.472	66.68	24.6	47.1	----	RR
99	48	1.474	68.68	24.9	47.8	----	RR
100	48	1.479	82.68	25.4	48.0	----	RR
94	48	1.483	74.68	23.5	49.1	----	RR
98	48	1.483	66.68	24.0	47.3	----	RR
93	48	1.494	70.68	24.2	----	0.20	SMR
101	48	1.500	74.68	25.5	47.8	----	RR
96	48	1.531	76.02	24.5	----	0.22	SMR
85	48	1.539	11.34	23.0	48.2	----	RR
90	48	1.547	72.02	24.0	----	0.29	SMR
89	48	1.565	18.67	23.5	47.8	----	RR
82	48	1.587	17.34	23.4	47.6	----	RR

Exp. No.	θ_w (deg)	M_s	p_0 (kPa)	T_0 (deg C)	ω' (deg)	χ (deg)	Reflection Type
86	48	1.597	16.54	23.3	----	0.27	SMR
88	48	1.615	15.34	22.8	----	0.33	SMR
84	48	1.650	13.34	23.6	----	0.20	CMR
83	48	1.677	11.34	23.5	----	0.32	CMR
87	48	1.700	9.87	22.7	----	0.49	CMR
81	48	1.778	7.33	23.3	----	0.50	CMR
106	48	2.366	6.67	24.6	----	1.18	DMR
104	48	2.619	4.67	25.4	35.7	----	RR
105	48	2.637	4.67	25.6	----	1.37	DMR
110	48	3.103	3.07	24.6	----	1.47	DMR
115	48	3.627	1.73	24.3	----	0.53	DMR
113	48	3.732	1.60	23.0	----	0.74	DMR
114	48	3.810	1.47	23.9	----	1.04	DMR
112	48	3.897	1.33	22.9	35.7	----	RR
116	48	3.951	1.20	24.4	34.2	----	RR
78	48	4.012	6.67	22.4	----	1.69	DMR
117	48	4.085	1.07	24.7	34.7	----	RR
77	48	4.211	5.33	23.0	----	1.81	DMR
79	48	4.371	3.73	24.8	----	0.36	DMR
76	48	4.414	4.27	22.4	33.2	----	RR
73	48	4.489	3.75	23.0	----	0.89	DMR
75	48	4.615	3.27	20.1	30.5	----	RR
80	48	4.627	1.16	24.9	31.1	----	RR
74	48	4.791	2.60	22.3	----	0.11	DMR
72	48	5.045	2.00	24.7	----	0.13	DMR

Table 2

TRANSITION BOUNDARY POINTS

Exp. No.	θ_w (deg)	M_s	p_0 (kPa)	ω' (deg)
36	42	1.19	100.82	57.7
58	45	1.30	40.01	54.5
17	47	1.46	16.54	48.8
94	48	1.48	74.68	48.1
82	48	1.59	17.34	47.7
112	48	3.90	1.33	34.9
71	47	5.42	1.25	31.9
62	45	6.21	0.45	34.0
* 966	49	3.71	6.00	31.0

* Taken from Deschambault [29]
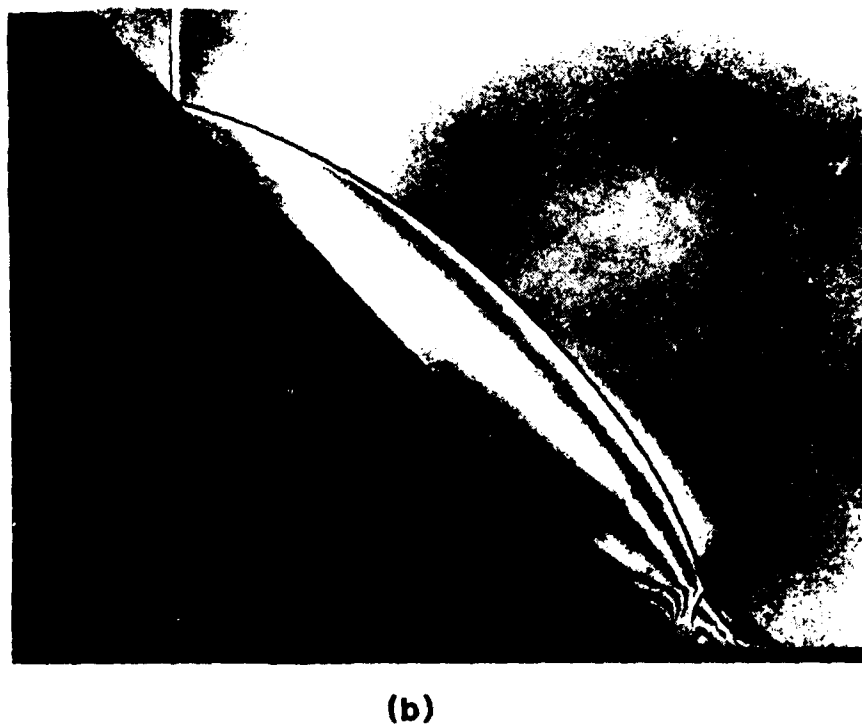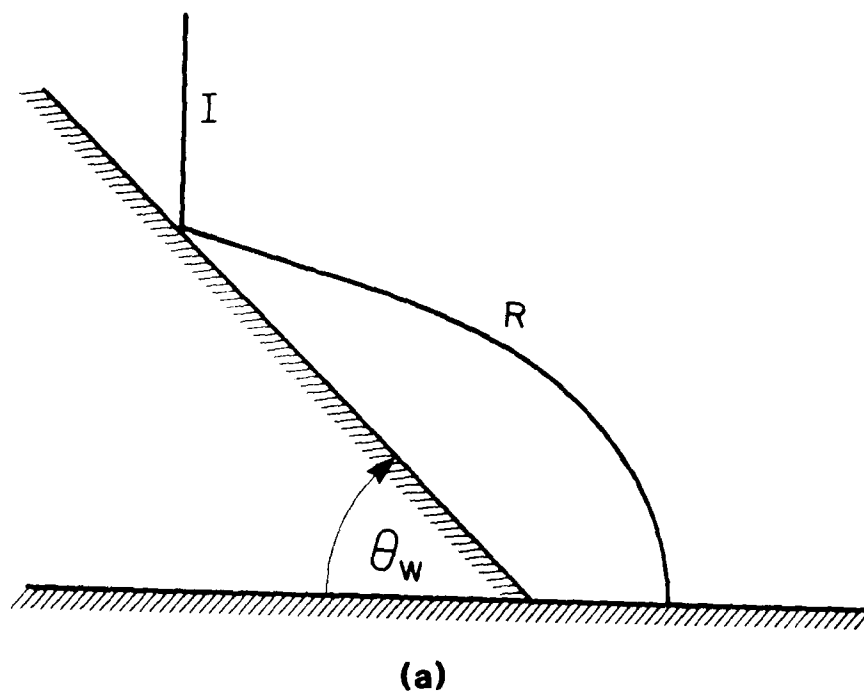
Figure 1:   Regular Reflection (RR)

(a) Schematic diagram

(b) Interferogram

(θ_w = 47°, M_s = 5.55, p_0 = 1.1 kPa, T_0 = 297 K)

I - incident shock wave, R - reflected shock wave,
θ_w - wedge angle
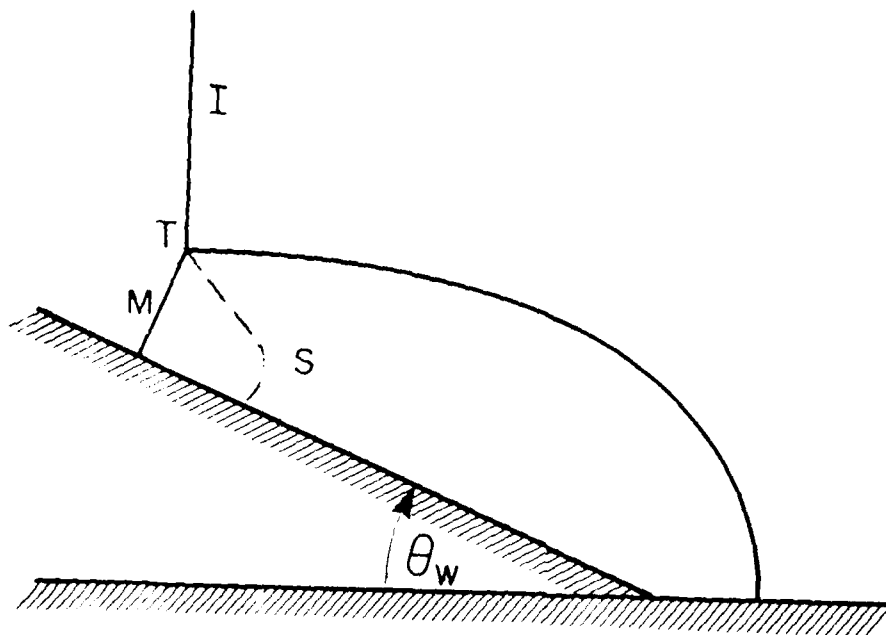
Figure 2: Single-Mach Reflection (SMR)

(a) Schematic diagram

(b) Interferogram (Ref. 29)

($\theta_w = 20°$, $M_s = 3.00$, $p_0 = 20.0$ kPa, $T_0 = 299$ K)

I - incident shock wave, R - reflected shock wave,
M - Mach stem, S - slipstream, T - triple point,
θ_w - wedge angle
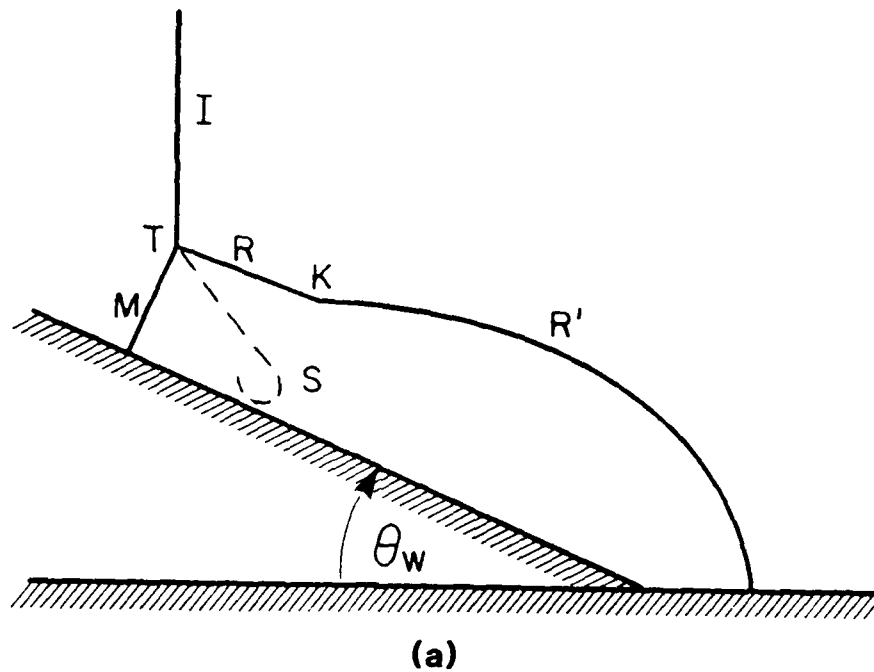
Figure 3:   Complex-Mach Reflection (CMR)

(a) Schematic diagram

(b) Interferogram (Ref. 29)

$(\theta_w = 30^\circ$, $M_s = 3.09$, $p_0 = 8.0$ kPa, $T_0 = 296$ K$)$

θ_w - wedge angle, I - incident shock wave,
R, R' - first and second reflected shock waves,
M - Mach stem, S - slipstream, T - triple point, K - kink
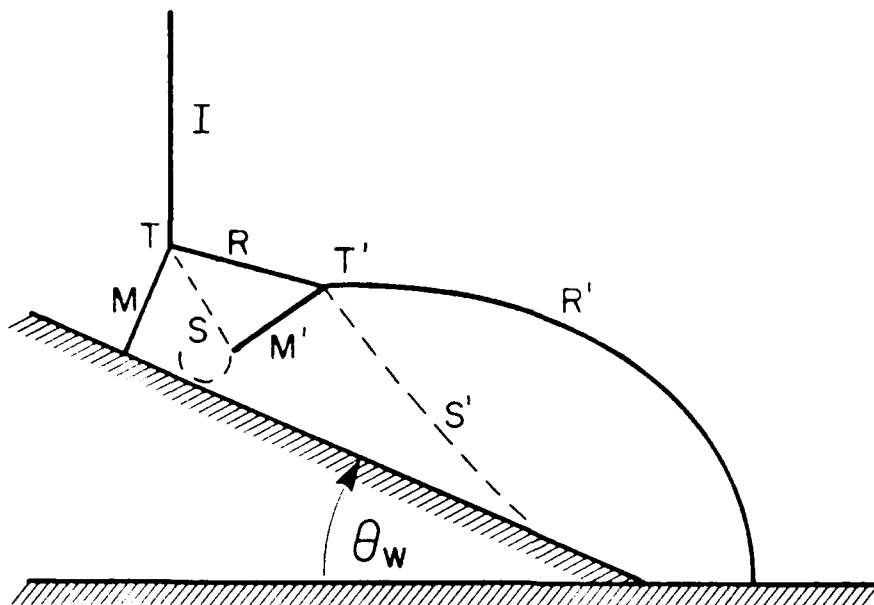
(a)

(b)

Figure 4: Double-Mach Reflection (DMR)

(a) Schematic diagram

(b) Interferogram (Ref. 29)
($\theta_w = 40°$, $M_s = 5.50$, $p_0 = 1.33$ kPa, $T_0 = 298$ K)

θ_w - wedge angle, I - incident shock wave,
R, R' - first and second reflected shock waves,
M, M' - first and second Mach stems,
T, T' - first and second triple points,
S, S' - first and second slipstreams
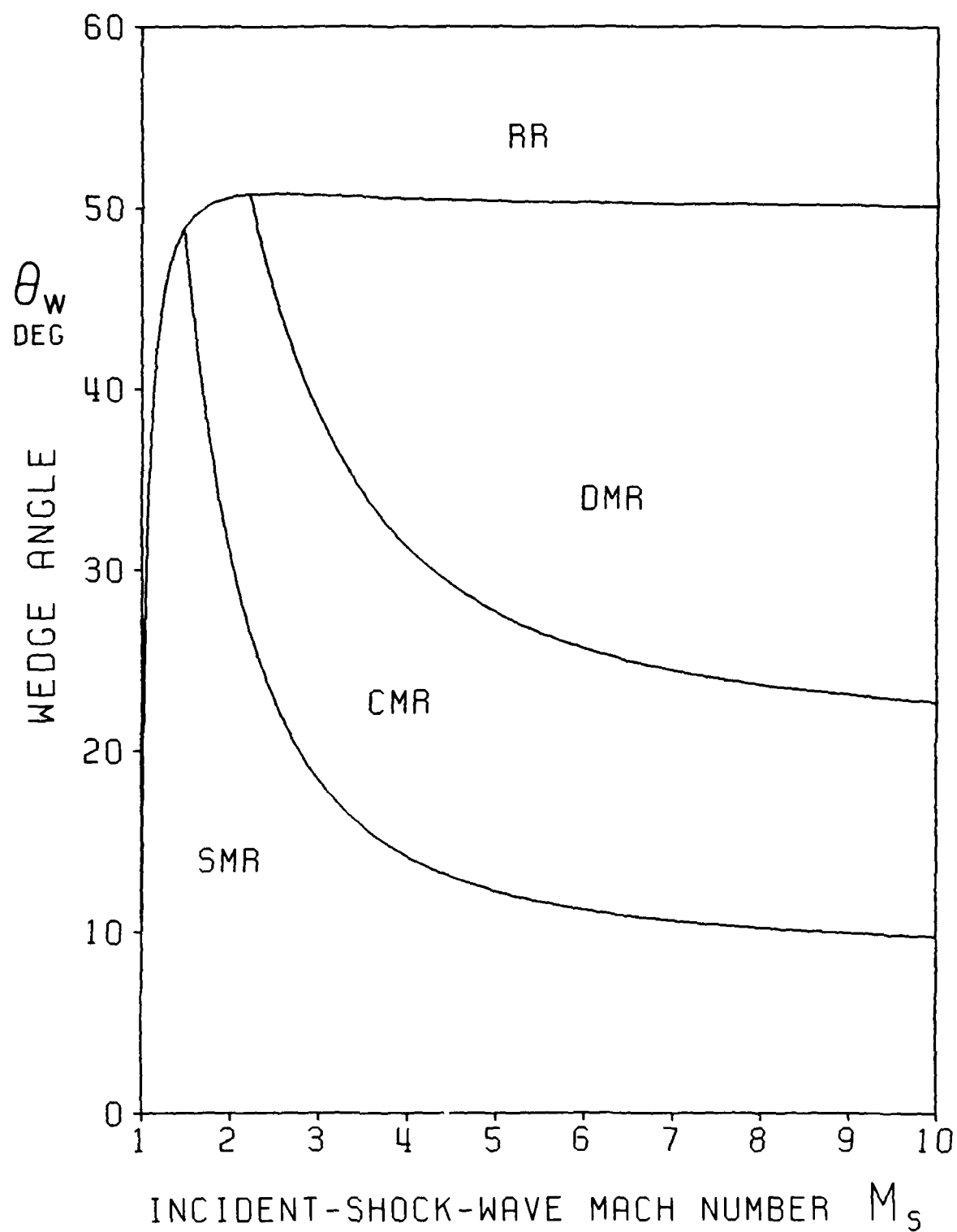
Figure 5: Regions of various types of shock-wave reflection
in frozen inviscid flow in air [Ref. 30]

$M_I > 1$

$\theta_w < \theta_s$

$M_I \longleftarrow$

θ_w

(a)

$M_I > 1$

$\theta_s < \theta_w < \theta_m$

$M_I \longleftarrow$

θ_w

(b)

$M_I < 1$

OR

$M_I > 1$

$\theta_w > \theta_m$

$M_I \longleftarrow$

θ_w

(c)
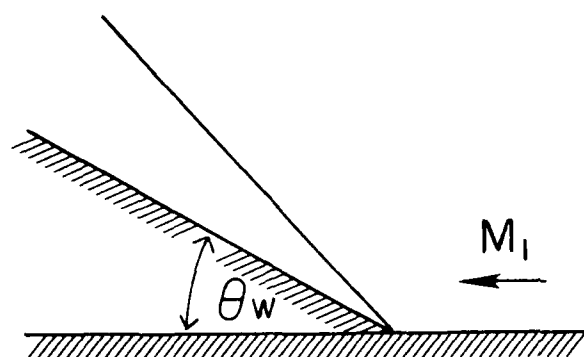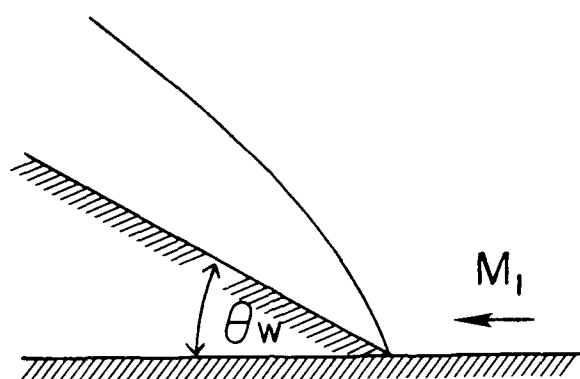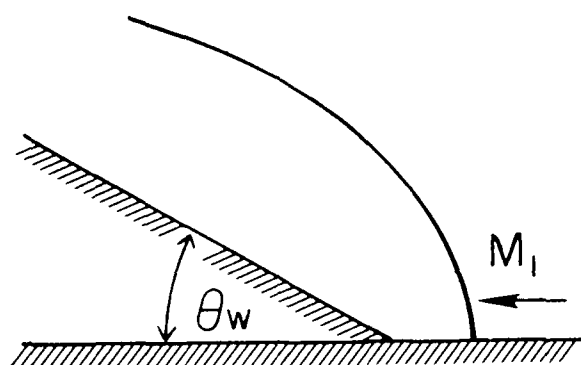
Figure 6: Possible bow-shock configurations

(a) straight, attached shock

(b) curved, attached shock

(c) curved, detached shock
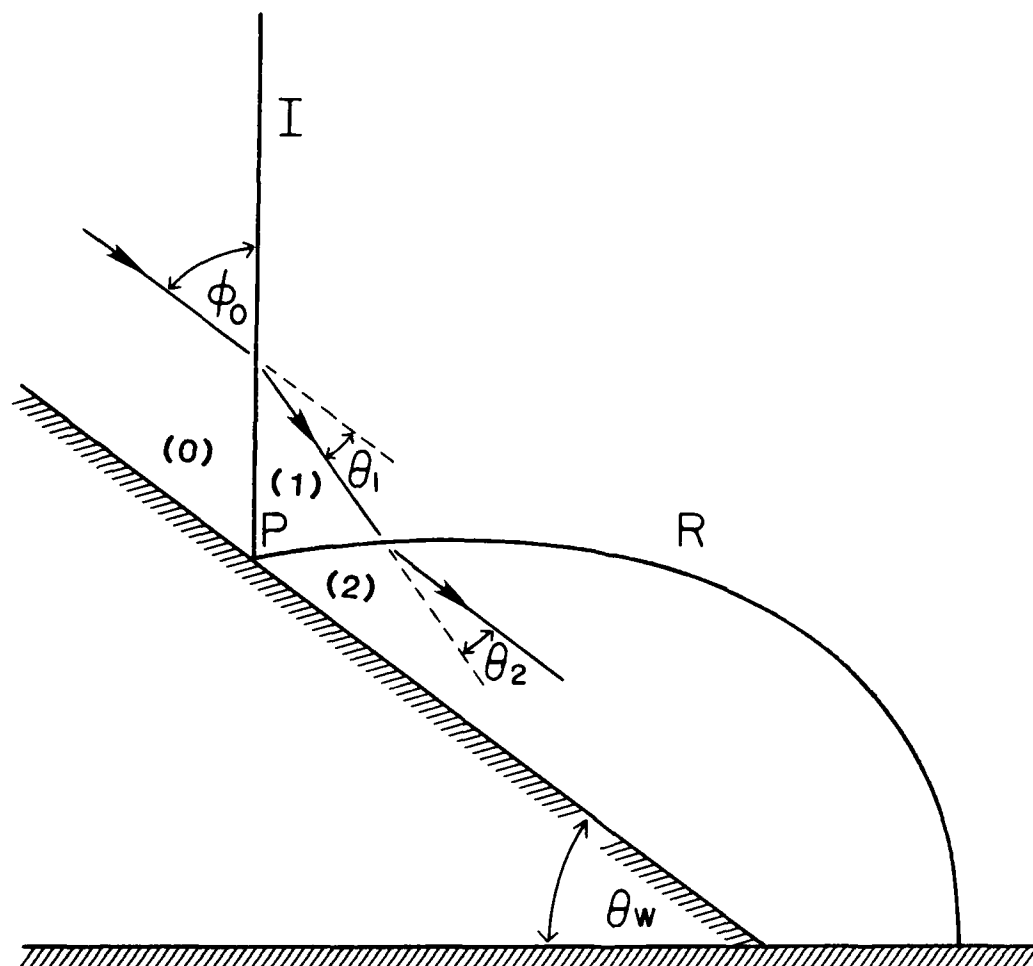
Figure 7: Schematic diagram of regular reflection (RR)
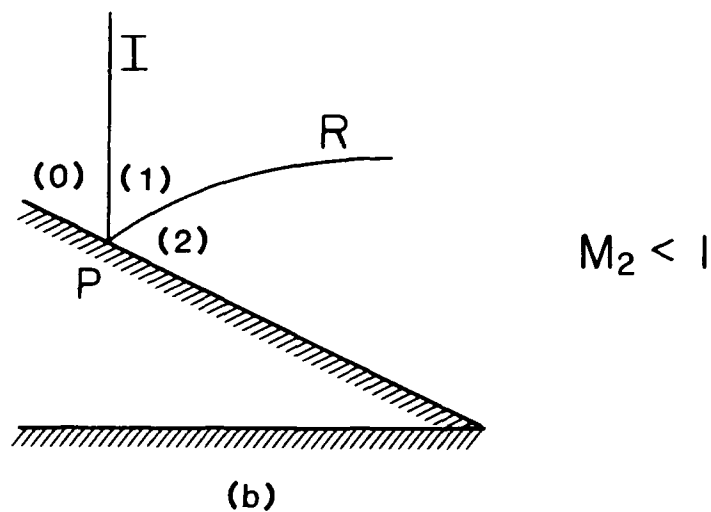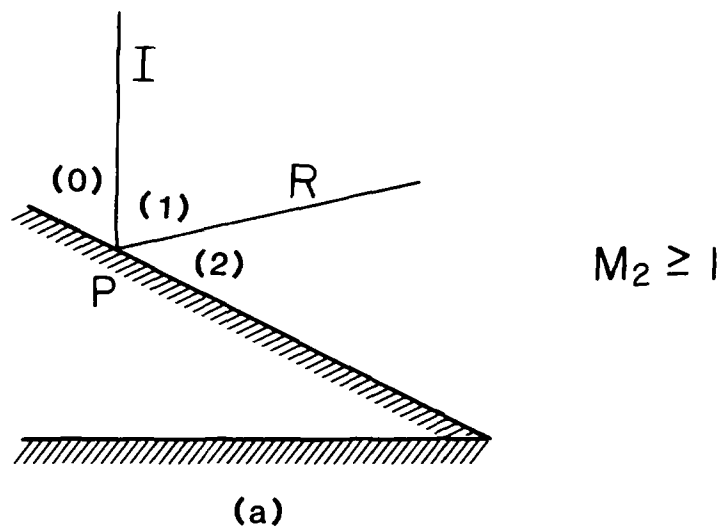
Figure 8: Two possible reflected-shock-wave configurations
at point P in RR

(a) straight reflected shock

(b) curved reflected shock
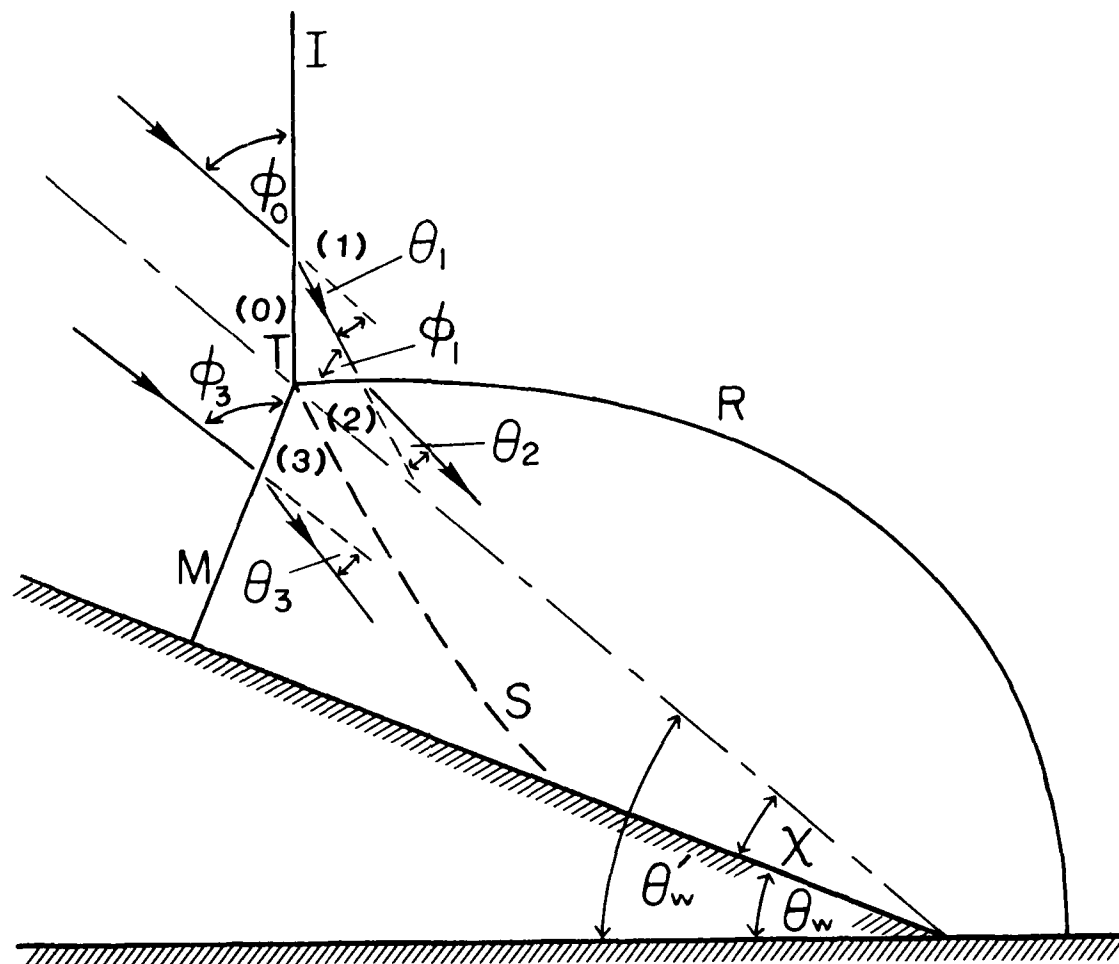
Figure 9: Schematic diagram of single-Mach reflection (SMR)
I - incident shock wave, R - reflected shock wave,
M - Mach stem, S - slipstream, T - triple point,
θ_w - wedge angle, X - triple-point trajectory angle,
ϕ - incidence angle, θ - deflection angle

Figure 10: Schematic diagram of complex-Mach reflection (CMR)
I - incident shock wave, R - reflected shock wave,
M - Mach stem, S - slipstream, K - kink, T - triple point,
θ_w - wedge angle, X - triple-point trajectory angle,
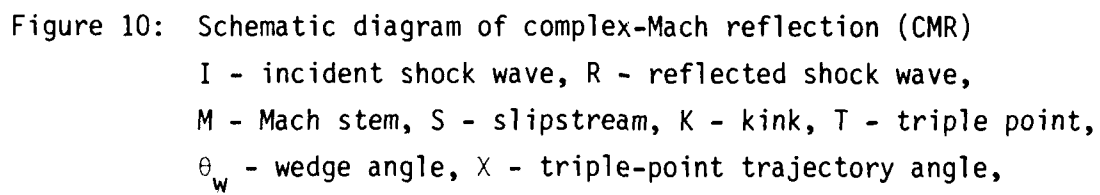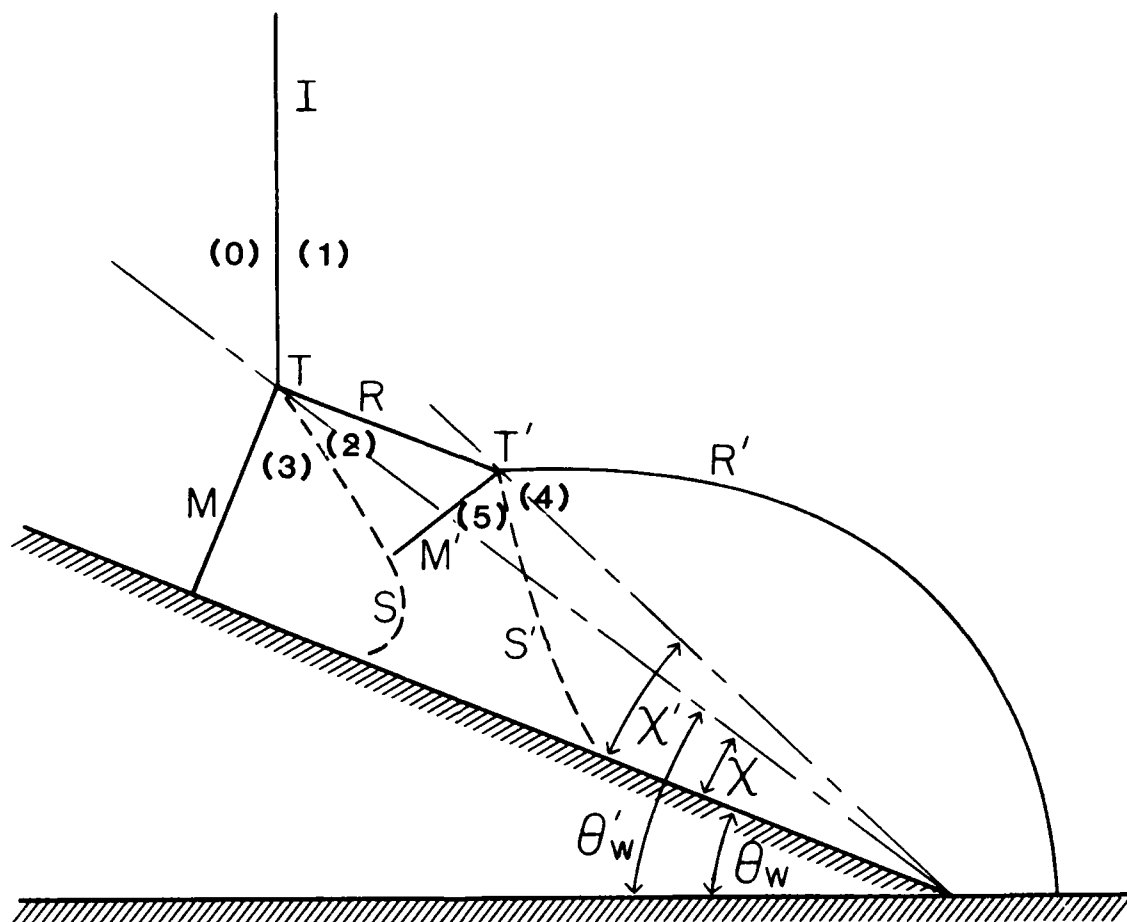
Figure 11: Schematic diagram of double-Mach reflection (DMR)

θ_w - wedge angle, I - incident shock wave,

R, R' - first and second reflected shock waves,

M, M' - first and second Mach stems,

T, T' - first and second triple points,

S, S' - first and second slipstreams,

X, X' - first and second triple-point trajectory angles
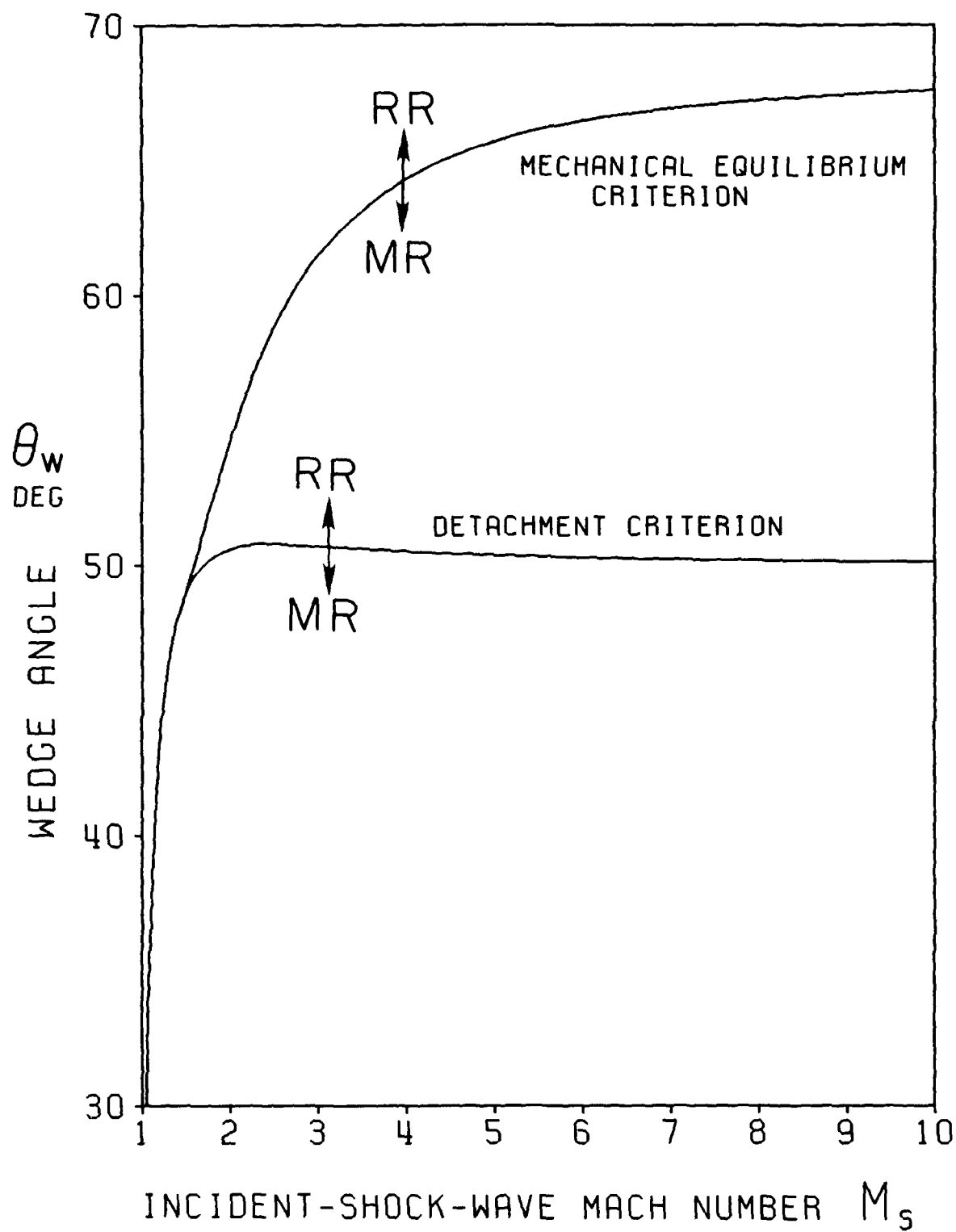
Figure 12: Regular to Mach reflection transition boundary as defined by two theoretical inviscid criteria
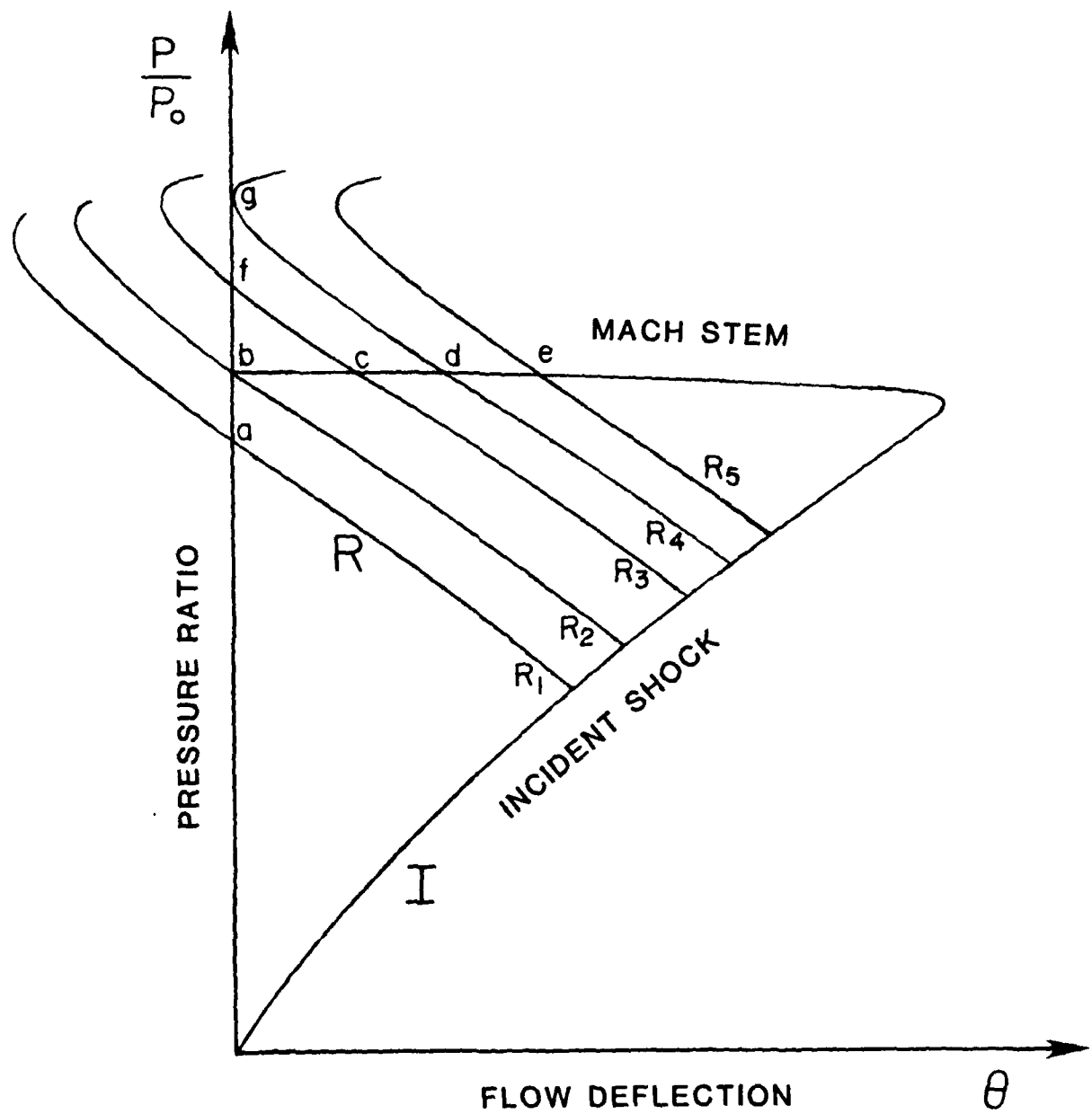
Figure 13: Schematic shock-polar diagram to define several possible flow configurations [Ref. 34]
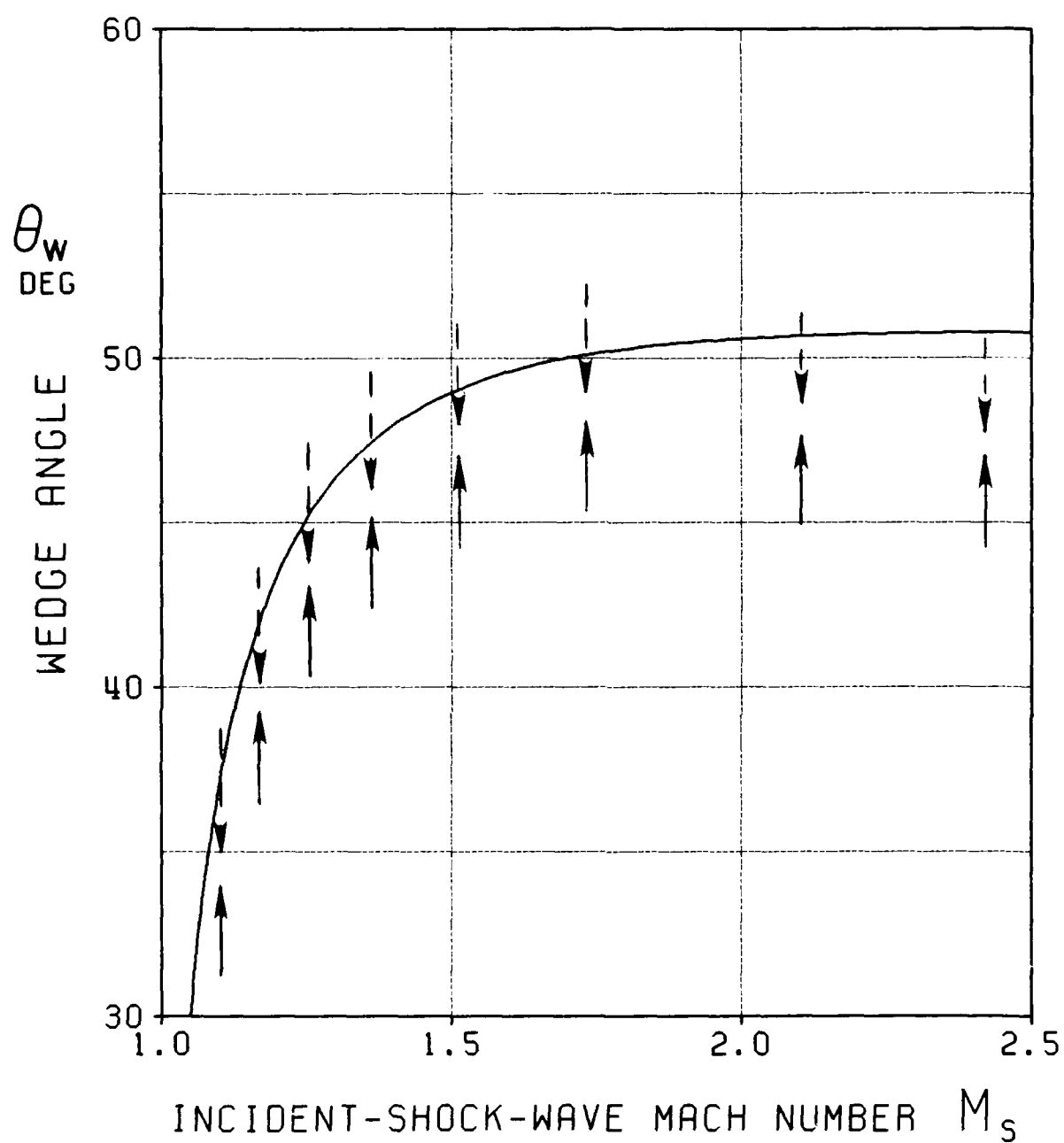
Figure 14: Deviation of experimental results of Smith [8]
from the 'detachment' criterion RR◄►MR boundary.

Experiments were not performed in gaps between arrows.

── ─► lower limit of RR

─────► upper limit of MR
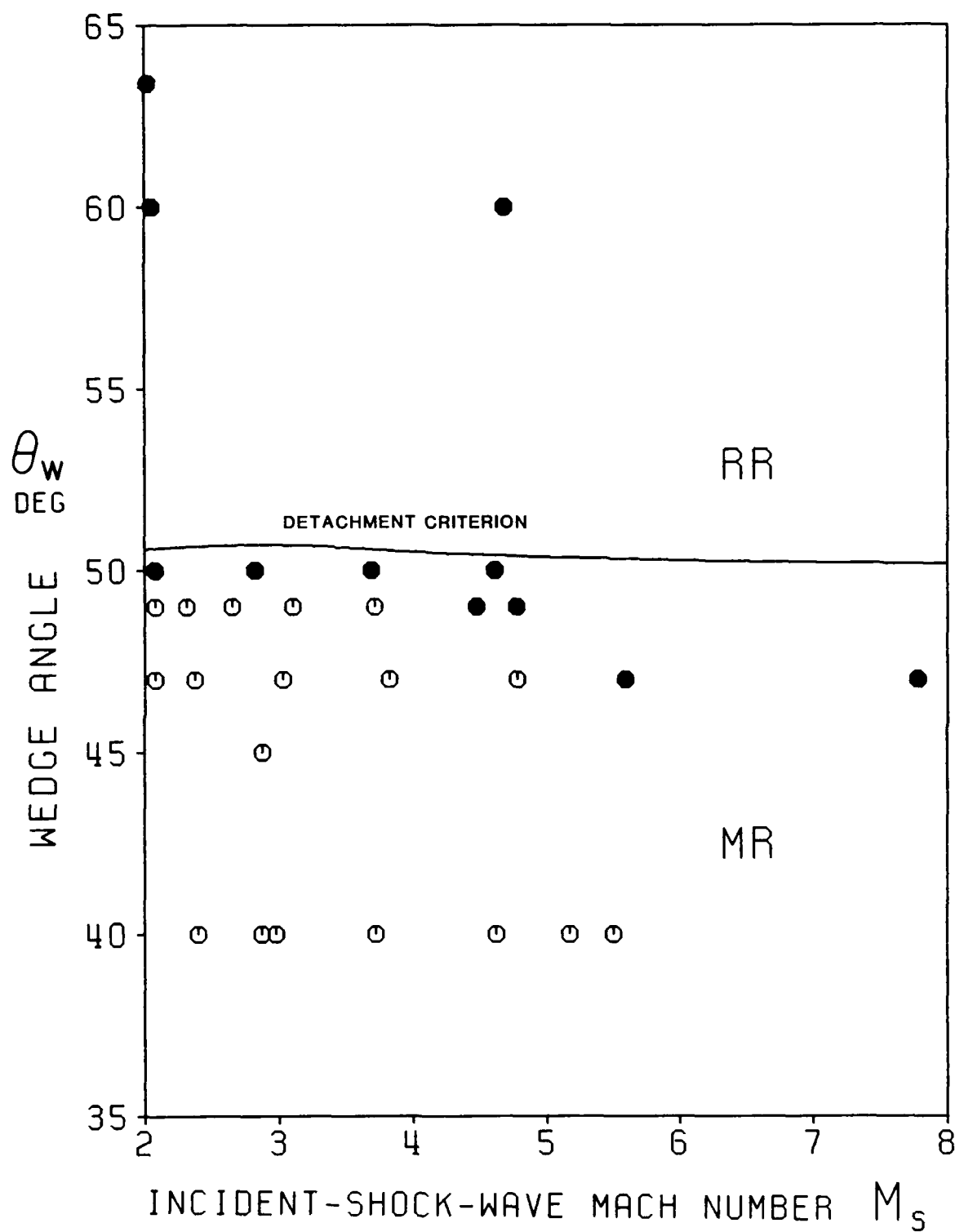
Figure 15: Deviation of experimental results of Deschambault [29] from the 'detachment' criterion boundary

RR ● , MR ◯
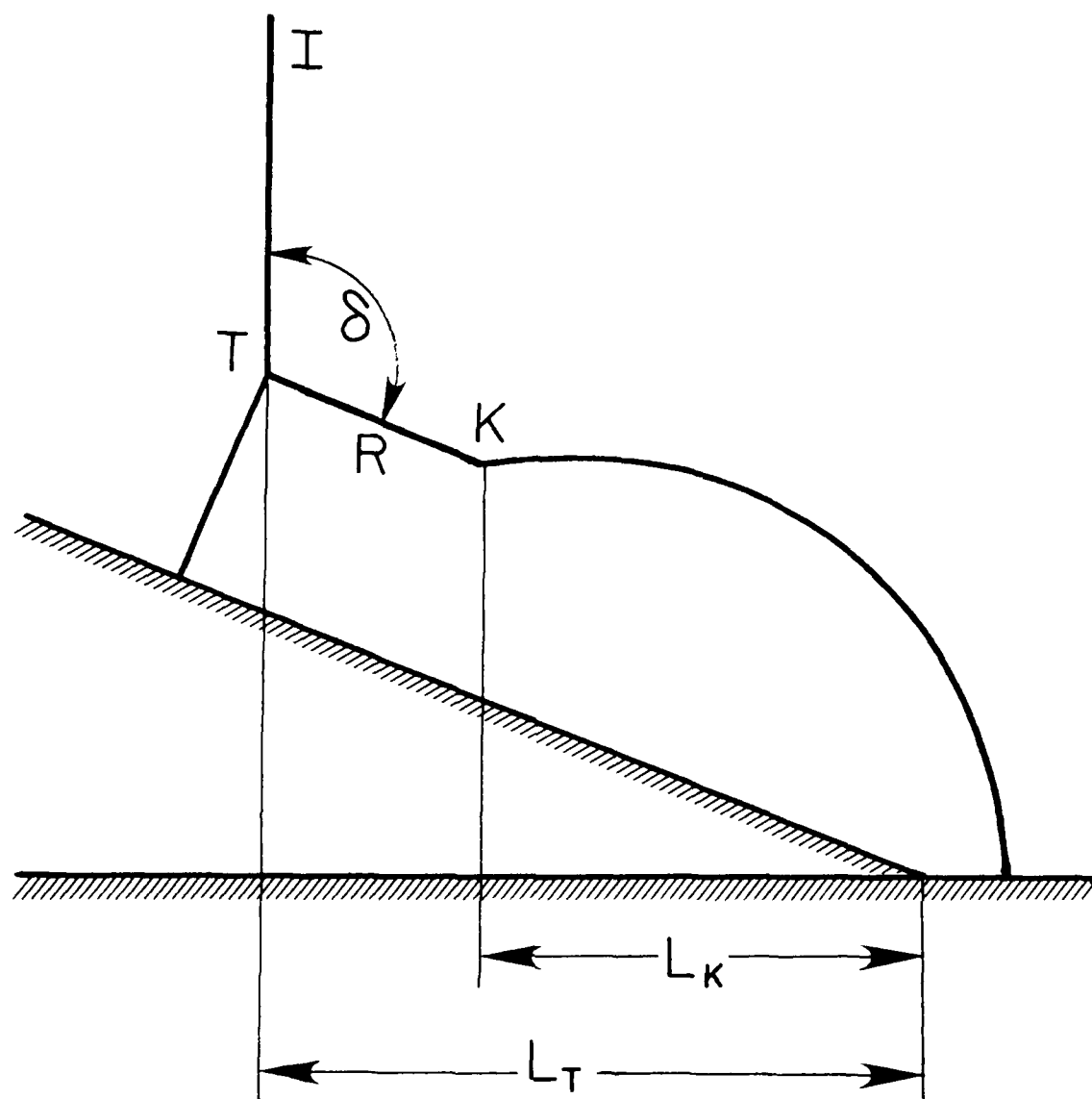
Figure 16: Definition of lengthscales used in Eq. 2.8
to define the position of T and K in CMR
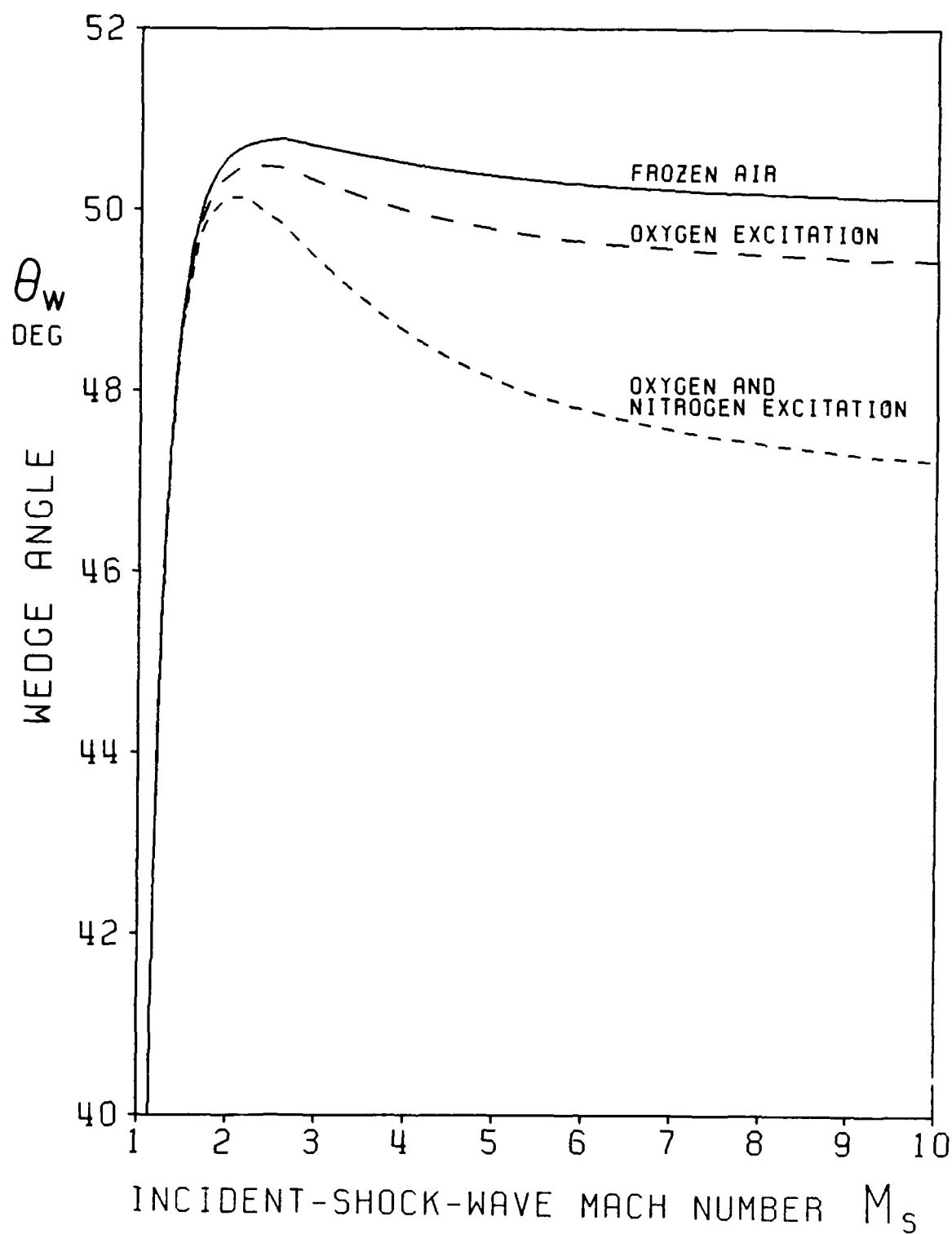
Figure 17: Effect of equilibrium vibrational excitation of O_2 and N_2 on the RR↔MR transition boundary
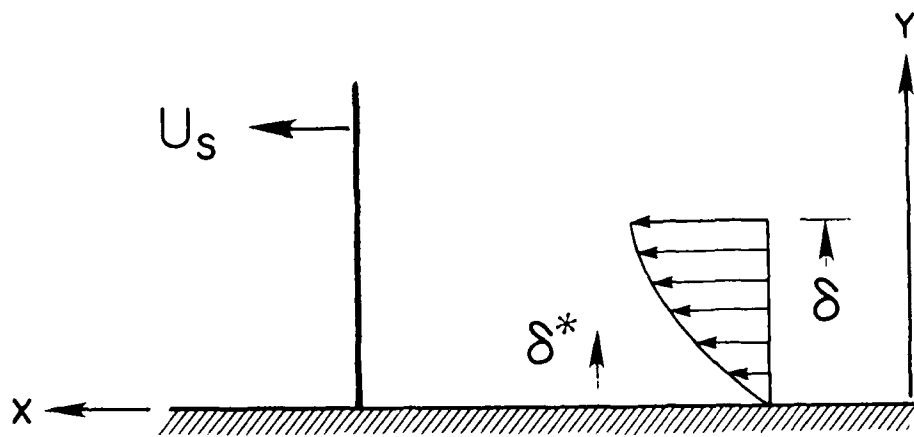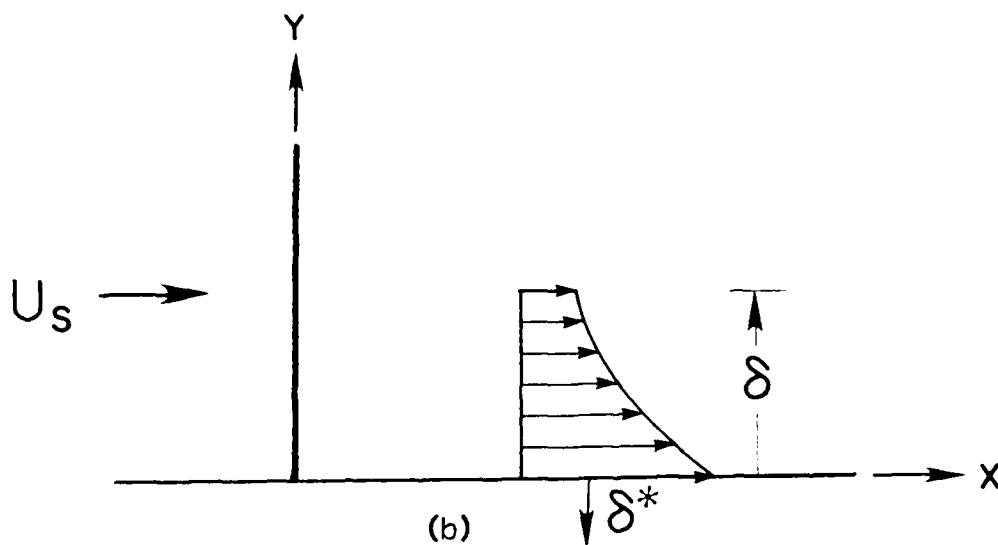
Figure 18: Boundary-layer velocity distribution in moving and stationary reference frames [37]

(a) Laboratory-fixed reference frame

(b) Shock-fixed reference frame

δ - boundary-layer height

δ^* - boundary-layer displacement thickness
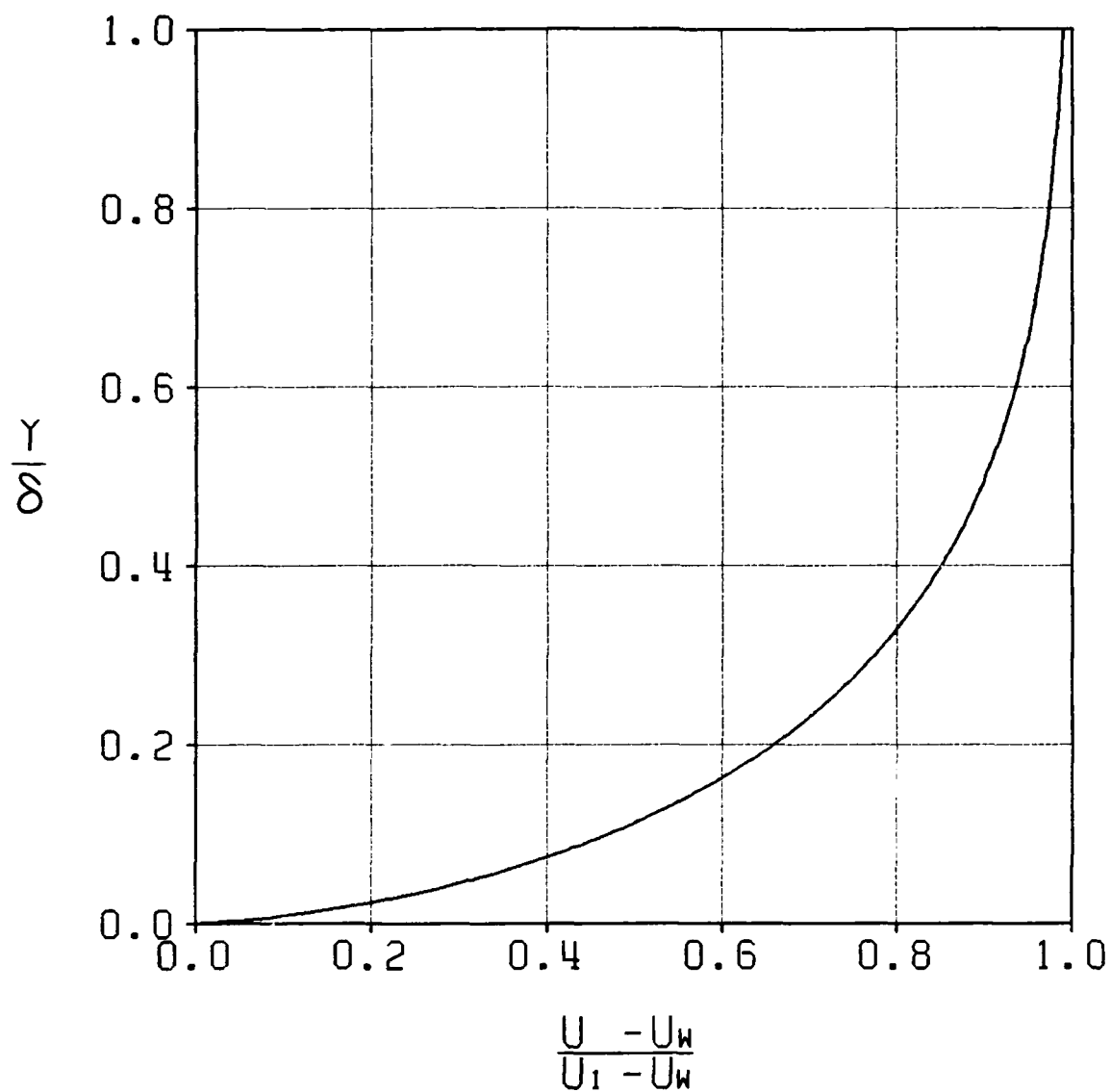
Figure 19: Laminar-boundary-layer velocity profile behind a
shock wave travelling at M_s = 2.0 in+o air at
p_0 = 2 kPa, T_0 = 300 K

- based on Mirels [37, 38]

Figure 20: Laminar-boundary-layer temperature profile behind a shock wave travelling at M_s = 2.0 into air at P_0 = 2 kPa, T_0 = 300 K

- based on Mirels [37, 38]
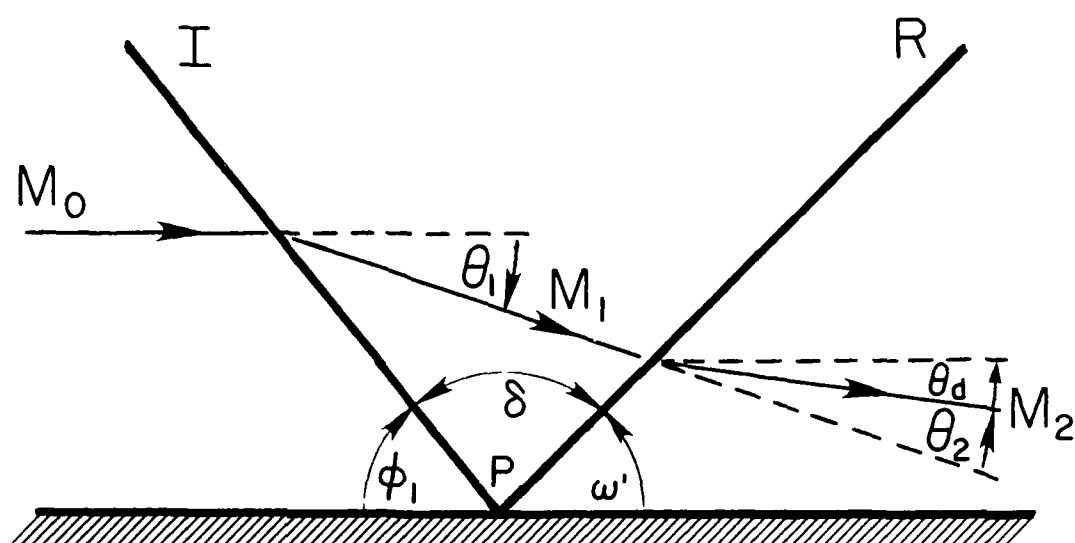
Figure 21:   Definition of displacement wedge angle θ_d

ω' - reflected-shock-wave angle

M_i - Mach number in region i

P - reflection poirt

θ_i - flow deflection angle in region i
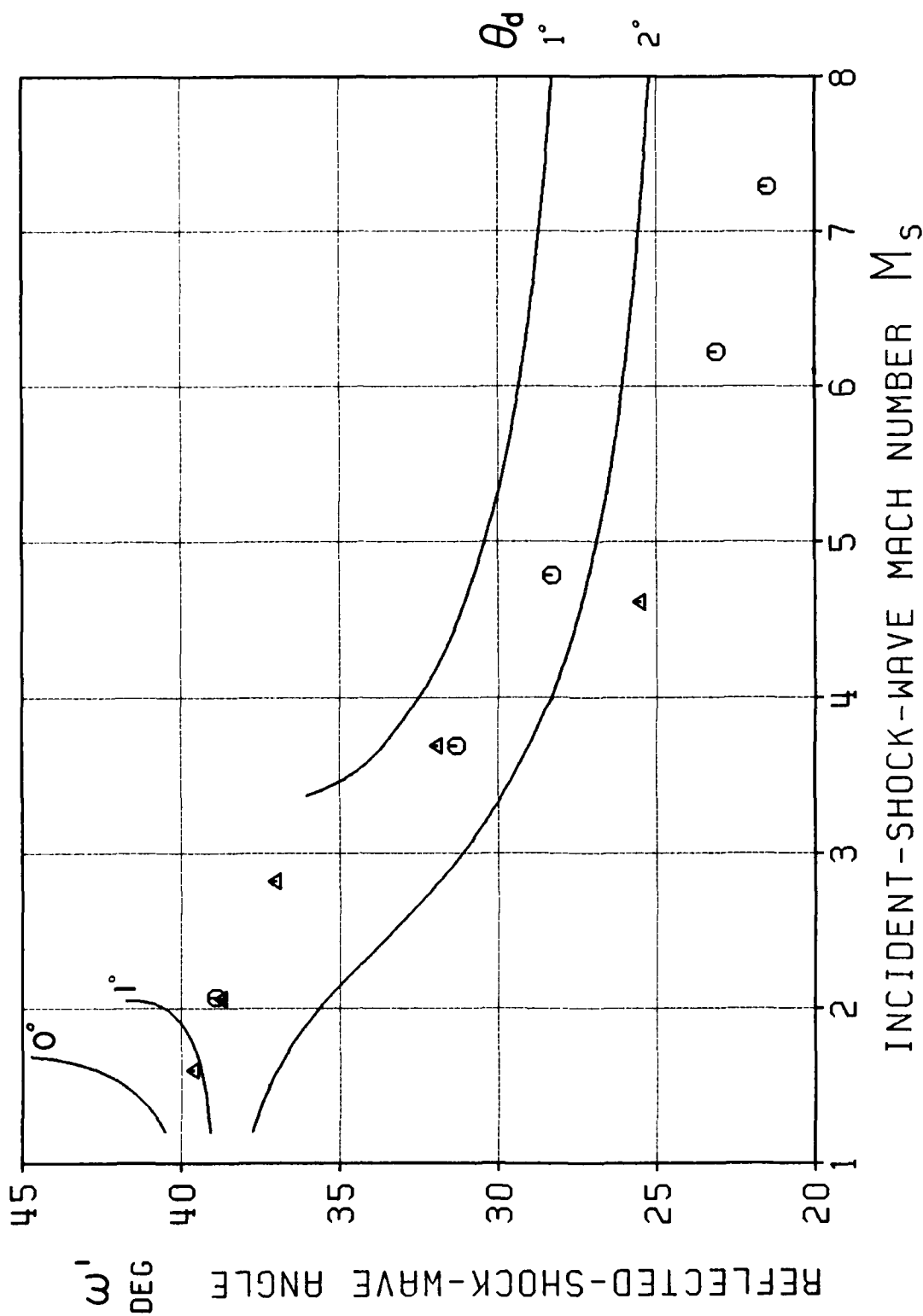
Figure 22: Experimental deviation of reflected-shock-wave angle ω' in air and nitrogen from the theoretical inviscid solution for 50° wedge angle

△ Ben-Dor [22]
○ Deschambault [29]
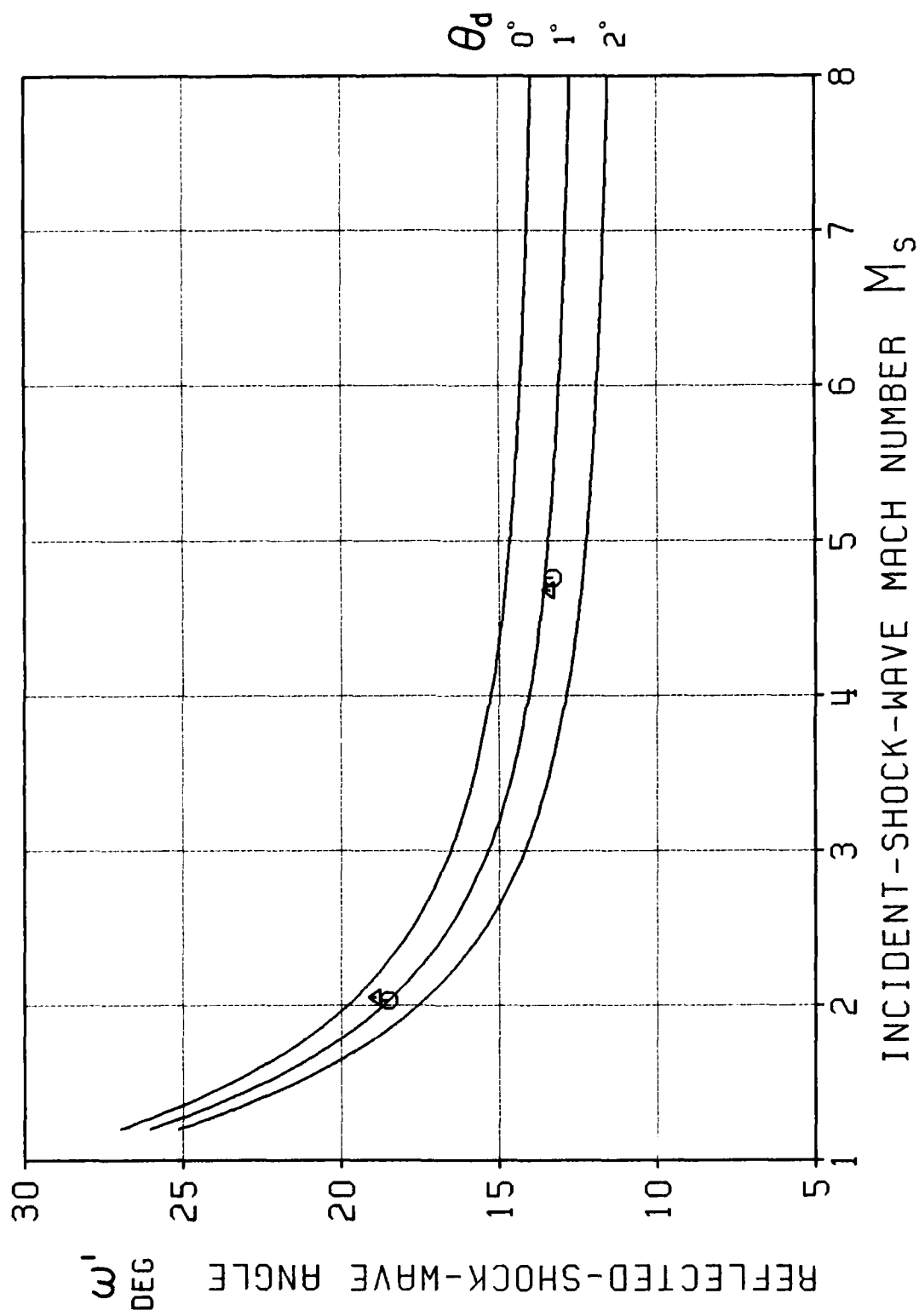
Figure 23: Experimental deviation of reflected-shock-wave angle ω' in air and nitrogen from the theoretical inviscid solution for $60°$ wedge angle

△ Ben-Dor [22]
○ Deschambault [29]
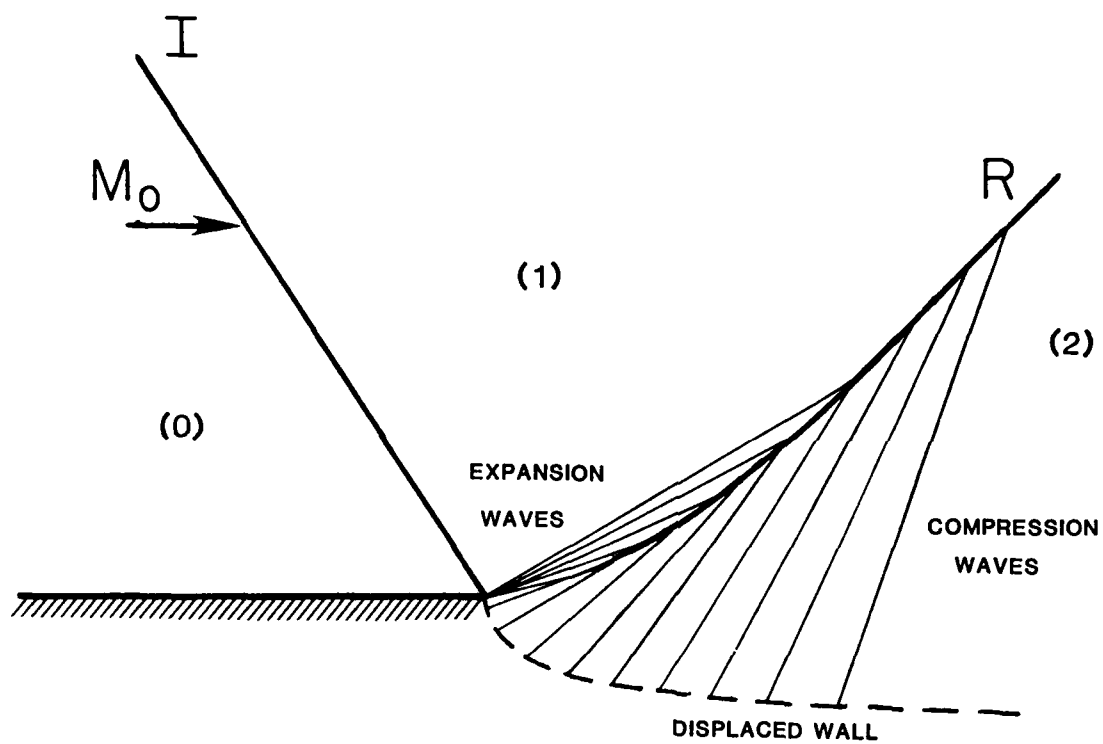
Figure 24: Physical model of the RR reflection process at point P in the presence of a laminar boundary layer [19]
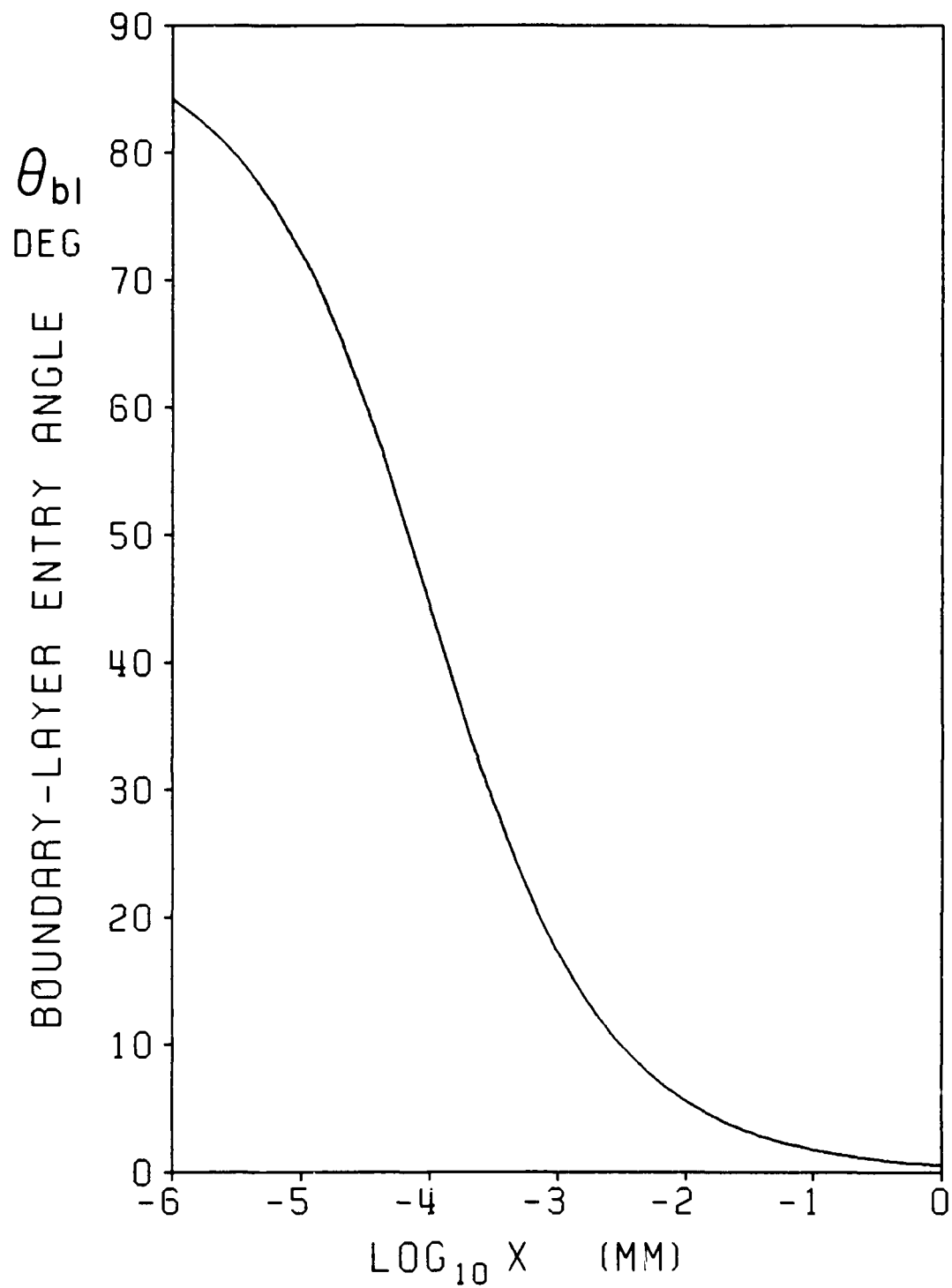
Figure 25: Distribution of boundary-layer entry angle θ_{bl} for a laminar boundary layer in air
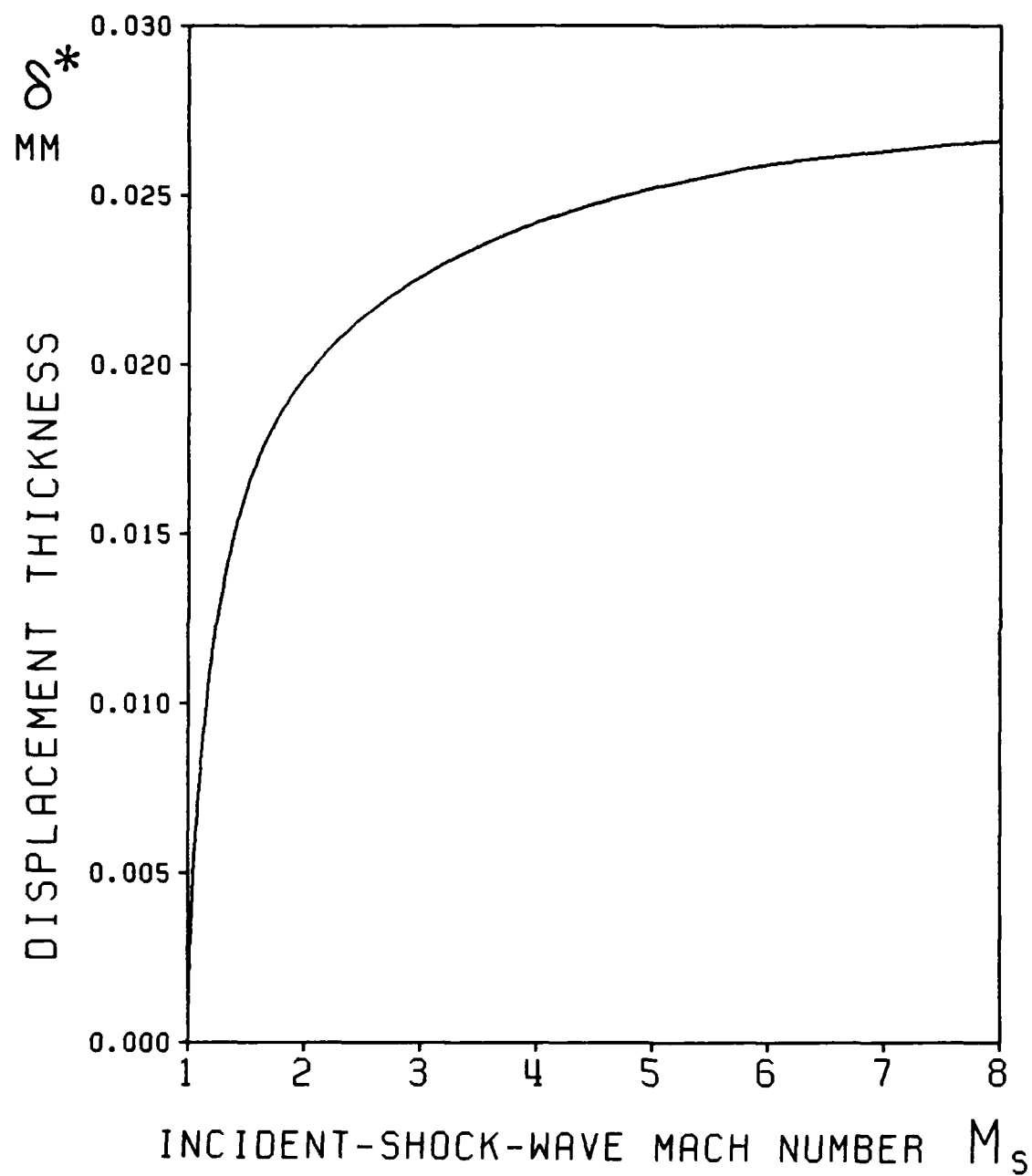
Figure 26: Predicted boundary-layer displacement thickness δ^* at distance of 1 mm from regular reflection point P (p_0 = 2.0 kPa, T_0 = 300 K)
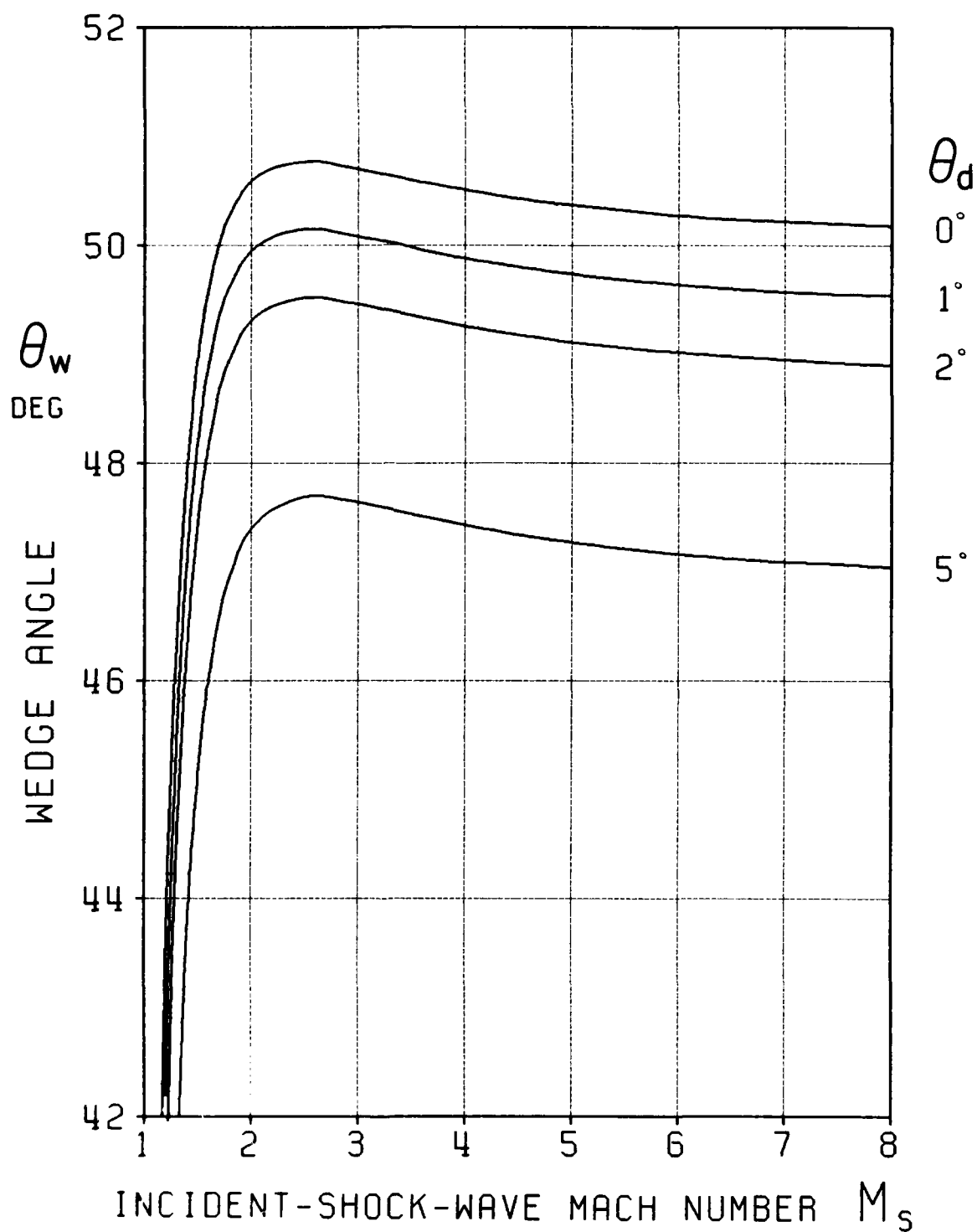
Figure 27: Effect of displacement wedge angle θ_d on the RR◄►MR transition boundary in frozen air
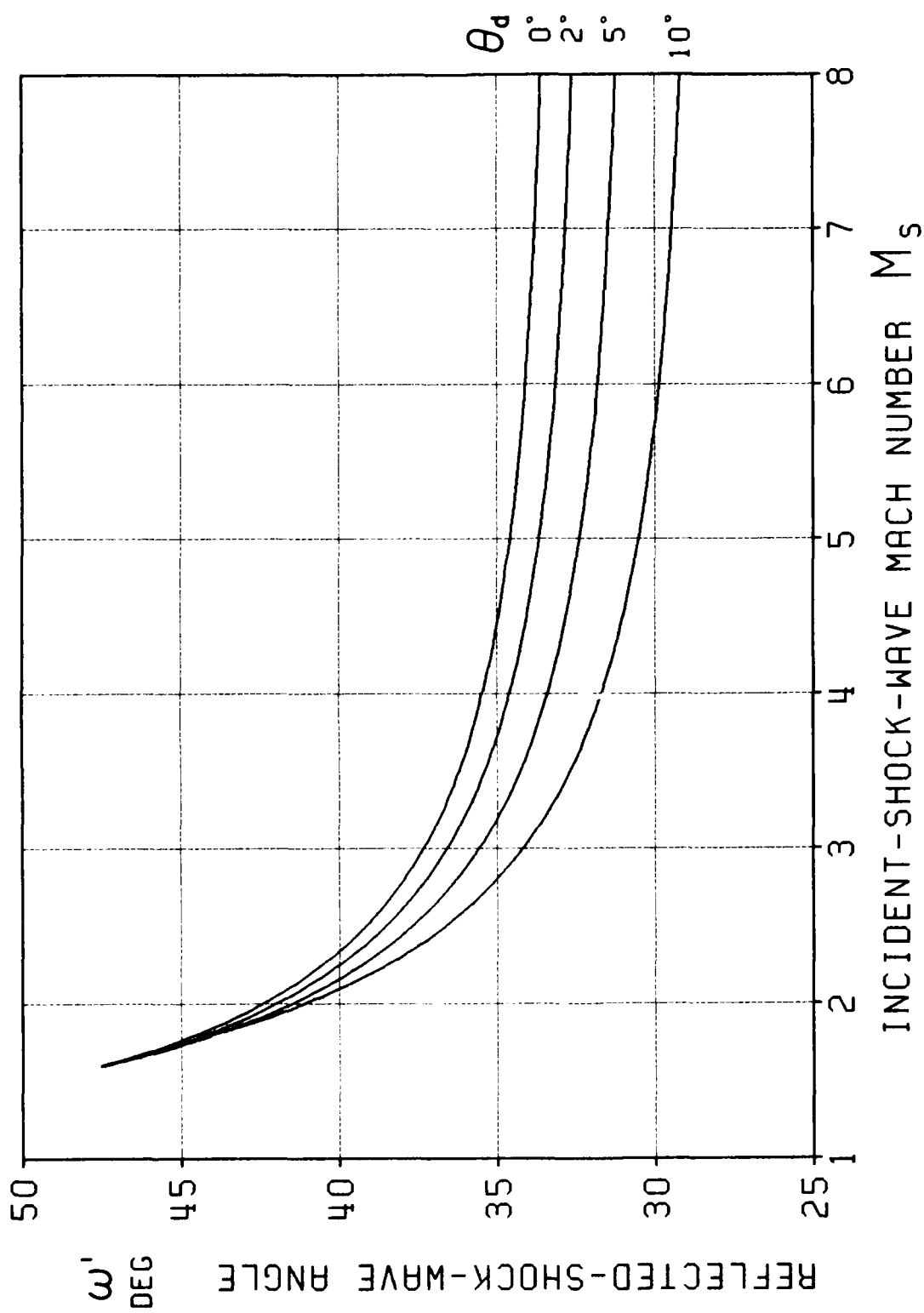
Figure 28: Effect of displacement wedge angle θ_d on reflected wave angle ω' at RR↔MR transition boundary
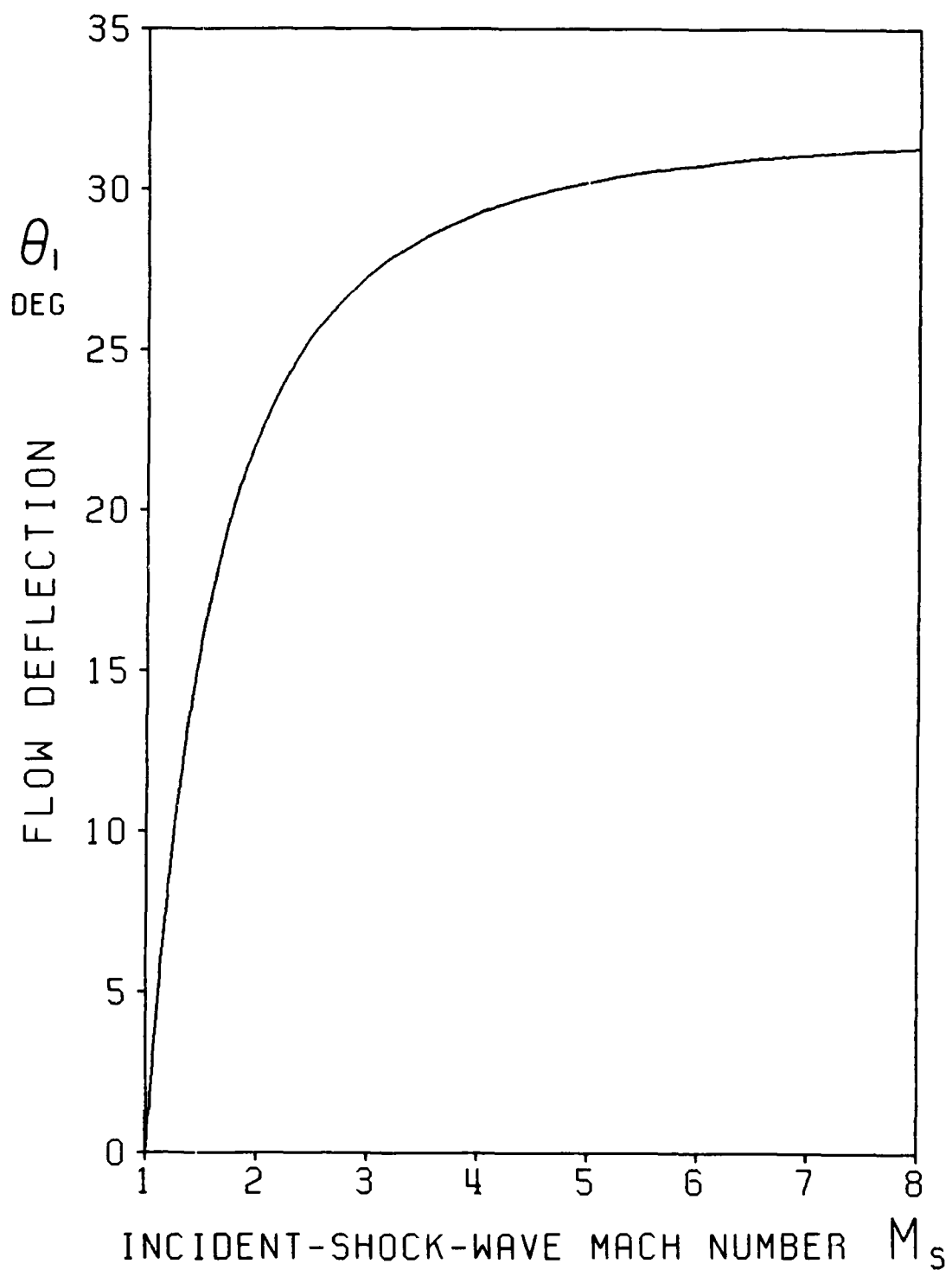
Figure 29: Inviscid solution for flow deflection θ_1 through
incident shock wave at the RR⟷MR transition boundary
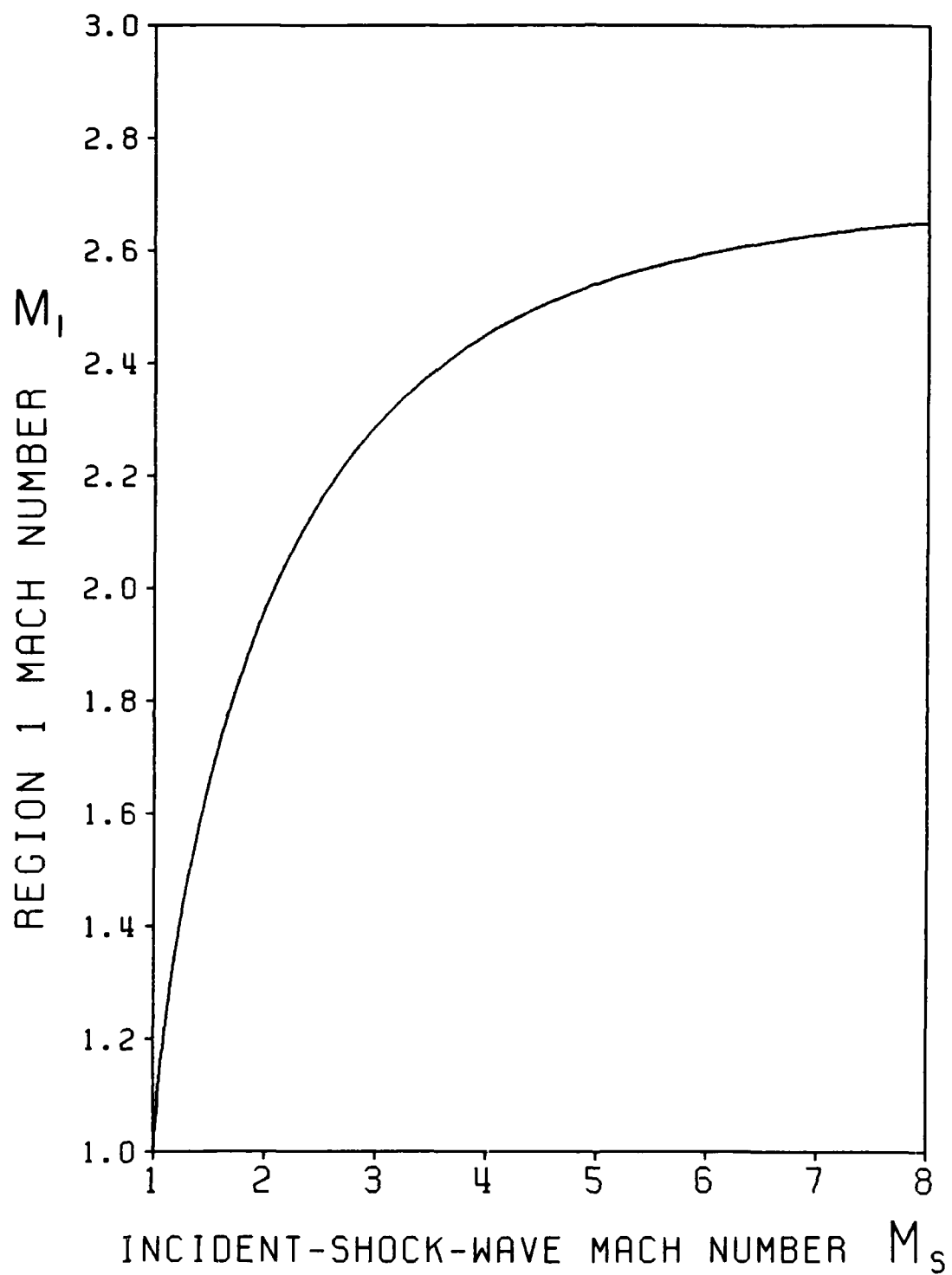
Figure 30:   Inviscid solution for flow Mach number M_1 in region 1
at RR↔MR transition boundary
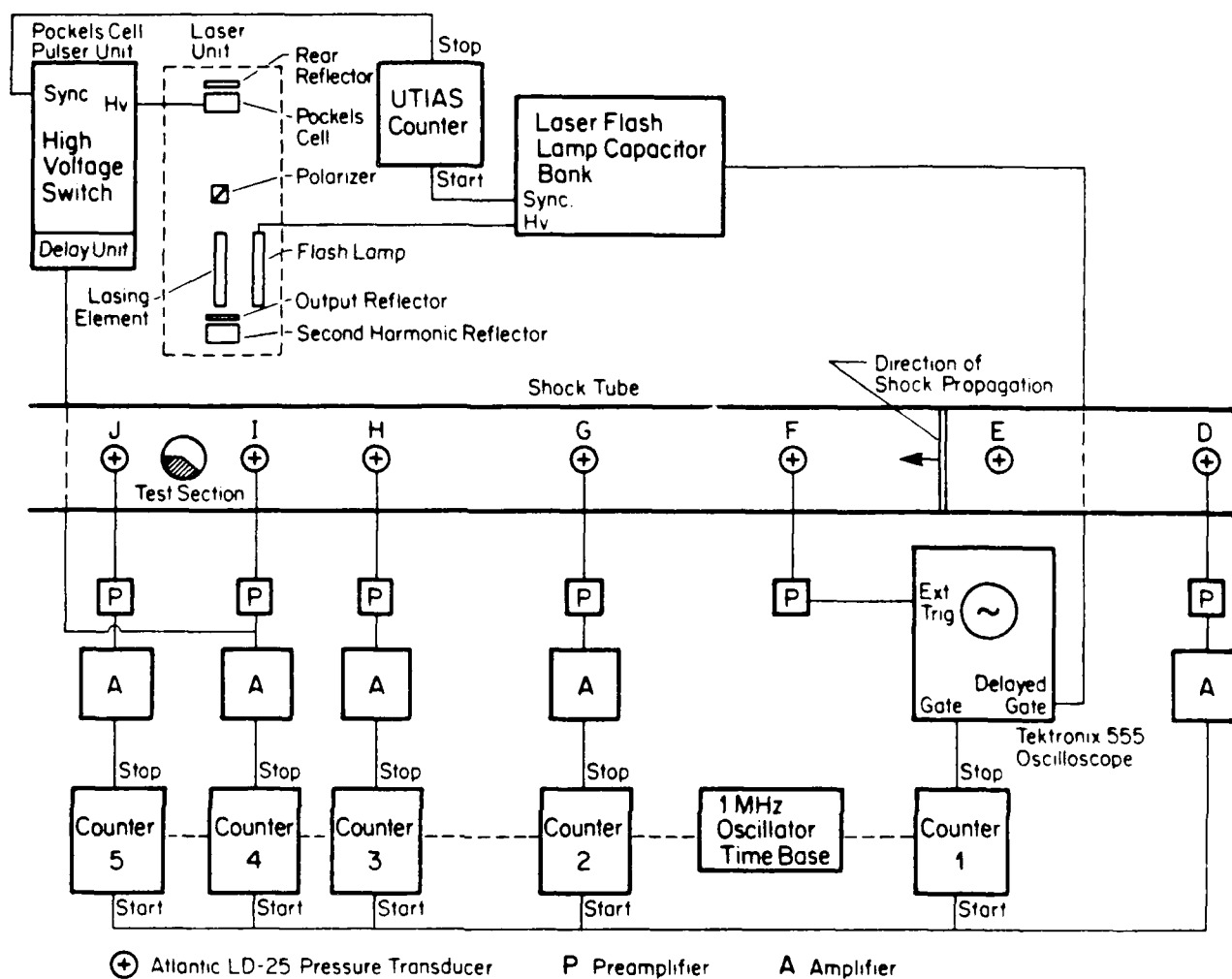
Figure 31: Schematic diagram of test equipment associated with
UTIAS 10 x 18 cm Hypervelocity Shock Tube [40]
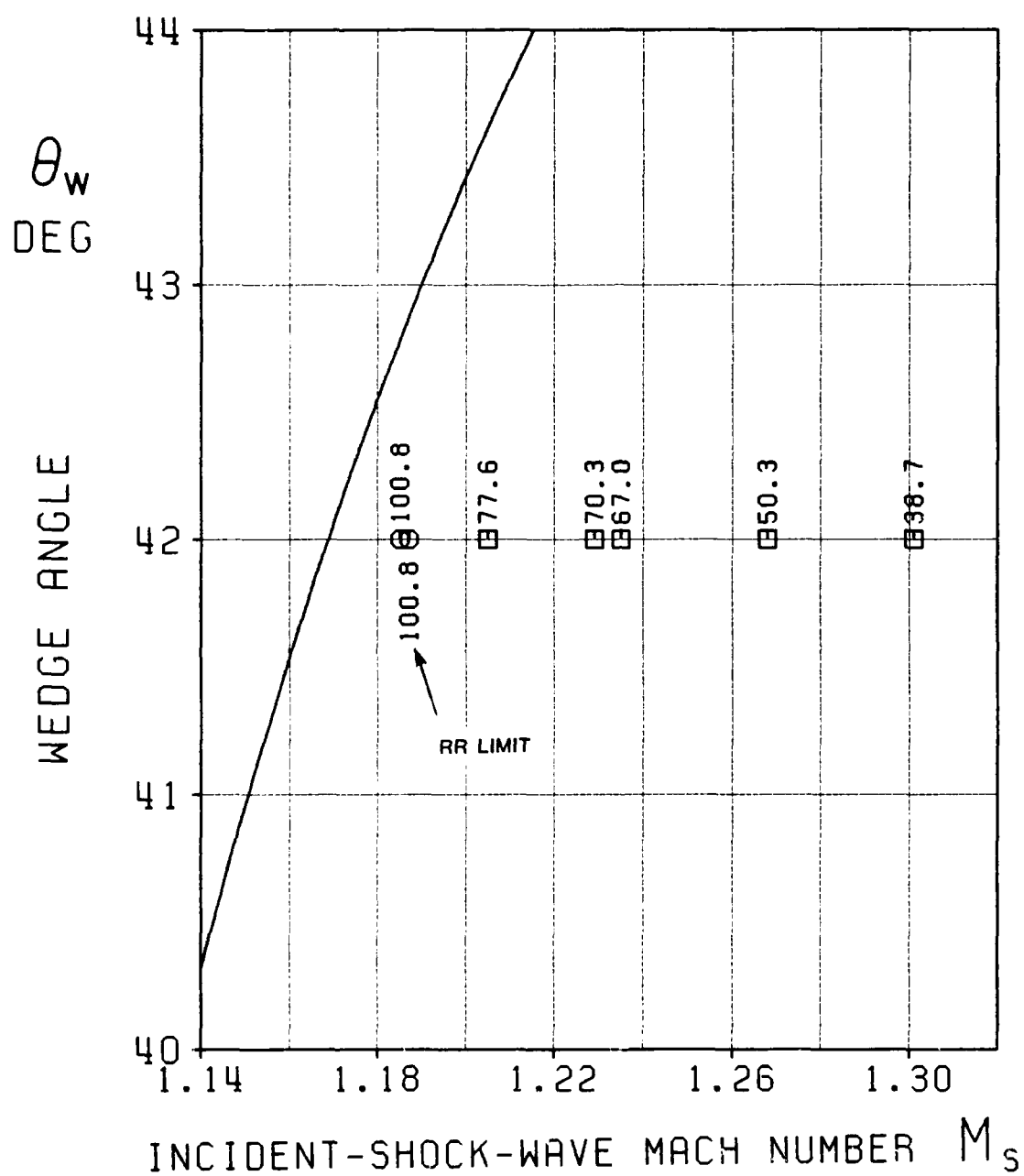
Figure 32: Experimental results for 42° wedge
for high p_0 and low M_s

Numbers beside symbols are p_0 in kPa

O   RR

□   SMR
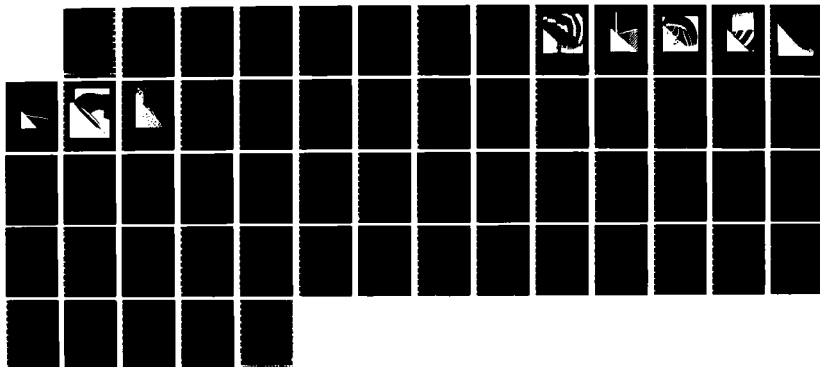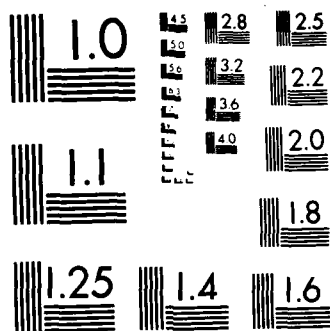
MICROCOPY RESOLUTION TEST CHART

NATIONAL BUREAU OF STANDARDS-1963-A
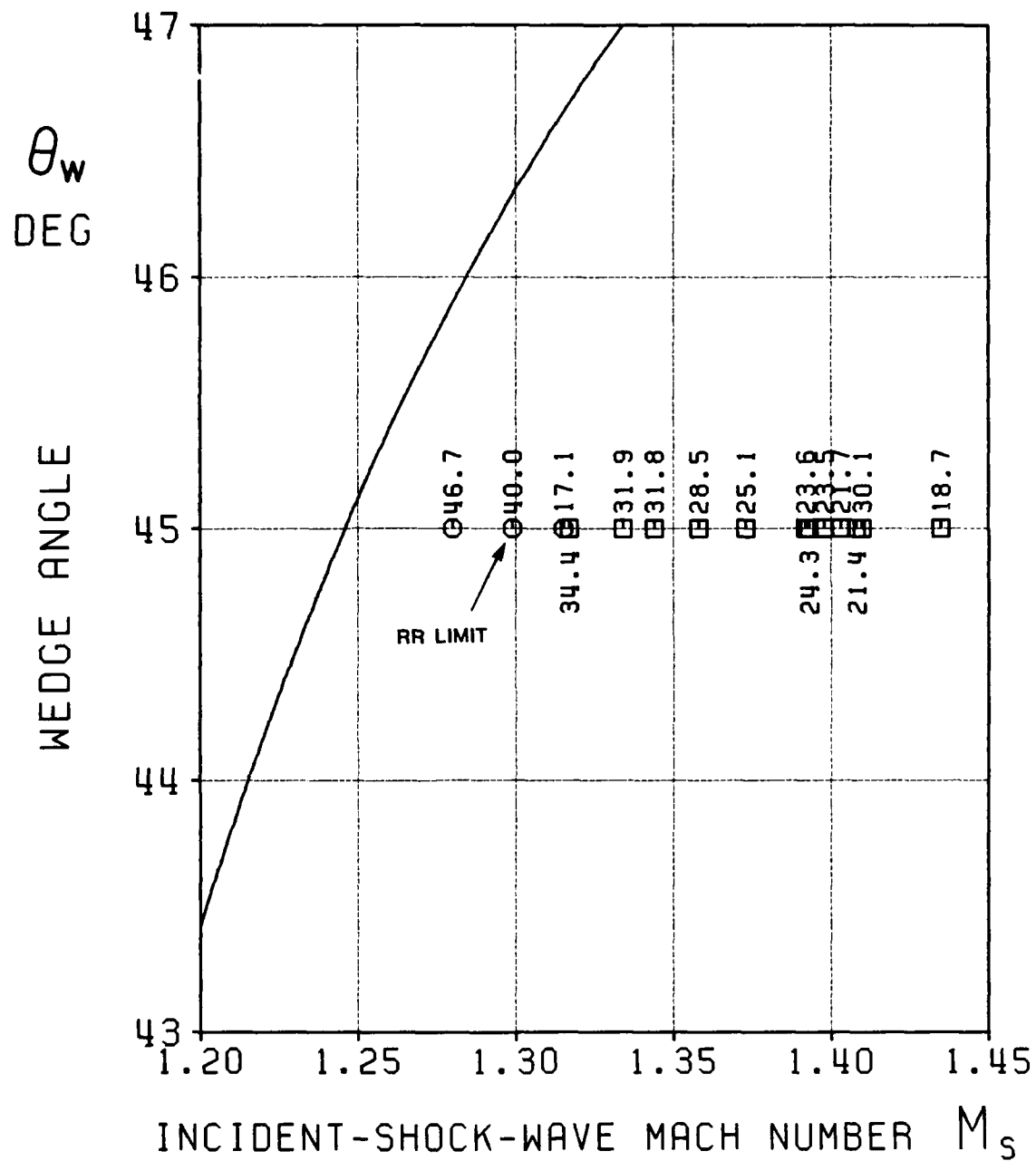
Figure 33: Experimental results for 45° wedge for high p_0 and low M_s

Numbers beside symbols are p_0 in kPa

O   RR

□   SMR
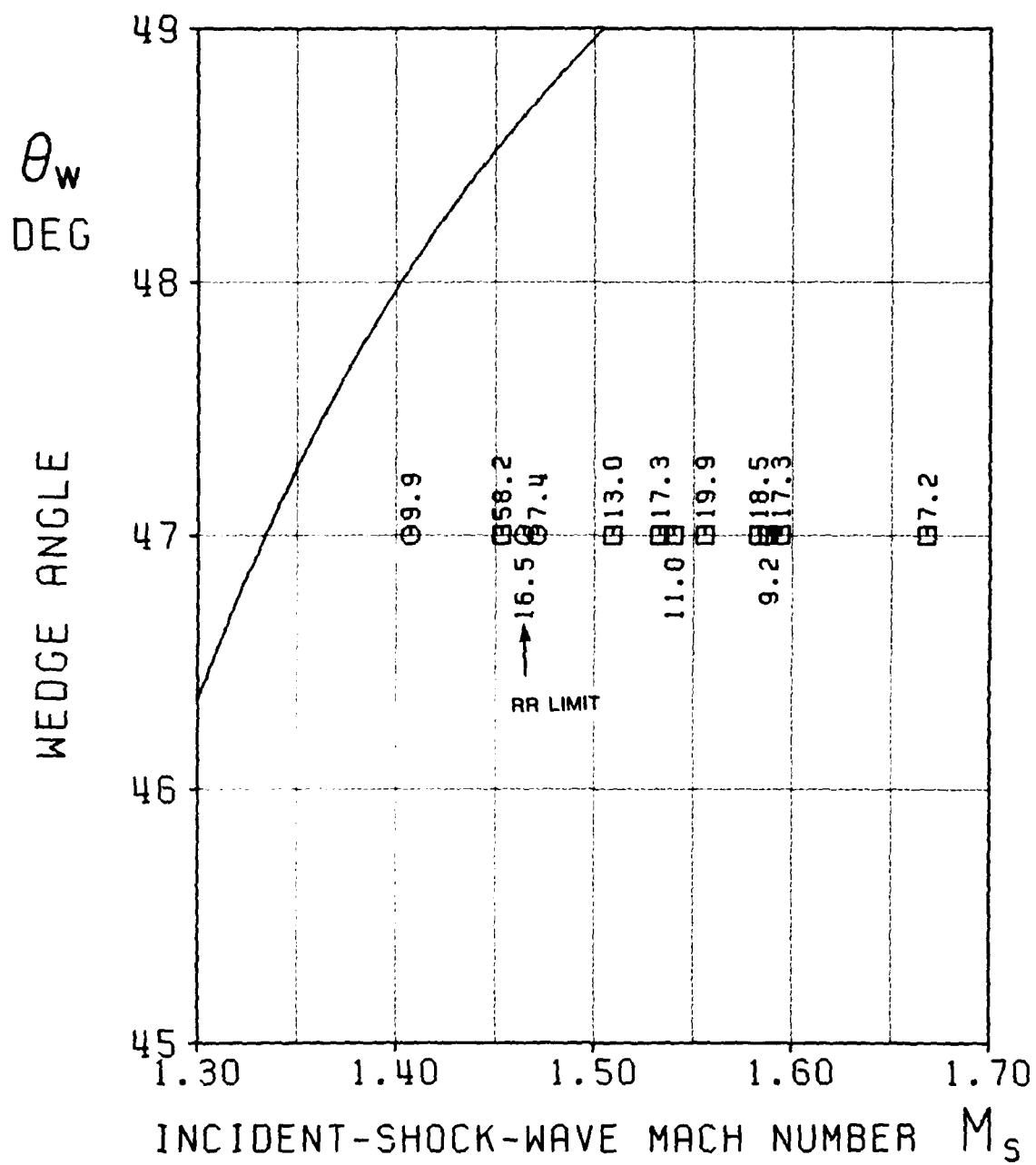
Figure 34: Experimental results for 47 wedge
for low p_0 and M_s

Numbers beside symbols are p_0 in kPa

O   RR

□   SMR
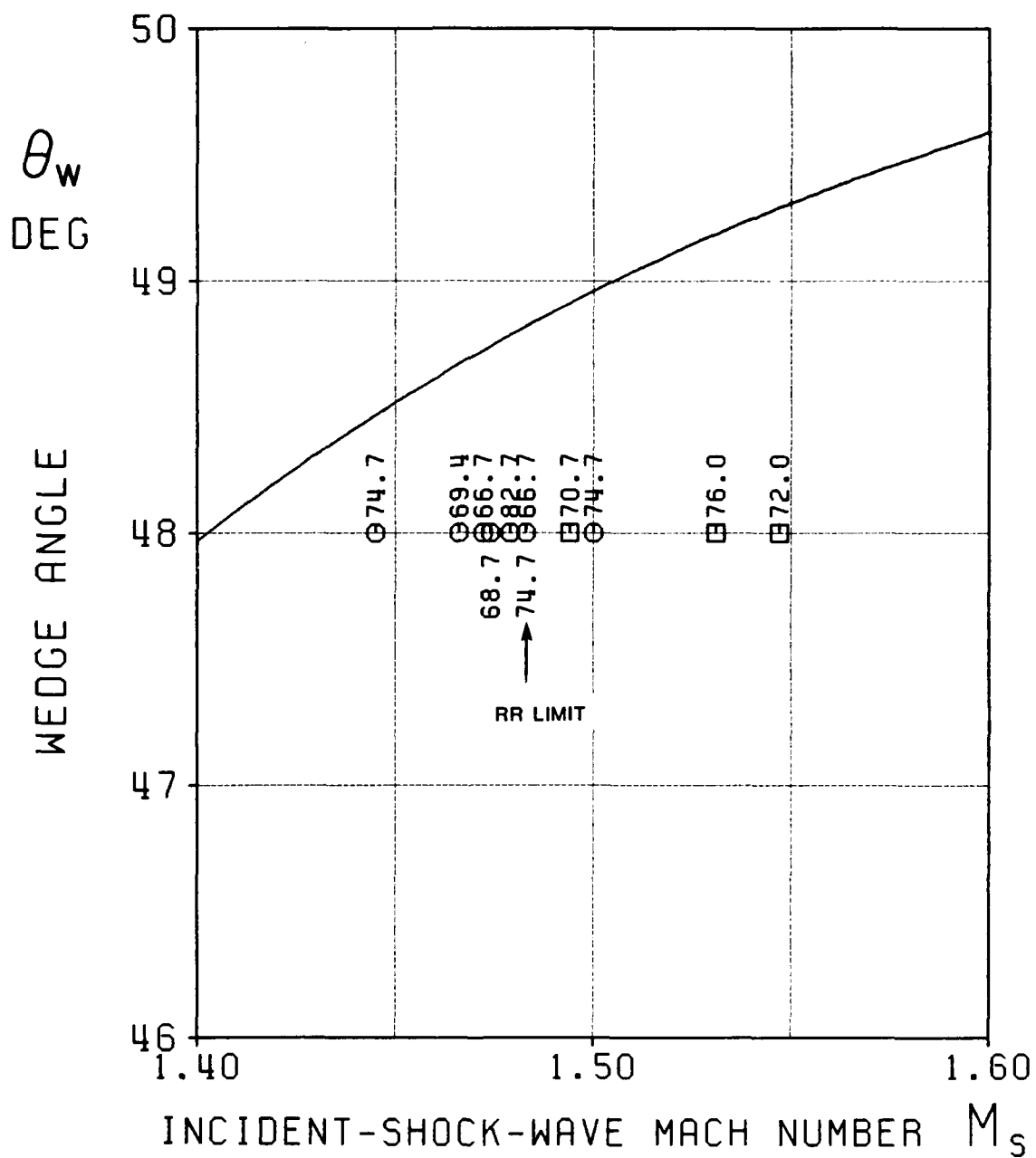
Figure 35a: Experimental results for 48° wedge for high p_0 and low M_s

Numbers beside symbols are p_0 in kPa

O RR

□ SMR
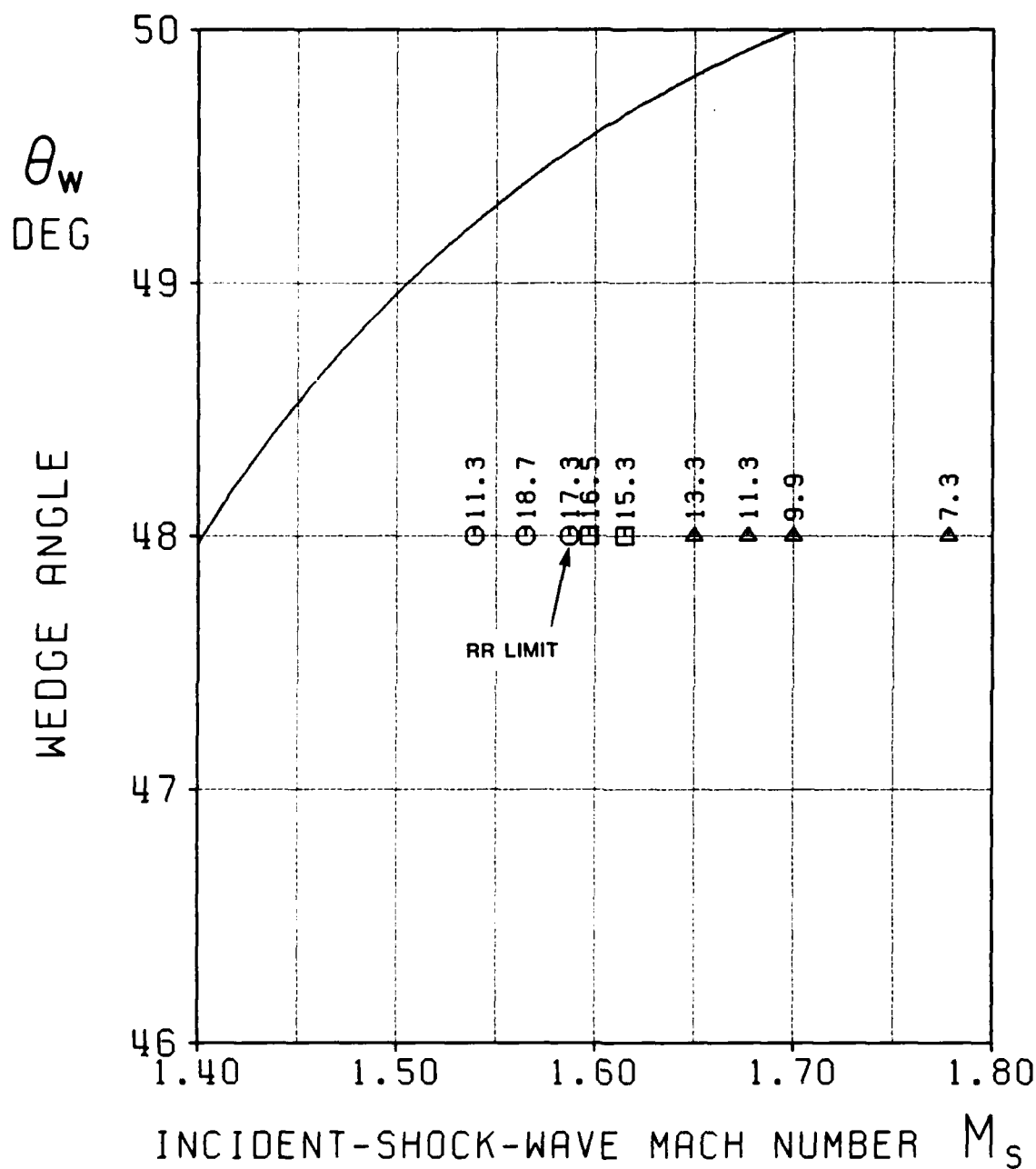
Figure 35b: Experimental results for 48° wedge
for low p_0 and M_s

Numbers beside symbols are p_0 in kPa

O   RR

□   SMR

△   CMR
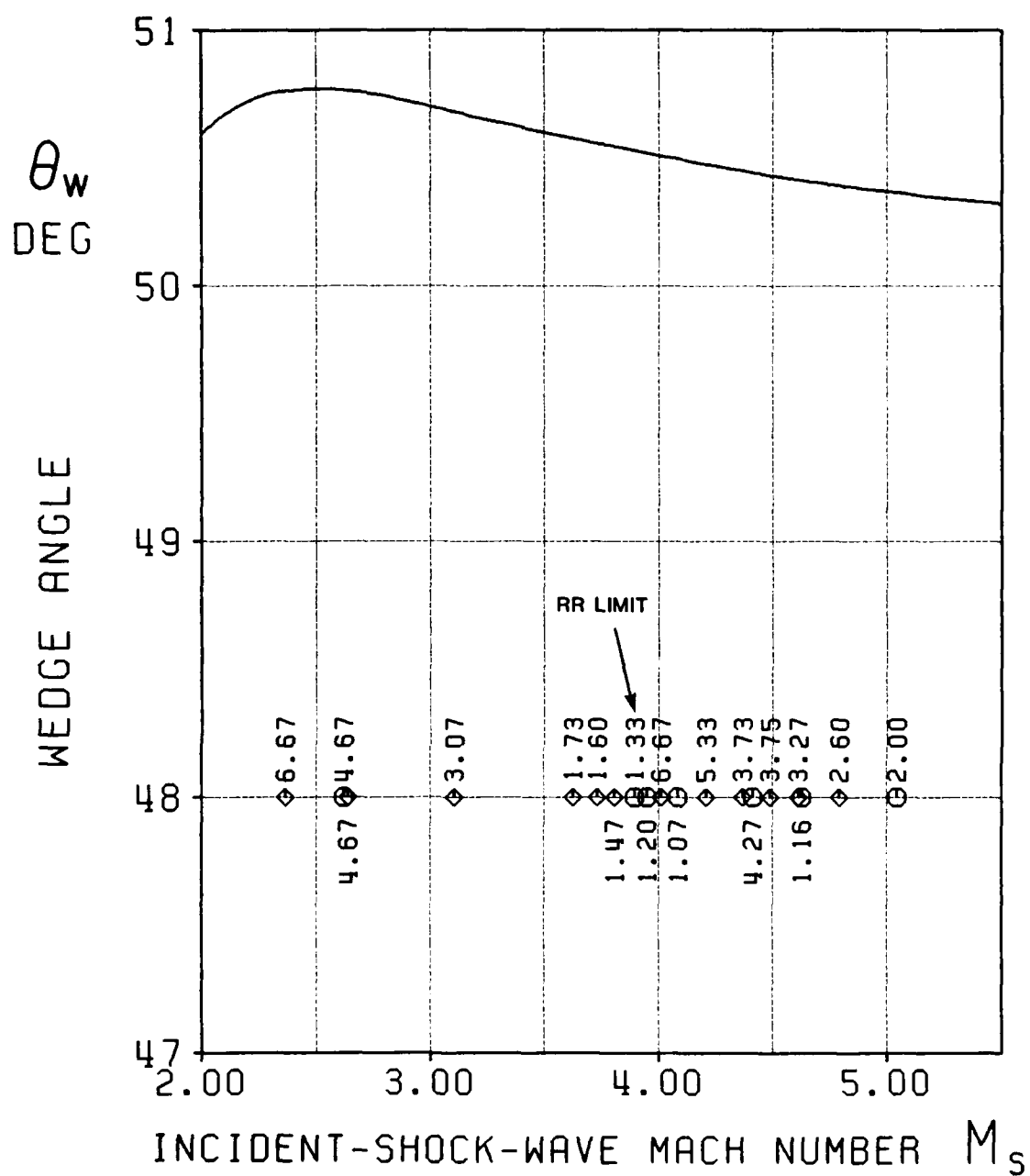
Figure 36: Experimental results for 48 wedge for low p_0 and high M_s

Numbers beside symbols are p_0 in kPa

O   RR

◇   DMR
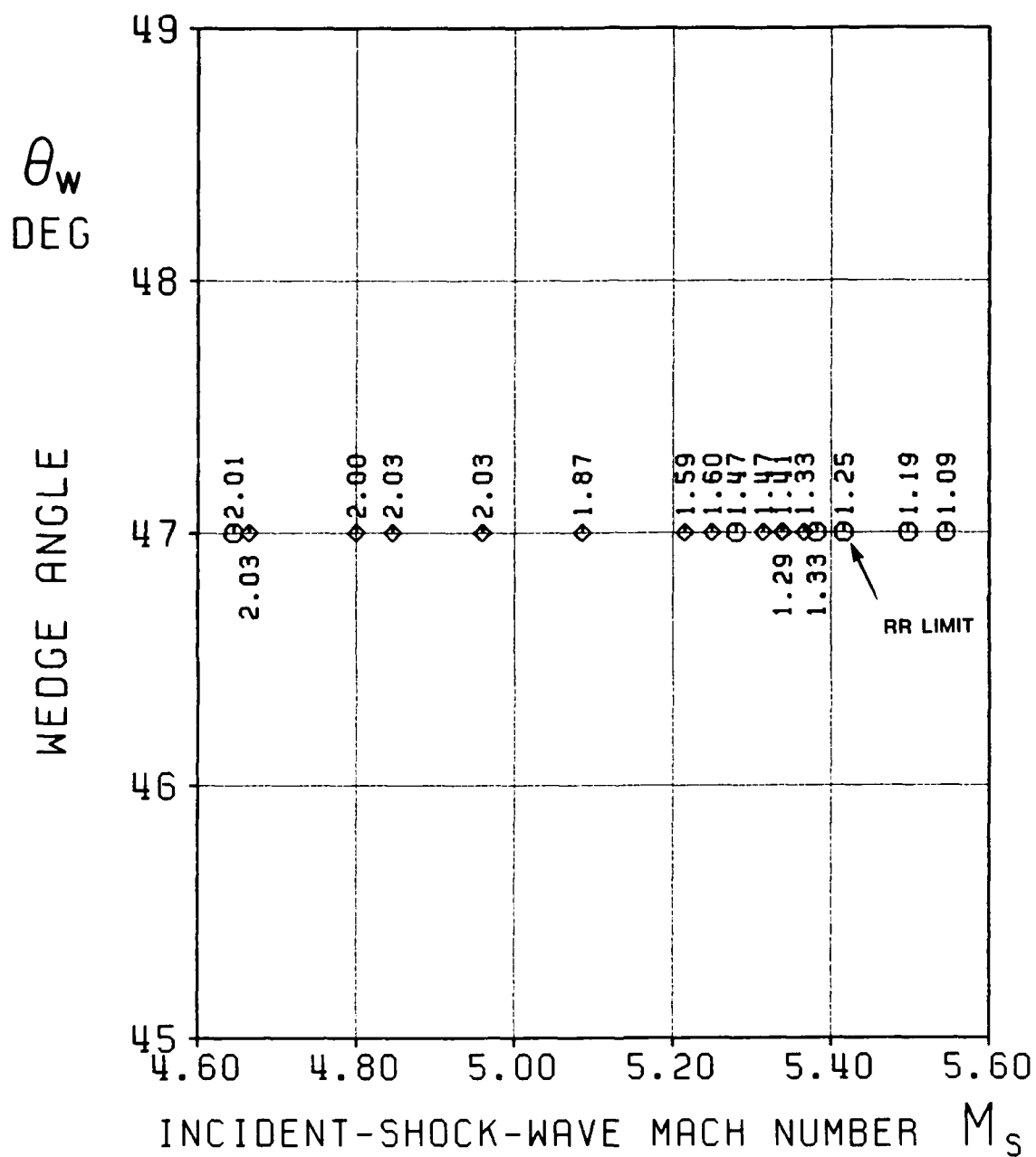
Figure 37: Experimental results for 47 wedge
for low p_0 and high M_s

Numbers beside symbols are p_0 in kPa

O   RR

◇   DMR
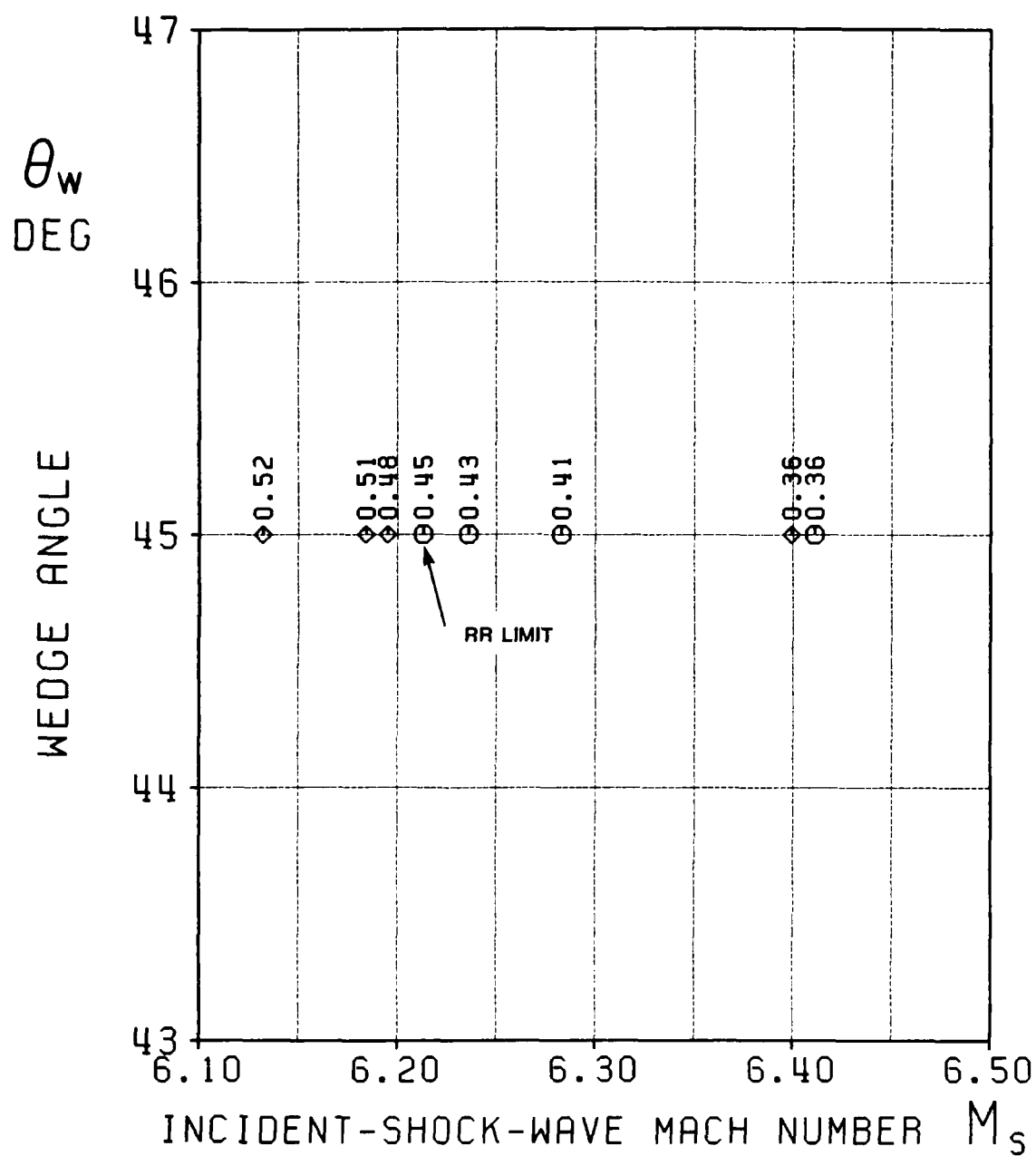
Figure 38: Experimental results for 45 wedge
for low p_0 and high M_s
Numbers beside symbols are p_0 in kPa
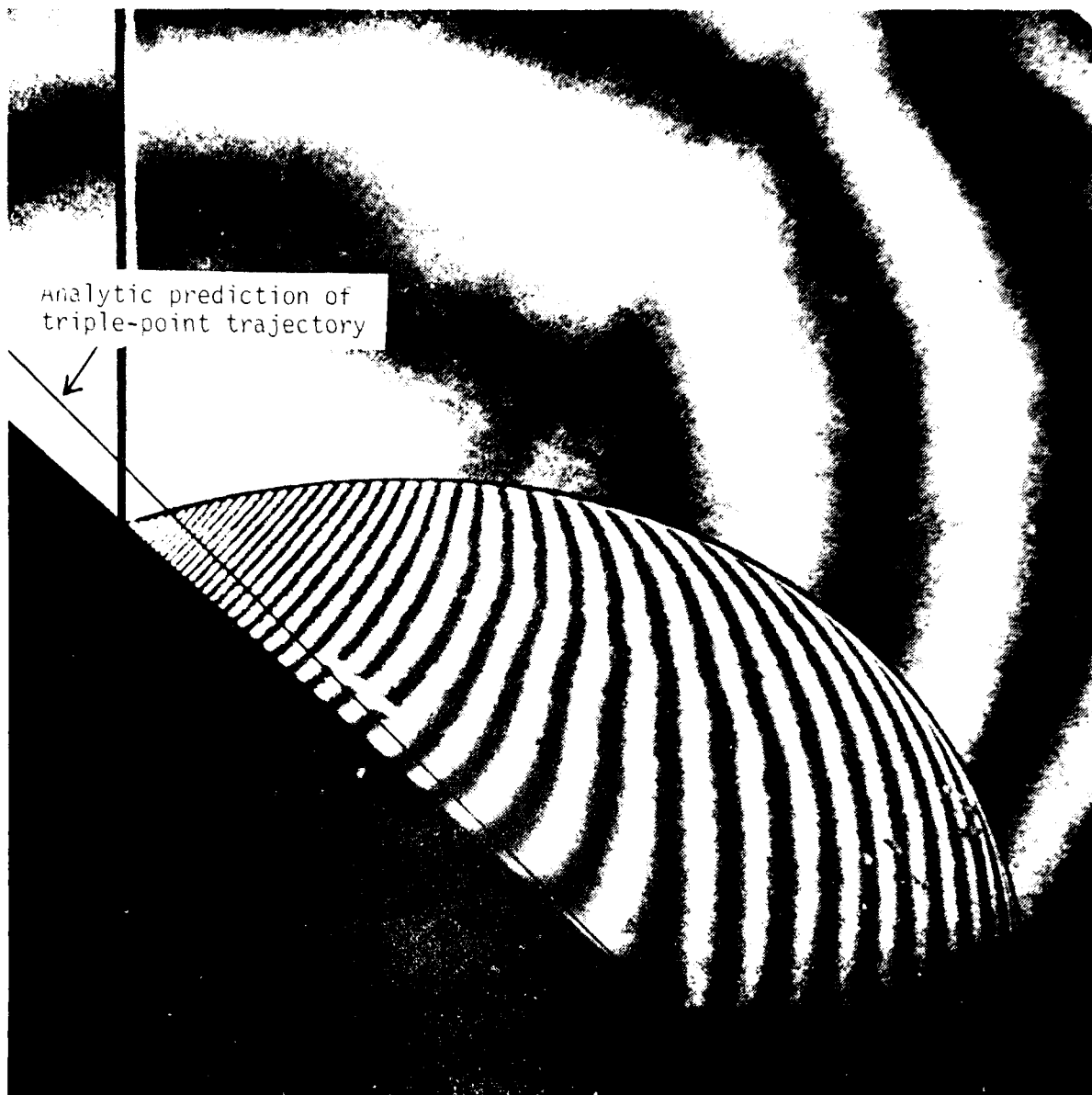
O   RR

◇   DMR

Figure 59a: ... .ular reflection ...)
... ., ... 42°, ...d7 . .,
. Hz, ...
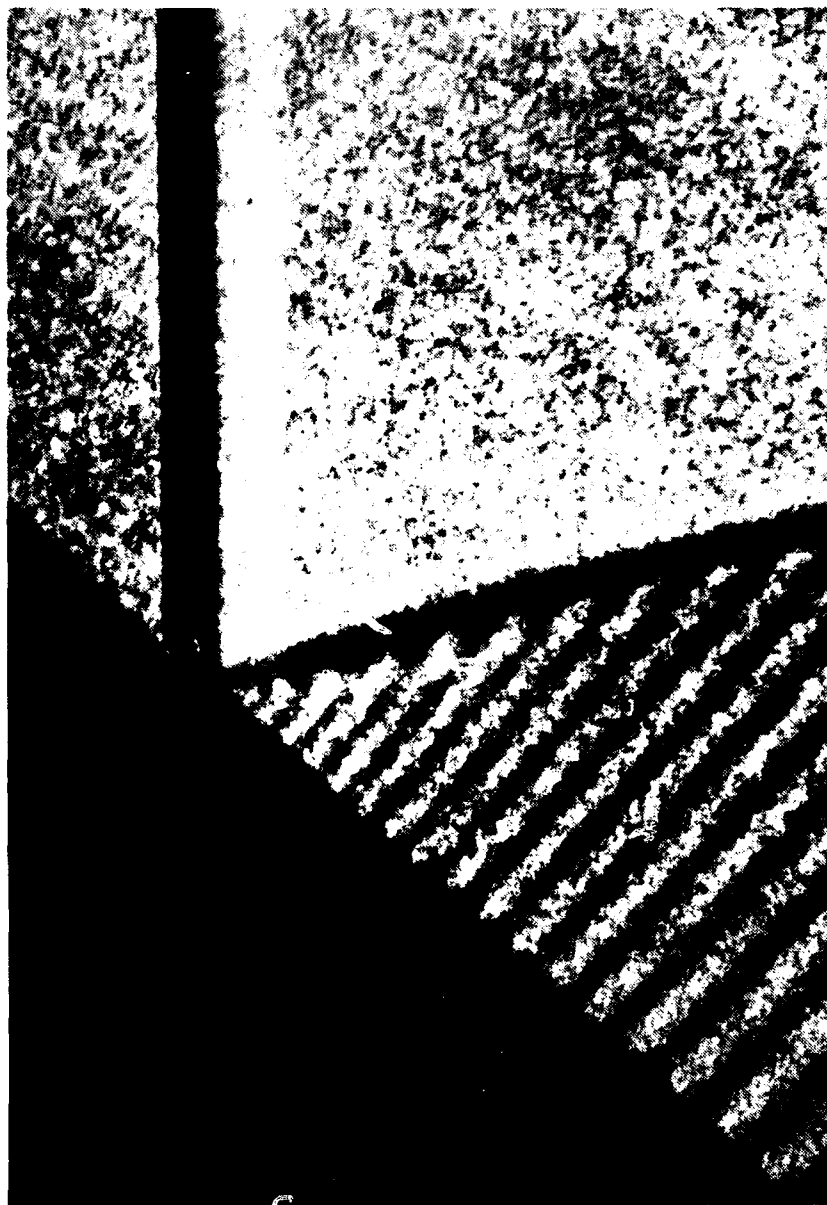
Figure 39b: Interferogram of regular reflection (RR)
Closeup of reflection point P

Exp. 36, M_s = 1.19, θ_w = 42°, λ = 3472 A,
p_0 = 100.8 kPa, T_0 = 25.5 °C

Analytic prediction of
triple-point trajectory
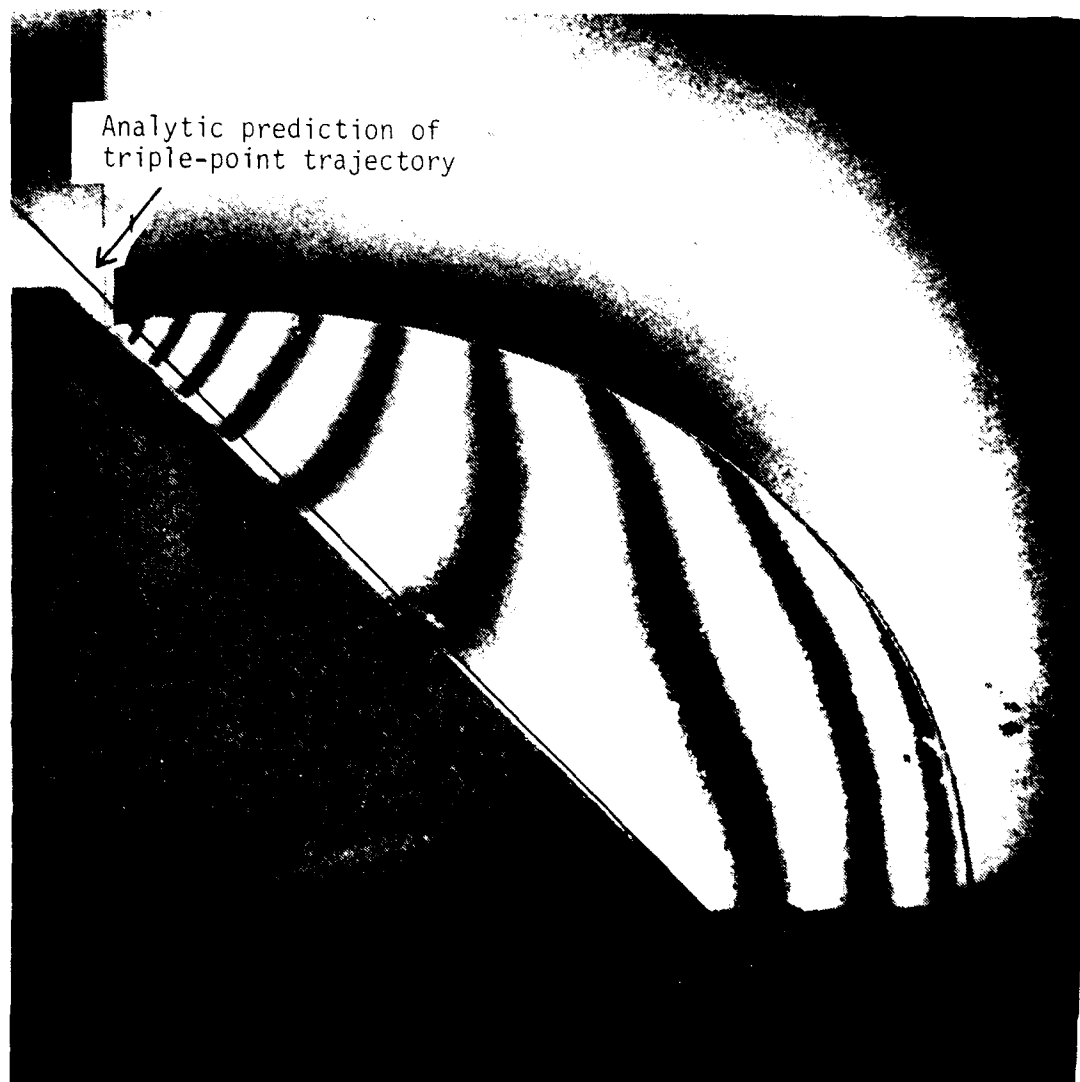
Figure 40a: Interferogram of single-Mach reflection (SMR)
Exp. 27, M = 1.9, θ_w = 3°, λ = 6943 Å,
air, T_0 = 26.6 C

Figure 40b: Interferogram of single-Mach reflection (SMR)
Closeup of triple point T

Exp. 27, M_s = 1.40, θ_w = 45°, λ = 6943 A,

p_0 = 23.5 kPa, T_0 = 22.6 C

Analytic prediction of
triple-point trajectory
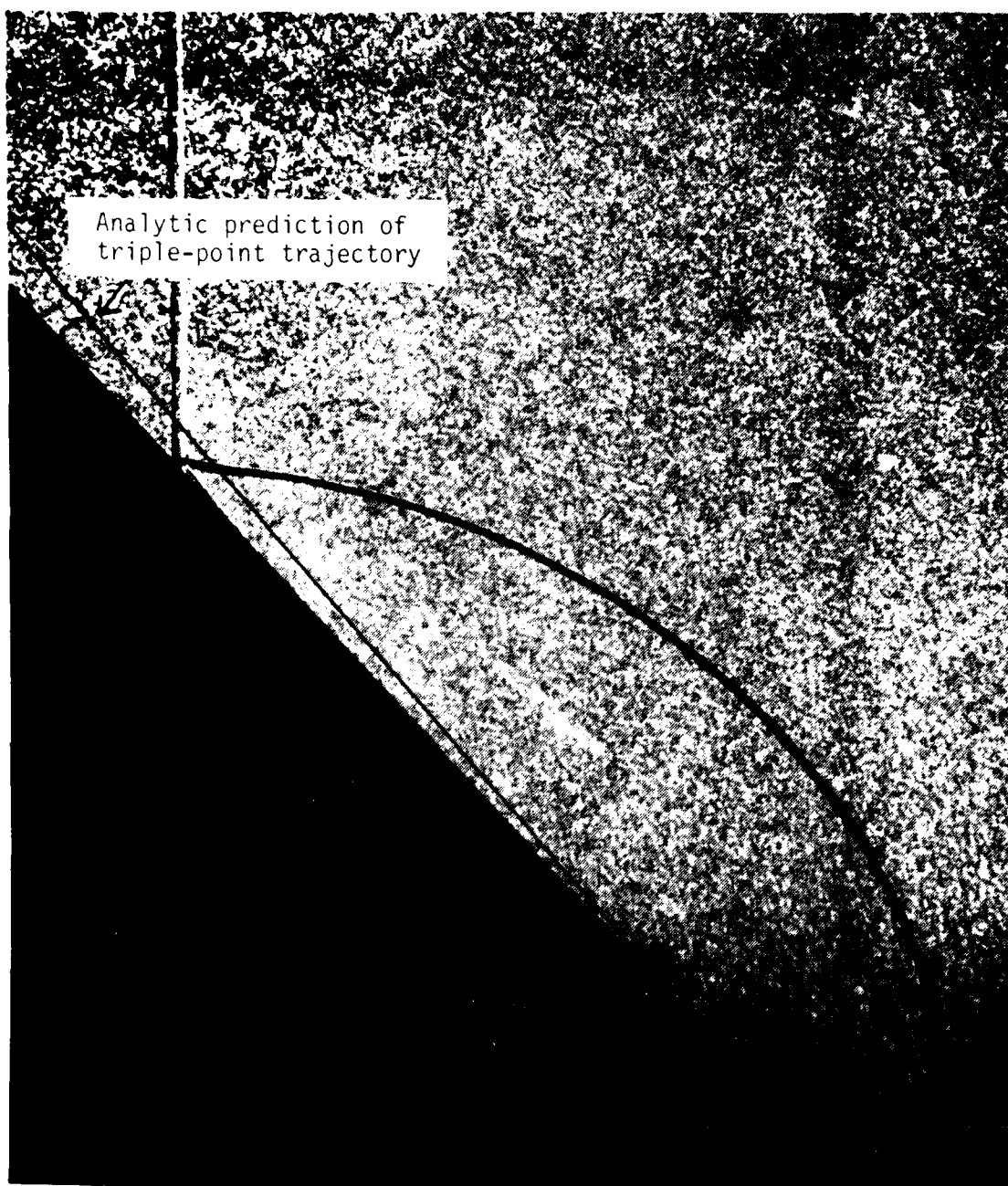
Figure 41a: Shadowgraph of complex-Mach reflection (CMR)
Exp. 81, M_S = 1.78, θ_w = 48°,
p_0 = 7.33 kPa, T_0 = 23.3°C

Figure 41b: Shadowgraph of complex-Mach reflection (CMR)
Closeup of triple point T

Exp. 81, $M_s = 1.78$, $\theta_w = 48°$,
$p_0 = 7.33$ kPa, $T_0 = 23.3°$C

Analytic prediction of
triple-point trajectory
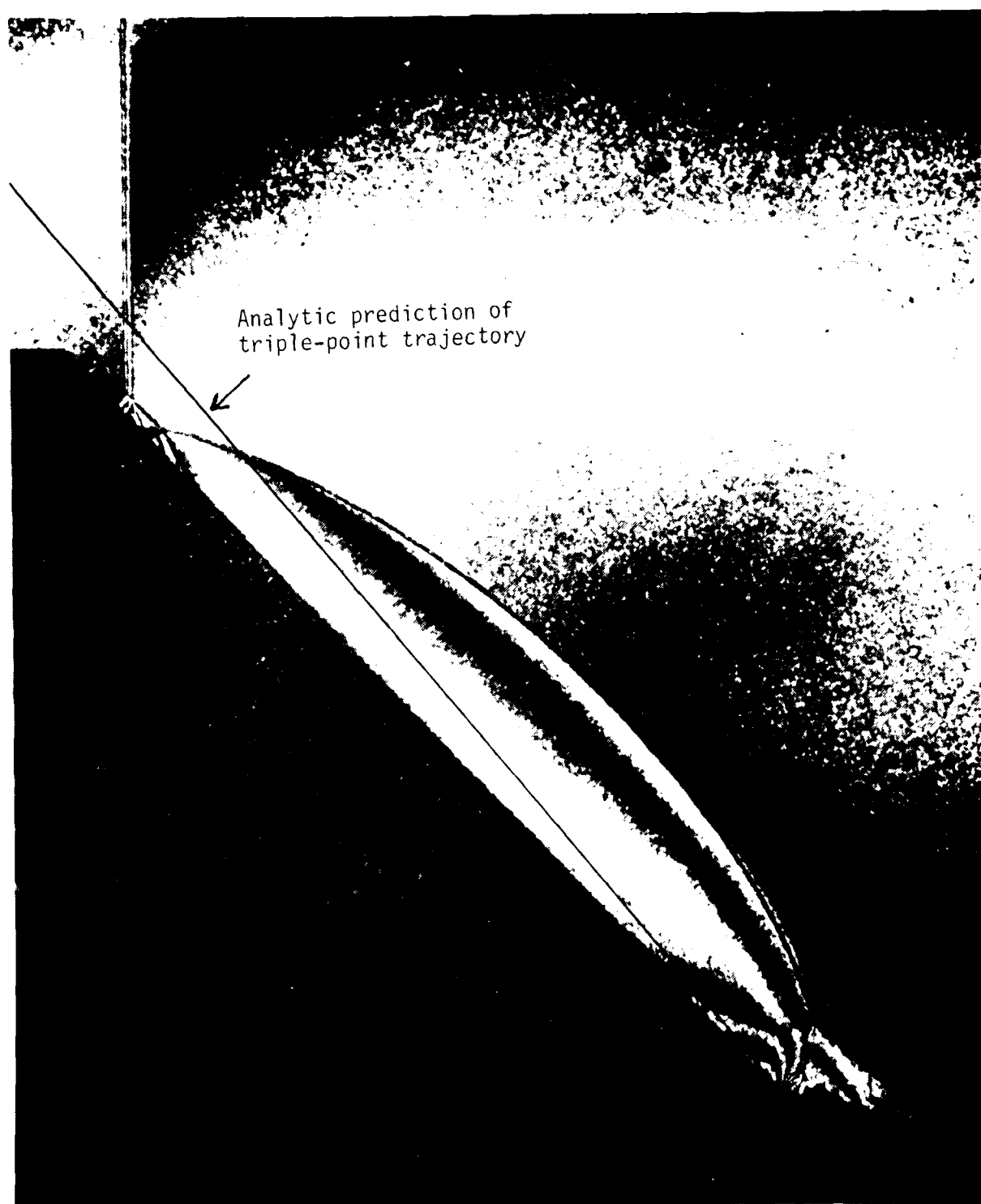
Figure 42a: Interferogram of double-Mach reflection (DMR)

Exp. 49, $M_s = 5.31$, $\theta_w = 47°$, $\lambda = 6943$ Å,

$p_0 = 1.47$ kPa, $T_0 = 27.0°$C

Figure 42b: Interferogram of double-Mach reflection (DMR)
Closeup of triple point T

Exp. 49, M_s = 5.31, θ_w = 47°, λ = 6943 Å,
p_0 = 1.47 kPa, T_0 = 27.0°C
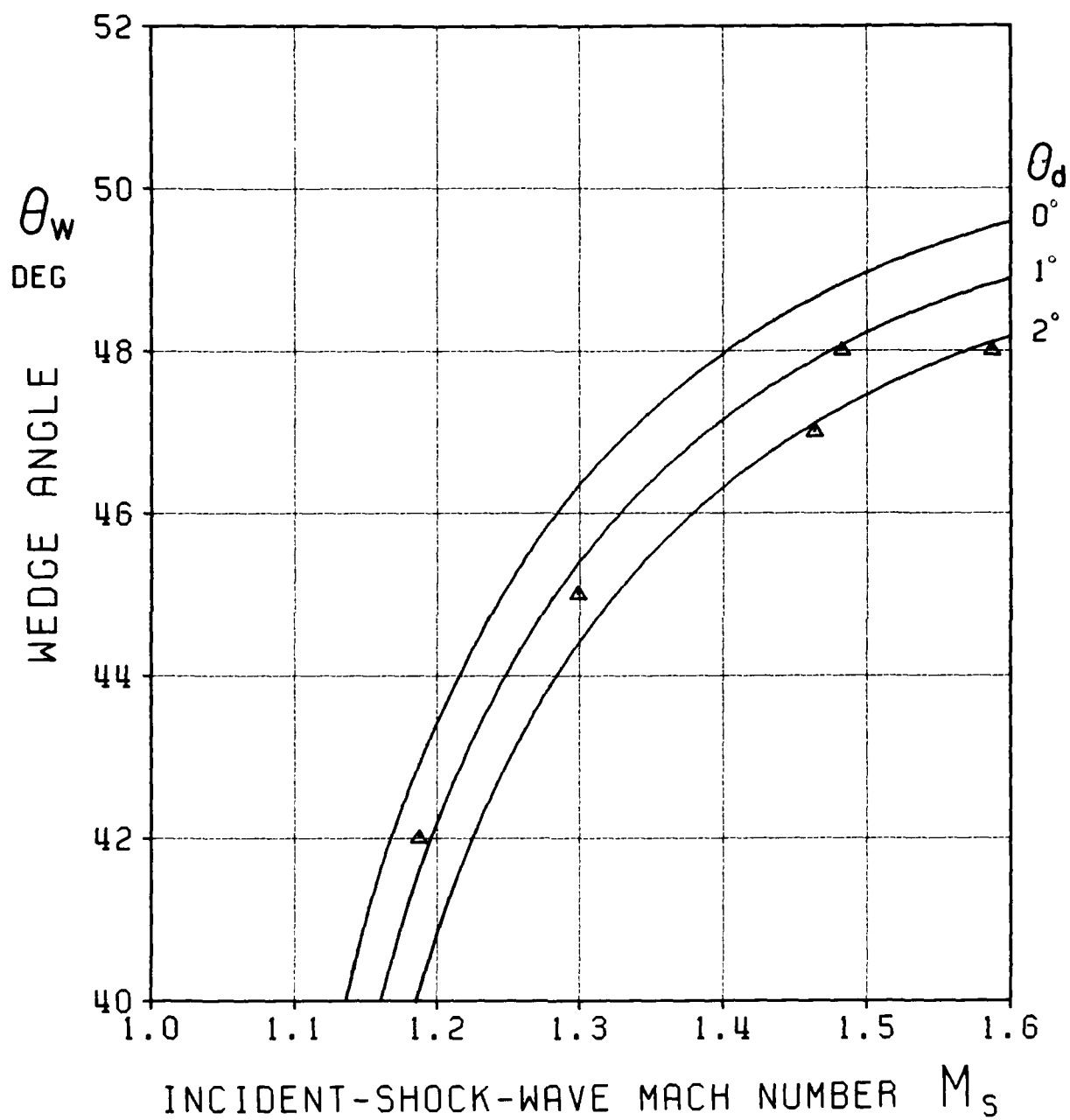
Figure 43: Comparison of experimentally determined transition boundary points with inviscid RR⟷MR boundary
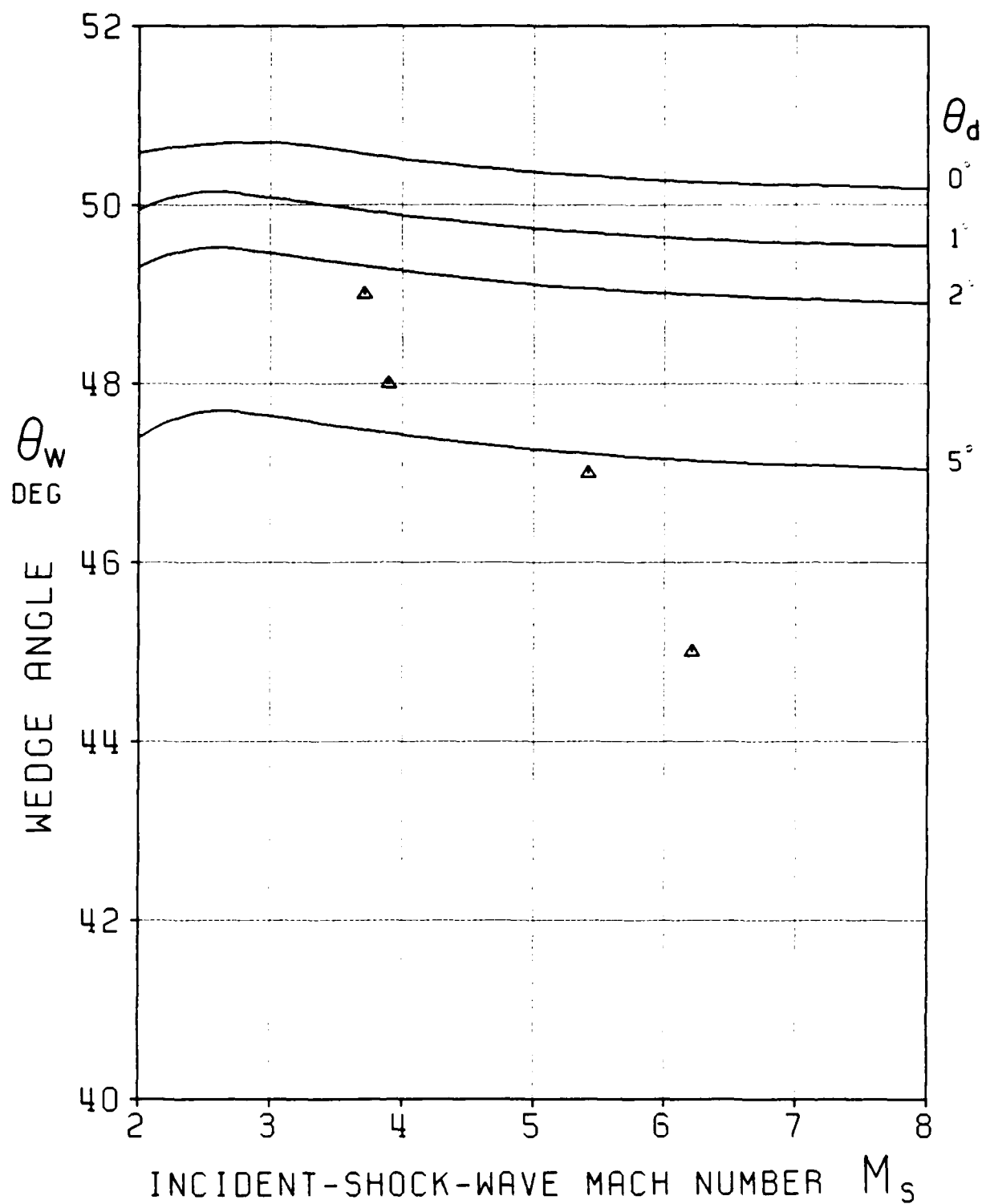
Figure 44: Comparison of experimentally determined transition boundary points with inviscid RR◄►MR boundary
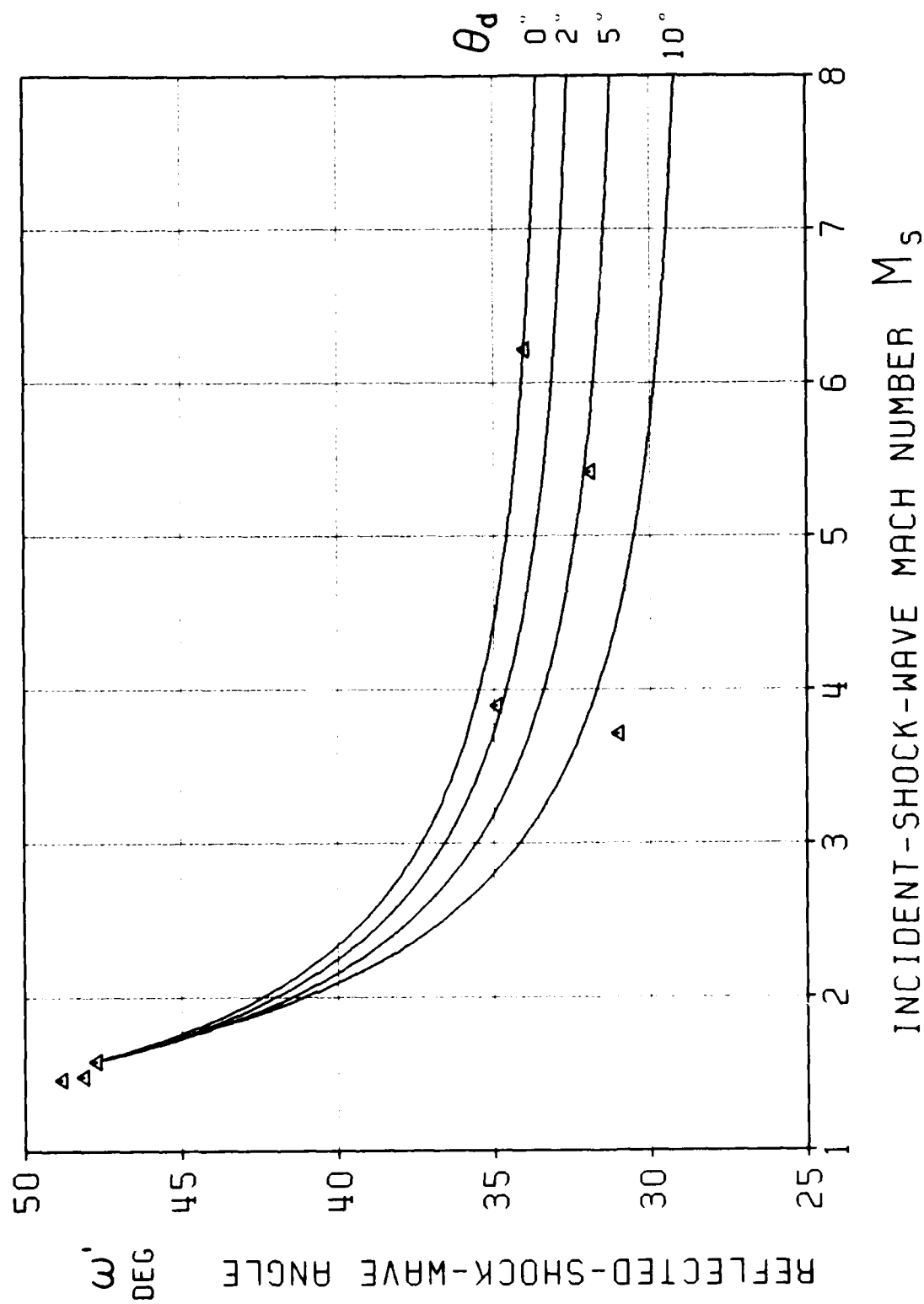
Figure 45: Measured reflected-wave angle ω' at various RR⟷MR transition points
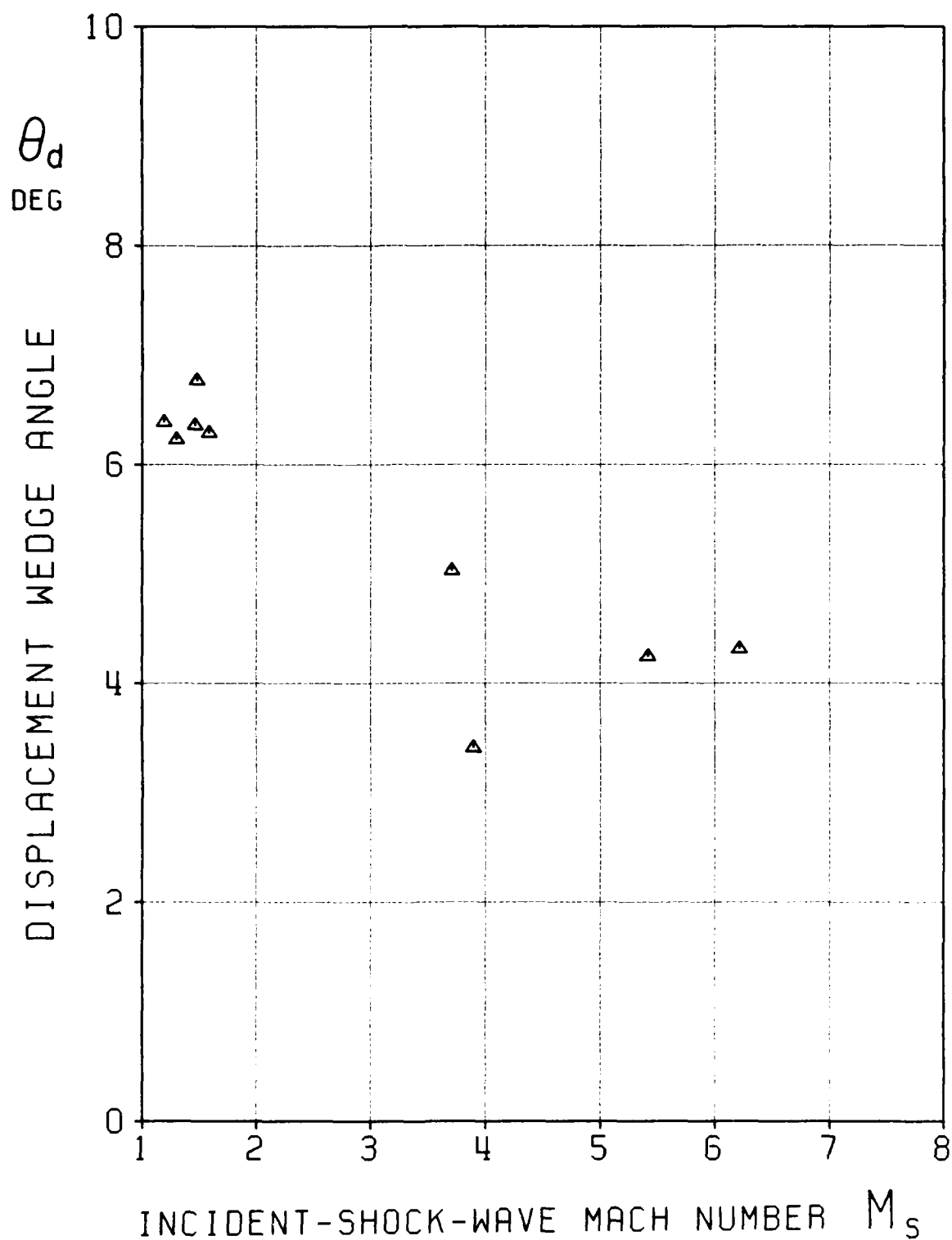
Figure 46: Displacement wedge angle θ_d at RR⟷MR transition boundary for $p_0 = 2.0$ kPa as determined by reduction of experimental results at various initial pressures
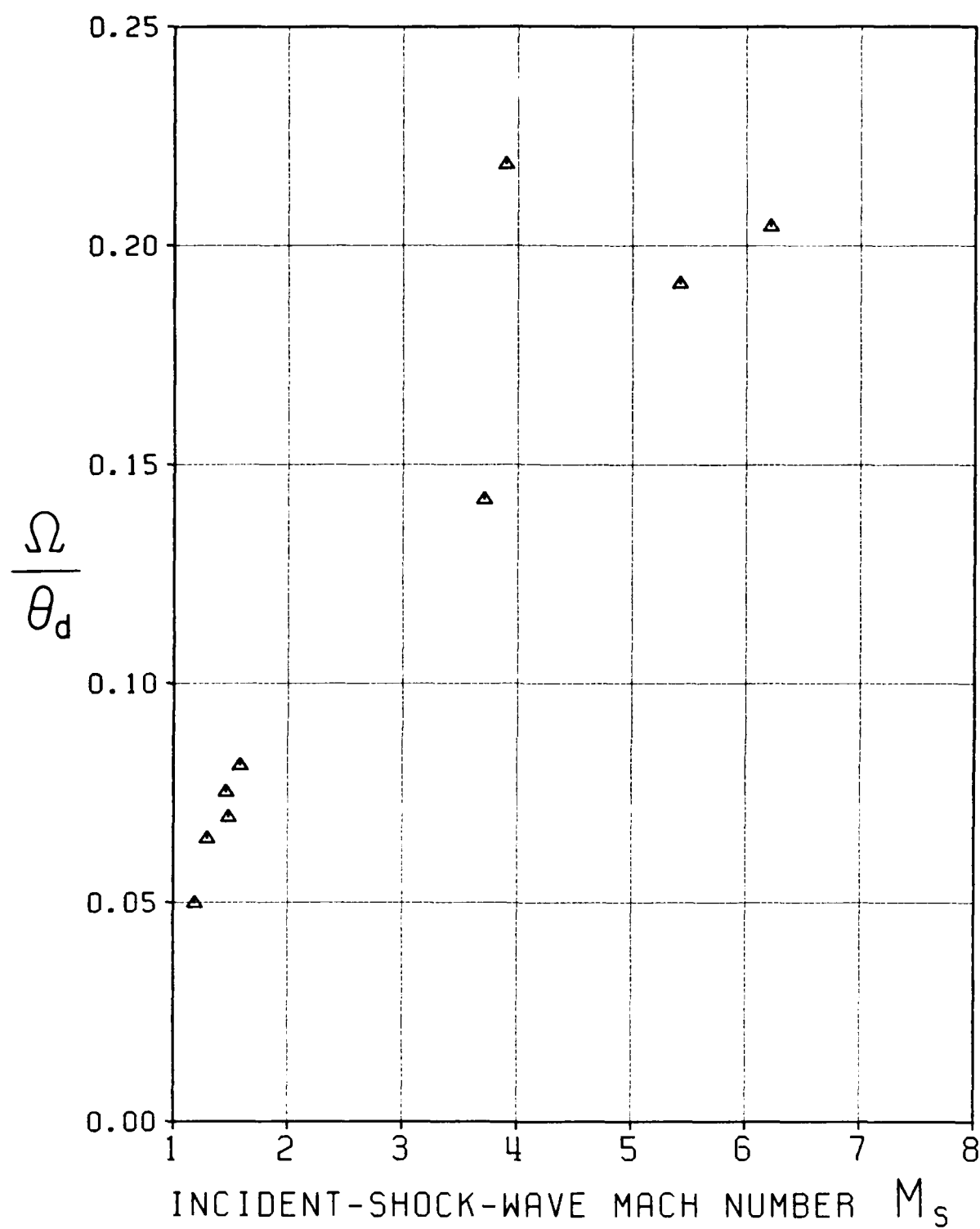
Figure 47: Ratio of boundary-layer size parameter Ω to
experimentally determined displacement wedge angle θ_d
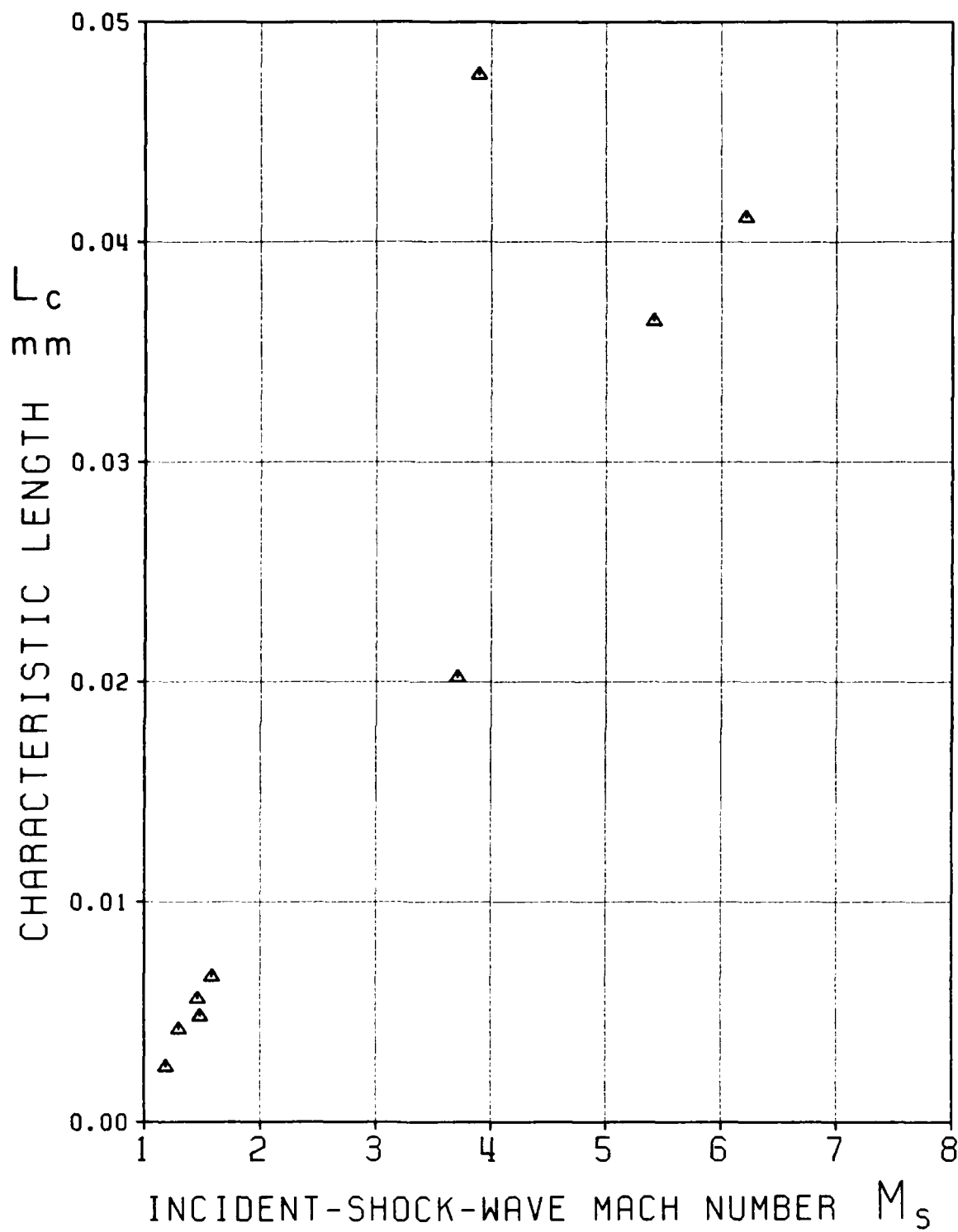
Figure 48: Characteristic length of boundary layer as determined
by comparison of predicted boundary-layer size and
experimental results
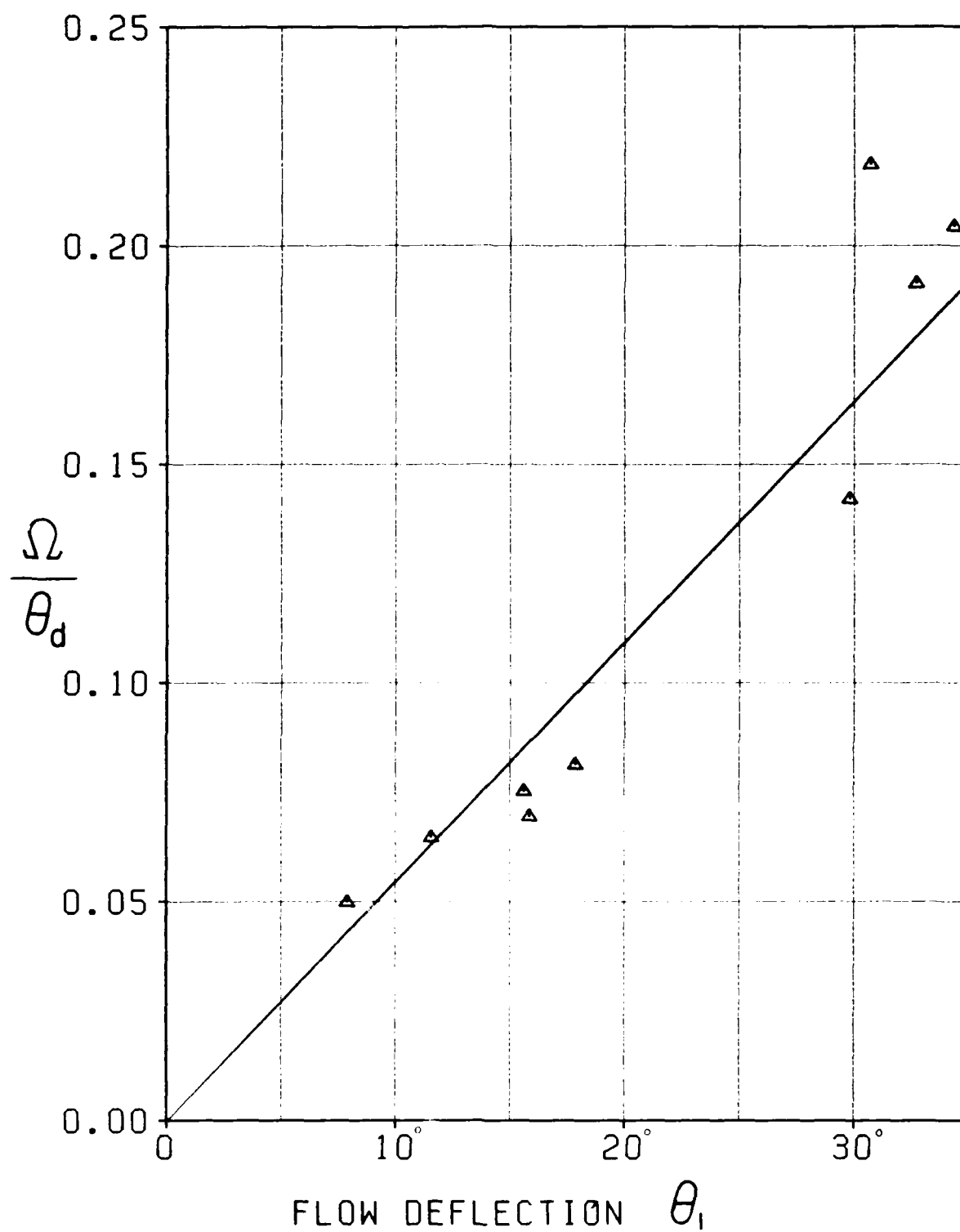
Figure 49: Ratio of boundary-layer size parameter Ω to experimentally determined displacement wedge angle θ_d vs incident shock flow deflection angle θ_1
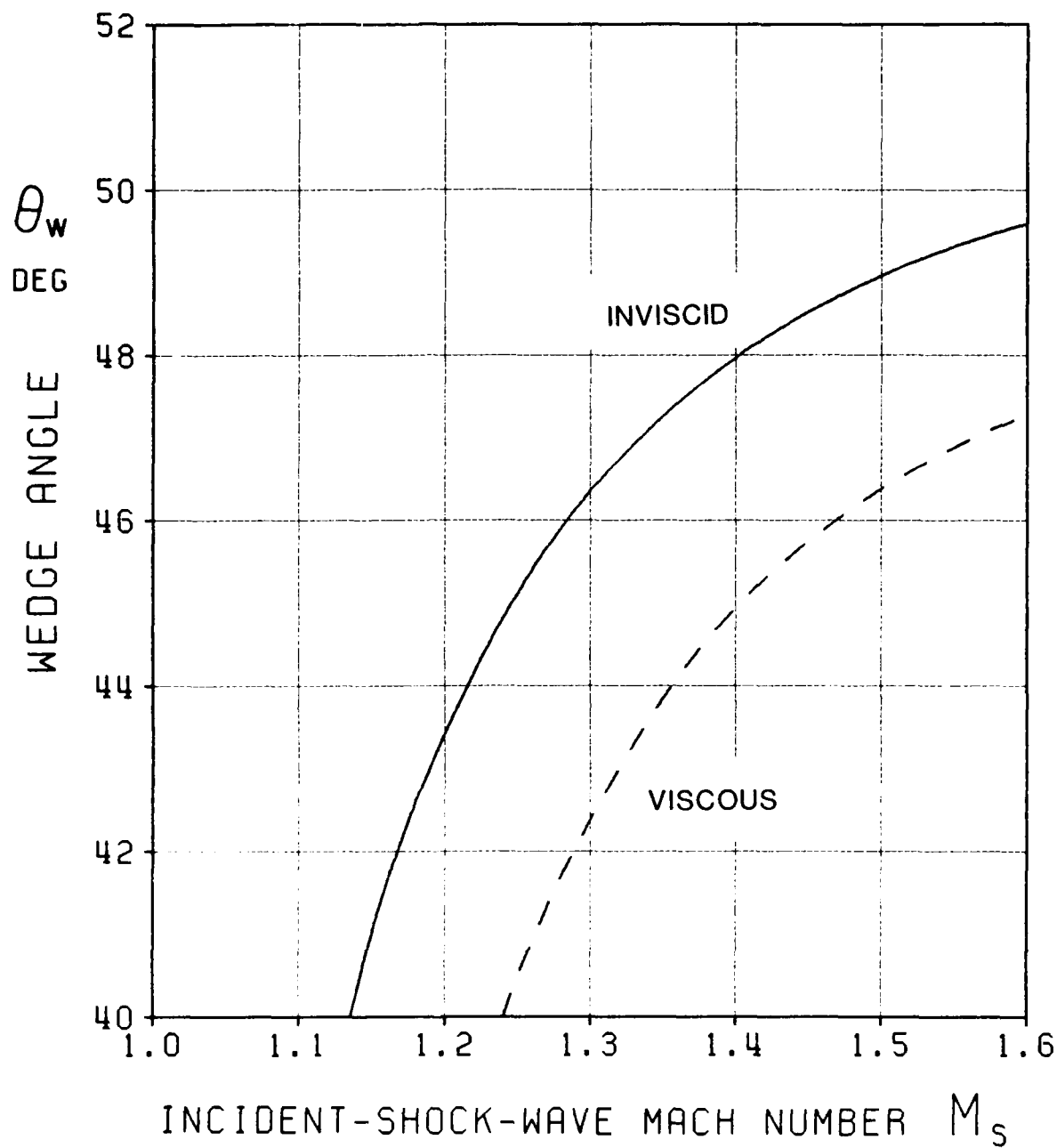
Figure 50a: Predicted viscous RR↔MR transition boundary
in air for initial pressure p_0 = 5.0 kPa
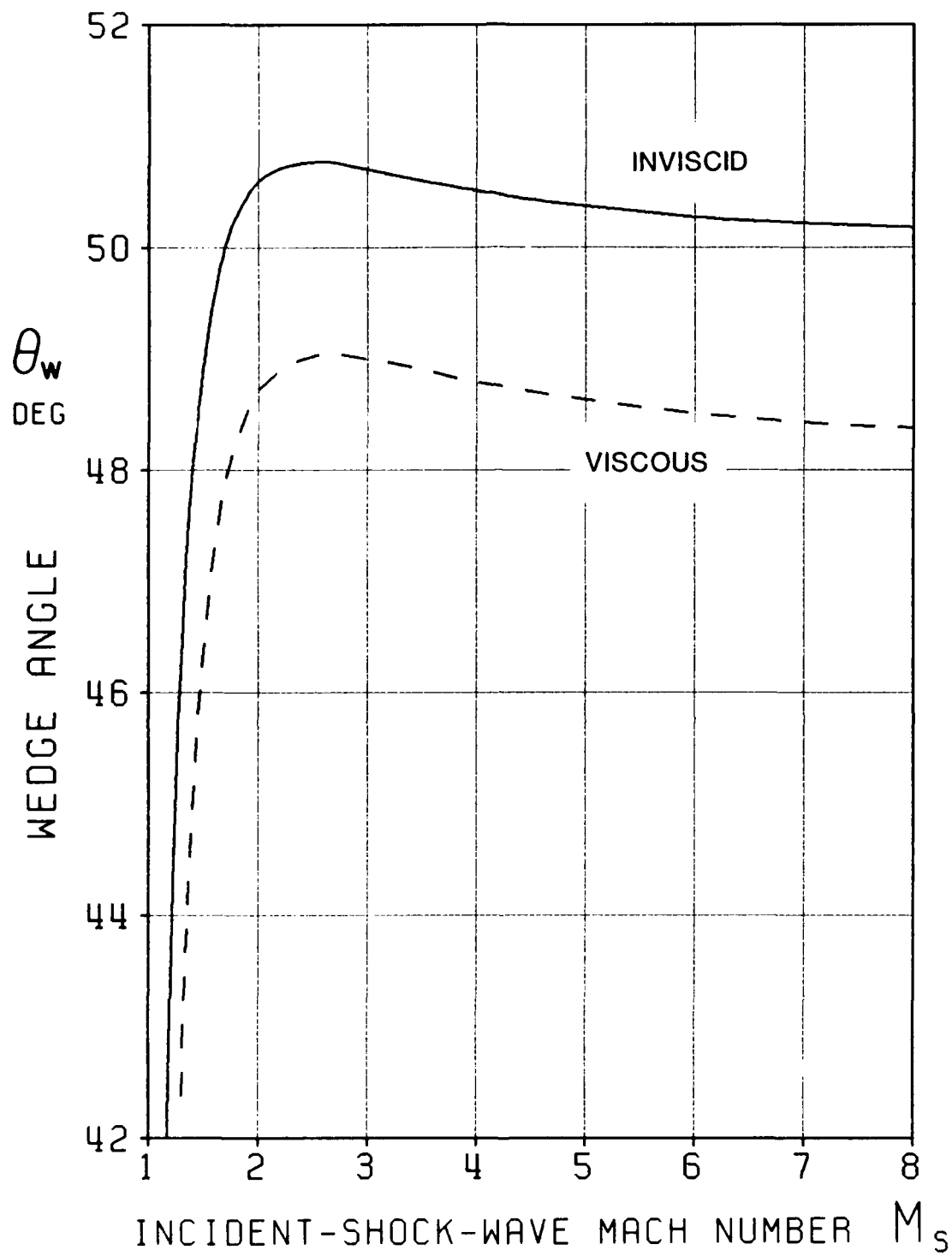
Figure 50b: Predicted viscous RR↔MR transition boundary
in air for initial pressure p_0 = 5.0 kPa
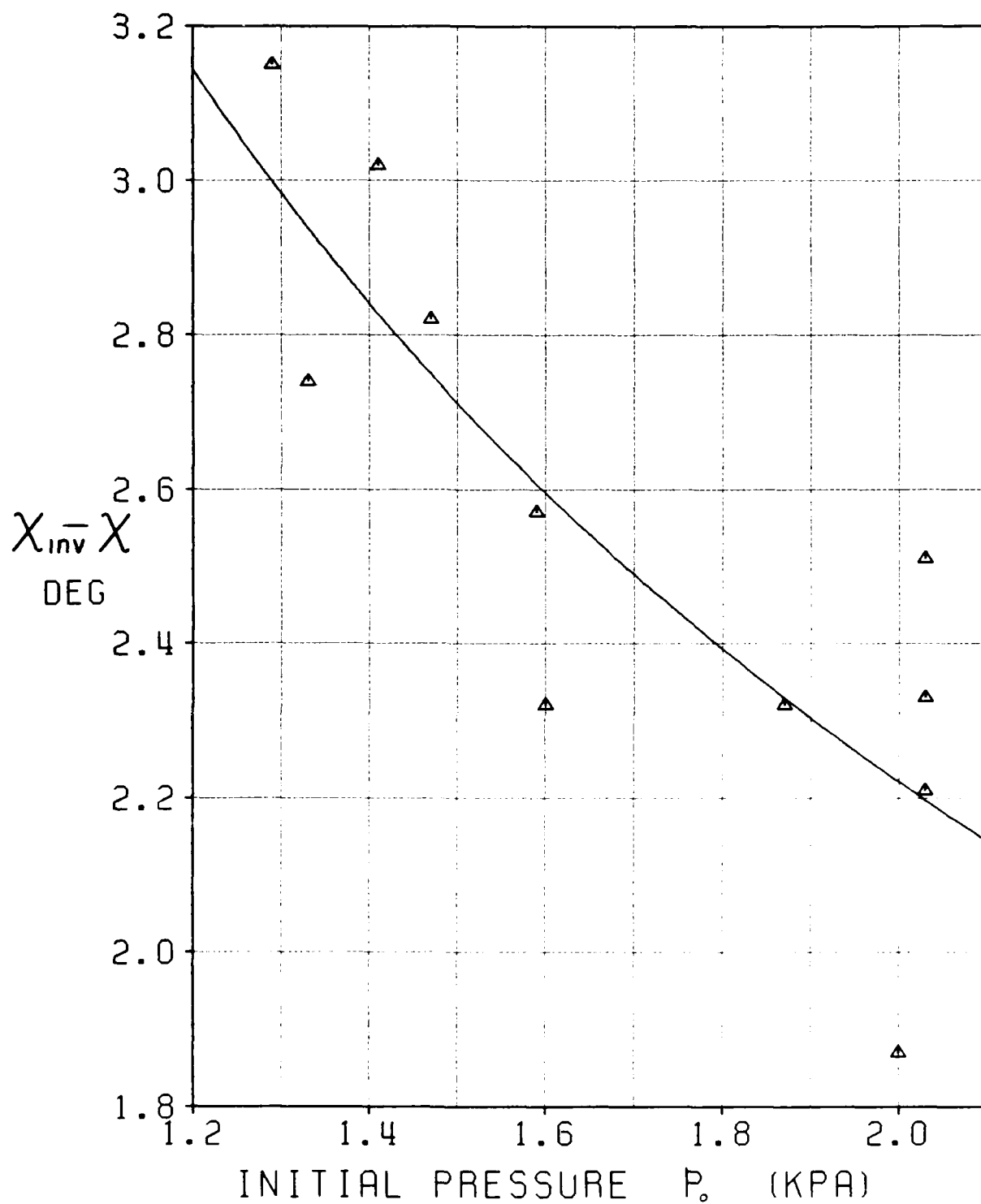
Figure 51:   Difference between analytic triple-point-trajectory
angle χ_{inv} and experimentally measured trajectory
angle χ for $\theta_w = 47°$

Figure 52: Difference between analytic triple-point-trajectory angle X_{inv} and experimentally measured trajectory angle X for $\theta_w = 48°$

Appendix A

SOLUTION OF FLOW FOR RR AND MR

The flow at an intersection of shock waves is readily calculated by applying the equations of motion across each of the waves, and using the proper boundary conditions. The frame of reference is fixed to the confluence point; triple point T in MR and reflection point P in RR. The equations of motion across a shock wave are (Figs. A-1 and A-2):

Continuity of tangential velocity:

$$U_i \cos(\phi_i) = U_j \cos(\phi_i - \theta_j) \qquad \text{(A.1)}$$

Conservation of mass:

$$\rho_i U_i \sin(\phi_i) = \rho_j U_j \sin(\phi_i - \theta_j) \qquad \text{(A.2)}$$

Momentum equation:

$$p_i + \rho_i U_i^2 \sin^2(\phi_i) = p_j + \rho_j U_j^2 \sin^2(\phi_i - \theta_j) \quad \text{(A.3)}$$

Conservation of energy:

$$h_i + \frac{1}{2} U_i^2 \sin^2(\phi_i) = h_j + \frac{1}{2} U_j^2 \sin^2(\phi_i - \theta_j) \quad \text{(A.4)}$$

where subscripts i and j refer to the regions upstream and downstream of the shock wave respectively.

The two necessary independent thermodynamic variables usually specified are p and T, thus giving ρ and h since the equations of state are given by:

$$\rho = \rho(p,T) \qquad \text{(A.5)}$$

$$h = h(p,T) \qquad \text{(A.6)}$$

If the gas is frozen, a closed-form solution exists.

For both RR and MR the following substitutions apply:

Incident shock wave	I:	$i = 0 \; ; \; j = 1$	(A.7)
Reflected shock wave	R:	$i = 1 \; ; \; j = 2$	(A.8)
Mach stem	M:	$i = 0 \; , \; j = 3$	(A.9)

(except $\phi_i = \phi_3$)

For clarity, these are illustrated in Fig. A-1 for the case of MR, and Fig. A-2 for RR.

The variables most often used to define the case under consideration are M_s and θ_w. The incident flow velocity and direction are calculated by attaching the frame of reference to point T in MR, or P in RR, and applying the gasdynamic equations and geometric relationships.

Solution of Flow at T in MR

The boundary conditions are:

$$P_2 = P_3 \qquad (A.10)$$

$$\theta_1 - \theta_2 = \theta_3 \qquad (A.11)$$

An additional constraint must be specified to solve the equations. It is assumed that at T, the Mach stem is perpendicular to the wedge surface.

One method of solution is:

1. Guess X and ω', and calculate the flow in region 0, relative to T.

2. Calculate the flow in region 1 by applying the equations of motion across I.

3. Calculate the flow in region 2 by applying the equations of motion across R.

A2

4. Calculate the flow in region 3 by applying the equations of motion across M.

5. Compare the flow direction and pressure in regions 2 and 3, and adjust X and ω' to try and achieve boundary conditions A.10 and A.11.

6. Repeat steps 2 through 5 until convergence is achieved.

It should be noted that in some areas of the (M_s, θ_w) plane, two solutions for MR can exist [44]. However, the one with lower value of X and ω' is the only one which occurs in practice.

Solution of Flow at P in RR

This configuration is illustrated in Fig. A-2. The only boundary condition is:

$$\theta_1 - \theta_2 = 0 \qquad\qquad (A.12)$$

The method of solution is very similar to that for T in MR.

1. Guess ω', and calculate the flow in region 0, relative to P.

2. Calculate the flow in region 1 by applying the equations of motion across I.

3. Calculate the flow in region 2 by applying the equations of motion across R.

4. Find the flow direction in region 2 and adjust ω' to try and achieve boundary condition A.12.

5. Repeat steps 3 to 4 until convergence is achieved.

Solutions for RR and MR over a wide range of Mach numbers and wedge angles were tabulated and plotted by Hu and Shirouzu [27].

Figure A-1: Schematic diagram of Mach reflection (MR)
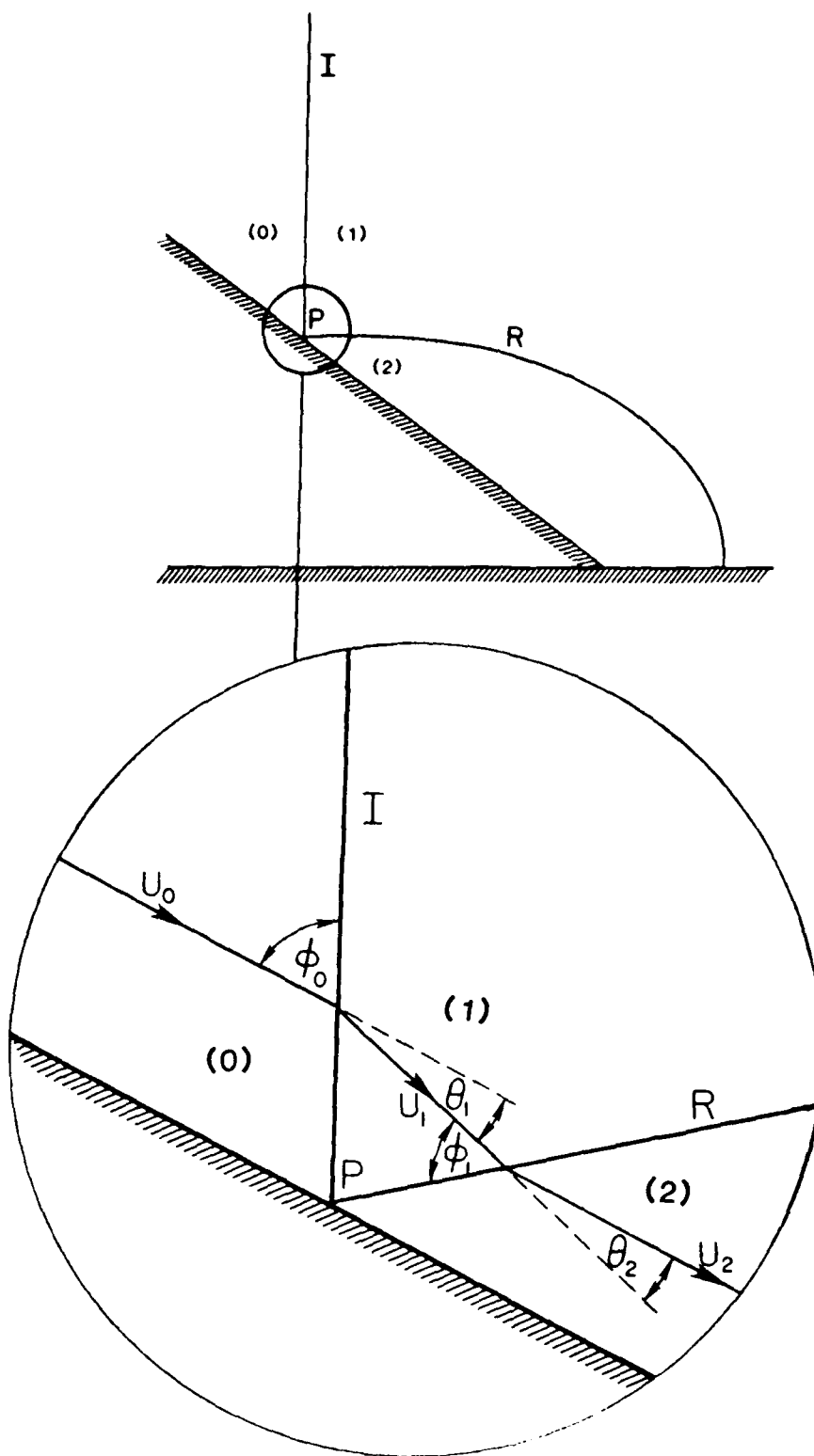
Figure A-2:   Schematic diagram of regular reflection (RR)

Computer Program to find the

RR→MR Transition Boundary in Frozen Air

```
C  *****************************************************************
C  *   THIS PROGRAM SOLVES FOR THE RR-MR TRANSITION BOUNDARY FOR FROZEN  *
C  *   AIR   IT CAN BE EASILY MODIFIED FOR OTHER FROZEN GASES.           *
C  *   OPTIONS ARE FOR THE DETACHMENT, SONIC, AND MECHANICAL EQUILIBRIUM *
C  *   CRITERIA.                                                         *
C  *   THE SHORT AND SIMPLE DESIGN ALLOWS IT TO BE TRANSLATED FOR A      *
C  *   MICROCOMPUTER, AND EXECUTION TIME IS MINIMAL.                     *
C  *****************************************************************
C
       REAL MS,MO,M1,M2
       COMMON G,R
       PI=3.141592654
       RADDEG=180.0/PI
C
C   THERMODYNAMIC GAS PROPERTIES
C
       R=8320.1/28.967
       G=1.400
C
C   OPTIONS
C
C       IOPT = 1      DETACHMENT CRITERION
C       IOPT = 2      SONIC CRITERION
C       IOPT = 3      MECHANICAL EQUILIBRIUM CRITERION
C
       READ(5,*) NCASE
       WRITE(6,100)
       DO 10 I=1,NCASE
C
C   THETAD IS THE DISPLACEMENT WEDGE ANGLE CAUSED BY THE
C   BOUNDARY-LAYER BEHIND THE INCIDENT SHOCK WAVE.
C   IT APPLIES ONLY TO THE SONIC AND DETACHMENT CRITERIA
C   TRANSITION BOUNDARIES.
C
       READ(5,*) MS,THETAD,IOPT
       IF(IOPT EQ 3) THETAD=0.0
       THETAD=THETAD/RADDEG
       IF(IOPT LE 2) CALL DETSON(MS,THETAW,THETAD,PHI1,IOPT)
       IF(IOPT EQ 3) CALL DETSON(MS,THETAW,0.0,PHI1,1)
       IF(IOPT EQ 3) CALL MECHEQ(MS,THETAW,PHI1,IOPT)
C
C   CALCULATE ALL THE THERMODYNAMIC STATES
C
       PHIO=PI/2.-THETAW
       MO=MS/SIN(PHIO)
       CALL OSWAVE(PHIO,MO,1.,1.,M1,P10,T10,THETA1)
```

```
          CALL OSWAVE(PHI1,M1,P10,T10,M2,P20,T20,THETA2)
          OMEGAP=PHI1-THETA1
C
C   SWITCH FROM RADIANS TO DEGREES AND OUTPUT THE DATA
C
          THETAW=THETAW*RADDEG
          PHIO=PHIO*RADDEG
          PHI1=PHI1*RADDEG
          THETA1=THETA1*RADDEG
          THETA2=THETA2*RADDEG
          THETAD=THETAD*RADDEG
          OMEGAP=OMEGAP*RADDEG
          WRITE(6,200) MS,THETAW,THETAD,IOPT,MO,PHIO,THETA1,M1,P10,T10,
         1PHI1,THETA2,M2,P20,T20,OMEGAP
   10     CONTINUE
          STOP
C
C
  100     FORMAT(1H1,///,T7,'MS',T13,'THETAW',T21,'THETAD',T30,'IOPT',
         1T41,'MO',T48,'PHIO',T55,'THETA1',T65,'M1',T72,'P1/PO',T80,'T1/TO',
         2T88,'PHI1',T95,'THETA2',T105,'M2',T112,'P2/PO',T120,'T2/TO',
         3T127,'OMEGAP',///)
  200     FORMAT(1H ,T5,F6.3,T13,F6.2,T21,F6.2,T32,I1,T39,F6.3,T47,F6.2,
         1T55,F6.2,T63,F6.3,T71,F6.2,T79,F6.2,T87,F6.2,T95,F6.2,T103,F6.2,
         2T111,F6.2,T119,F6.2,T127,F6.2)
          END
C
C  ***************************************************************************
C
          FUNCTION PHIM(M1)
C
C   THIS FUNCTION CALCULATES INCIDENCE ANGLE FOR MAXIMUM DEFLECTION
C   THROUGH THE SHOCK WAVE
C
          REAL M1
          COMMON G,R
          C1=(G+1.)/4.*(M1**2)-1.
          C2=SQRT((G+1.)*(1.+(G-1.)/2.*(M1**2)+(G+1.)/16.*(M1**4)))
          PHIM=ASIN(SQRT(1./G/(M1**2)*(C1+C2)))
          RETURN
          END
C
C  ***************************************************************************
C
          FUNCTION PHIS(M1)
C
C   THIS FUNCTION CALCULATES THE INCIDENCE ANGLE FOR SONIC FLOW
C   BEHIND THE SHOCK
C
          REAL M1
          COMMON G,R
          C1=(G+1.)/4.*(M1**2)-(3.-G)/4.
          C2=SQRT((G+1.)*((9.+G)/16.-(3.-G)/8.*(M1**2)+(G+1.)/16.*(M1**4)))
          PHIS=ASIN(SQRT(1./G/(M1**2)*(C1+C2)))
          RETURN
          END
```

B2

```
C
C      ****************************************************************
C
       SUBROUTINE OSWAVE(PHI1,M1,P1,T1,M2,P2,T2,THETA)
C
C  FLOW PROPERTIES ARE CALCULATED THROUGH A SHOCK WAVE
C
       REAL M1,M2,M1N,M2N
       COMMON G,R
       M1N=M1*SIN(PHI1)
       M2N=SQRT((2.+(G-1.)*(M1N**2))/(2.*G*(M1N**2)-G+1.))
       P2=P1*(2.*G/(G+1.)*(M1N**2)-(G-1.)/(G+1.))
       T2=T1*((1.+(G-1.)/2.*(M1N**2))/(1.+(G-1.)/2.*(M2N**2)))
       C1=(G+1.)/2.*(M1**2)/((M1N**2)-1.)-1.
       THETA=ATAN(1./C1/TAN(PHI1))
       M2=M2N/SIN(PHI1-THETA)
       RETURN
       END
C
C      ****************************************************************
C
       SUBROUTINE DETSON(MS,THETAW,THETAD,PHI1,IOPT)
C
C  THIS SUBROUTINE SOLVES FOR EITHER THE DETACHMENT OR SONIC CRITERION
C  THE FOLLOWING LOGIC IS USED:
C
C      1    SET THE MAXIMUM AND MINIMUM POSSIBLE VALUES FOR PHIO
C      2.   ITERATE ON PHIO BY BISECTING THE RANGE OF PHIO UNTIL
C           THE LIMIT OF RR IS REACHED, WHETHER IT BE THE LIMIT IMPOSED
C           BY THE DETACHMENT OR SONIC CRITERIA.
C
C
       REAL MS,MO,M1,M2
       COMMON G,R
       EXTERNAL PHIM,PHIS
       PI=3.141592654
       N=0
C
C  MINIMUM POSSIBLE VALUE FOR PHIO
       PHIOA=0.0
C  MAXIMUM POSSIBLE VALUE FOR PHIO
       PHIOB=PI/2
C
C  LOOK FOR BOUNDARY
C
   10  PHIOT=(PHIOA+PHIOB)/2.
       MO=MS/SIN(PHIOT)
       CALL OSWAVE(PHIOT,MO,1.,1.,M1,P1,T1,THETA1)
       IF(M1 GE 1.) GO TO 20
C  RR NOT POSSIBLE - PHIO TOO HIGH
       FUNCT=1.0
       GO TO 30
   20  PHI1=PHIM(M1)
       IF(IOPT EQ.2) PHI1=PHIS(M1)
       CALL OSWAVE(PHI1,M1,1.,1.,M2,P2,T2,THETA2)
       FUNCT=THETA1-THETA2-THETAD
```

B3

```
      N=N+1
      IF(N GT 20) GO TO 50
C
C   MAKE A NEW GUESS FOR PHIO USING THE BISECTION METHOD
C
   30 IF(FUNCT GT. 0. 0) THEN
      PHIOB=PHIOT
      ELSE
      PHIOA=PHIOT
      ENDIF
      GO TO 10
   50 THETAW=PI/2. -PHIOB
      RETURN
      END
C
C  *****************************************************************
C
      SUBROUTINE MECHEQ(MS, THETAW, PHI1, IOPT)
C
C   THIS SUBROUTINE SOLVES THE MECHANICAL EQUILIBRIUM CRITERION
C   THE FOLLOWING LOGIC IS USED:
C
C          1     SET THE MINIMUM AND MAXIMUM POSSIBLE VALUES FOR PHIO.
C          2.    CHECK TO SEE IF A SOLUTION IS POSSIBLE BY LOOKING
C                AT THE DETACHMENT CRITERION SOLUTION.
C                THIS POINT CORRESPONDS TO THE MAXIMUM POSSIBLE VALUE
C                FOR PHIO AT THE MECHANICAL EQUILIBRIUM BOUNDARY.
C          3     USE THE BISECTION METHOD TO GET A FIRST GUESS FOR
C                PHIO AT THE MECHANICAL EQUILIBRIUM BOUNDARY.
C          4     CALCULATE THE FLOW IN REGIONS 1 AND 3.
C                AND FLOW DEFLECTION THROUGH THE INCIDENT SHOCK.
C          5     ITERATE ON PHI1 UNTIL THE DEFLECTION THROUGH THE REFLECTED
C                SHOCK IS EQUAL AND OPPOSITE TO THAT THROUGH THE INCIDENT
C                SHOCK   USE A BISECTION METHOD.
C          6     COMPARE THE PRESSURES IN REGION 2 AND 3.
C          7     USING THE BISECTION METHOD, GET A NEW VALUE FOR PHIO
C                AND REPEAT STEPS 4 THROUGH 6 UNTIL CONVERGENCE IS
C                ACHIEVED
C
      REAL MS, MO, M1. M2, M3
      COMMON G, R
      EXTERNAL PHIM
      PI=3. 141592654
      N=0
C  MINIMUM POSSIBLE VALUE FOR PHIO
      PHIOA=0. 0
C  MAXIMUM POSSIBLE VALUE FOR PHIO, THE DETACHMENT CRITERION BOUNDARY
      PHIOB=PI/2 -THETAW
C
C   CHECK TO SEE IF A MECHANICAL EQUILIBRIUM SOLUTION EXISTS
C
      MO=MS/SIN(PHIOB)
      CALL OSWAVE(PHIOB, MO, 1 , 1., M1, P1, T1, THETA1)
      CALL OSWAVE(PI/2 , MO, 1 , 1 , M3, P3, T3, DUMMY)
      PHI1A=PHIM(M1)
      CALL OSWAVE(PHI1A, M1, P1, T1, M2, P2, T2, THETA2)
```

B4

```fortran
      IF(P3 LE P2) GO TO 10
      WRITE(6,*) 'NO MECHANICAL EQUILIBRIUM SOLUTION EXISTS AT',
     1   MS = ,MS
      IOFT=1
      RETURN
C
C   LOOK FOR THE BOUNDARY
C
  10  PHIOT=(PHIOA+PHIOB)/2
      MO=MS/SIN(PHIOT)
      CALL OSWAVE(PHIOT,MO,1 ,1 ,M1,P1,T1,THETA1)
      CALL OSWAVE(PI/2 ,MO,1 ,1 ,M3,P3,T3,THETA3)
C
C   SOLVE FOR PHI1 TO ACHIEVE NO NET DEFLECTION - USE BISECTION METHOD
C   TO ITERATE
C
      N2=0
C   MAXIMUM POSSIBLE VALUE OF PHI1
      PHI1A=PHIM(M1)
C   MINIMUM POSSIBLE VALUE OF PHI1
      PHI1B=ASIN(1 /M1)+.000001
  20  PHI1T=(PHI1A+PHI1B)/2.
      CALL OSWAVE(PHI1T,M1,P1,T1,M2,P2,T2,THETA2T)
      IF(ABS(THETA2T-THETA1) LT. 1.7E-05) GO TO 30
      IF(N2 GT.20) GO TO 40
      N2=N2+1
      IF(THETA2T GT THETA1) THEN
      PHI1A=PHI1T
      ELSE
      PHI1B=PHI1T
      ENDIF
      GO TO 20
C
C   CALCULATE A NEW VALUE FOR PHIO
C   USE THE BISECTION METHOD TO ITERATE
C
  30  CONTINUE
      FUNCT=P3-P2
      N=N+1
      IF(N.GT.20) GO TO 60
      IF(FUNCT.GT.0.0) THEN
      PHIOA=PHIOT
      ELSE
      PHIOB=PHIOT
      ENDIF
      GO TO 10
C
C   ERROR MESSAGES
C
  40  WRITE(6,*) 'NO CONVERGENCE - INNER LOOP OF MECHEQ'
      STOP
C
  60  THETAW=PI/2.-PHIOB
      PHI1=PHI1T
      RETURN
      END
```

Appendix C

THERMODYNAMIC PROPERTIES OF AIR

INCLUDING VIBRATIONAL EXCITATION

Each degree of freedom of a gas molecule contributes a share to the total energy of the molecule. The quantity of energy per unit mass from a fully excited degree of freedom is $RT/2$. For a frozen diatomic molecule such as O_2 or N_2, there are 3 translational and 2 rotational degrees of freedom. The energy per unit mass is therefore:

$$e_{t+r} = \frac{5}{2} RT \qquad \qquad (C.1)$$

It follows immediately that:

$$c_{v_{t+r}} = \left. \frac{\partial e}{\partial T} \right|_v = \frac{5}{2} R \qquad \qquad (C.2a)$$

$$c_{p_{t+r}} = c_{v_{t+r}} + R = \frac{7}{2} R \qquad \qquad (C.2b)$$

Therefore:

$$\gamma = \frac{c_p}{c_v} = \frac{7}{5} = 1.4 \qquad \qquad (C.2c)$$

for a frozen diatomic molecule.

However, diatomic molecules also have a vibrational energy mode, along the axis joining the two atoms. The energy per unit mass for a vibrational energy mode is:

$$e_v = RT \frac{z}{(e^z - 1)} \qquad \qquad (C.3a)$$

where

$$z = \frac{\theta_v}{T} \qquad \qquad (C.3b)$$

C1

θ_v is called the characteristic vibrational temperature and is unique for each gas. From Ref. 47:

$$\text{for } O_2: \qquad \theta_v = 2270 \text{ K}$$

$$\text{for } N_2: \qquad \theta_v = 3390 \text{ K}$$

Substitution of room temperature (293 K) into Eqns. C.3a and C.3b gives vibrational energies:

$$\text{for } O_2: \qquad e_v = 0.00335 \text{ RT}$$

$$\text{for } N_2: \qquad e_v = 0.00011 \text{ RT}$$

Virtually no vibrational excitation occurs at room temperature for air.

As a result of this additional vibrational energy, the specific heats also change.

$$c_{v_{t+r+v}} = c_{v_{t+r}} + R\, e^z \left(\frac{z}{e^z - 1}\right)^2 \qquad (C.4a)$$

$$c_{p_{t+r+v}} = R + c_{v_{t+r+v}} \qquad (C.4b)$$

Unlike the translational and rotational degrees of freedom, which become fully excited within a few mean free paths, vibrational equilibrium takes a relatively long time to occur. The rate of vibrational excitation decays exponentially to an equilibrium value. Because of the exponential nature of the excitation process, the relaxation time is defined as the time over which $1-1/e$ or 63.2% of the final excitation level is reached. It can be expressed as:

$$\tau = \frac{C_1}{p} \exp(C_2 T^{-1/3}) \qquad (C.5)$$

The values of C_1 and C_2 from two sources are listed in Table C-1. It is important to note that the relaxation time is inversely proportional to pressure, and much less dependent on temperature.

The relaxation lengths behind a normal shock wave in O_2 and N_2 are plotted in Figs. C-1 and C-2. A pressure of 2.0 kPa was chosen as a reference value for the plots, but correction for any other pressure can be made using Eq. C.5.

One might expect that the relaxation lengths for oxygen and nitrogen will differ when the two are mixed as in air. Since oxygen is affected before nitrogen, its vibrational mode is not affected much by collision with vibrating nitrogen molecules. As such, the relaxation length of oxygen is affected very little by the presence of nitrogen [45]. This is not true for nitrogen however. When nitrogen begins to become excited, the oxygen molecules are already vibrating, and their collision with the nitrogen molecules does change the relaxation length of nitrogen. Even with this change, the relaxation length of oxygen is still much shorter than that of nitrogen.

Table C-1

Empirical Constants in the
Vibrational-Relaxation-Time Equation (C.5)

Gas	C_1 (atm-μsec)	C_2 (Deg. $K^{1/3}$)	Temp. Range (Deg. K)	Ref.
O_2	2.92×10^{-4}	126	1000 – 3700	46
O_2	5.42×10^{-5}	143.4	800 – 3200	47
N_2	6.22×10^{-5}	202	3000 – 4500	46
N_2	7.12×10^{-3}	124.1	800 – 6000	47
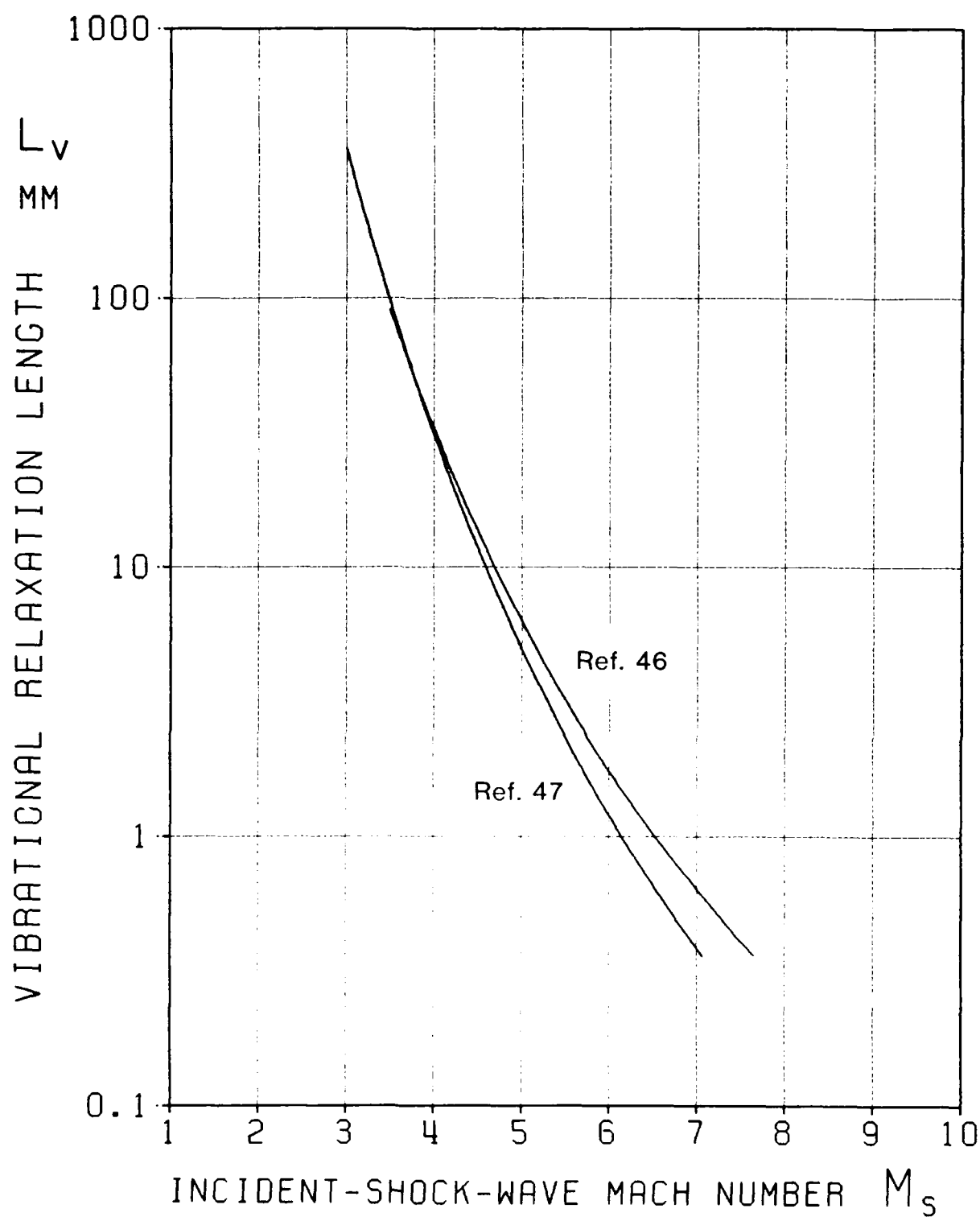
Figure C-1: Vibrational relaxation length of O_2 behind a normal shock wave with $T_0 = 300$ K and $p_0 = 2.0$ kPa
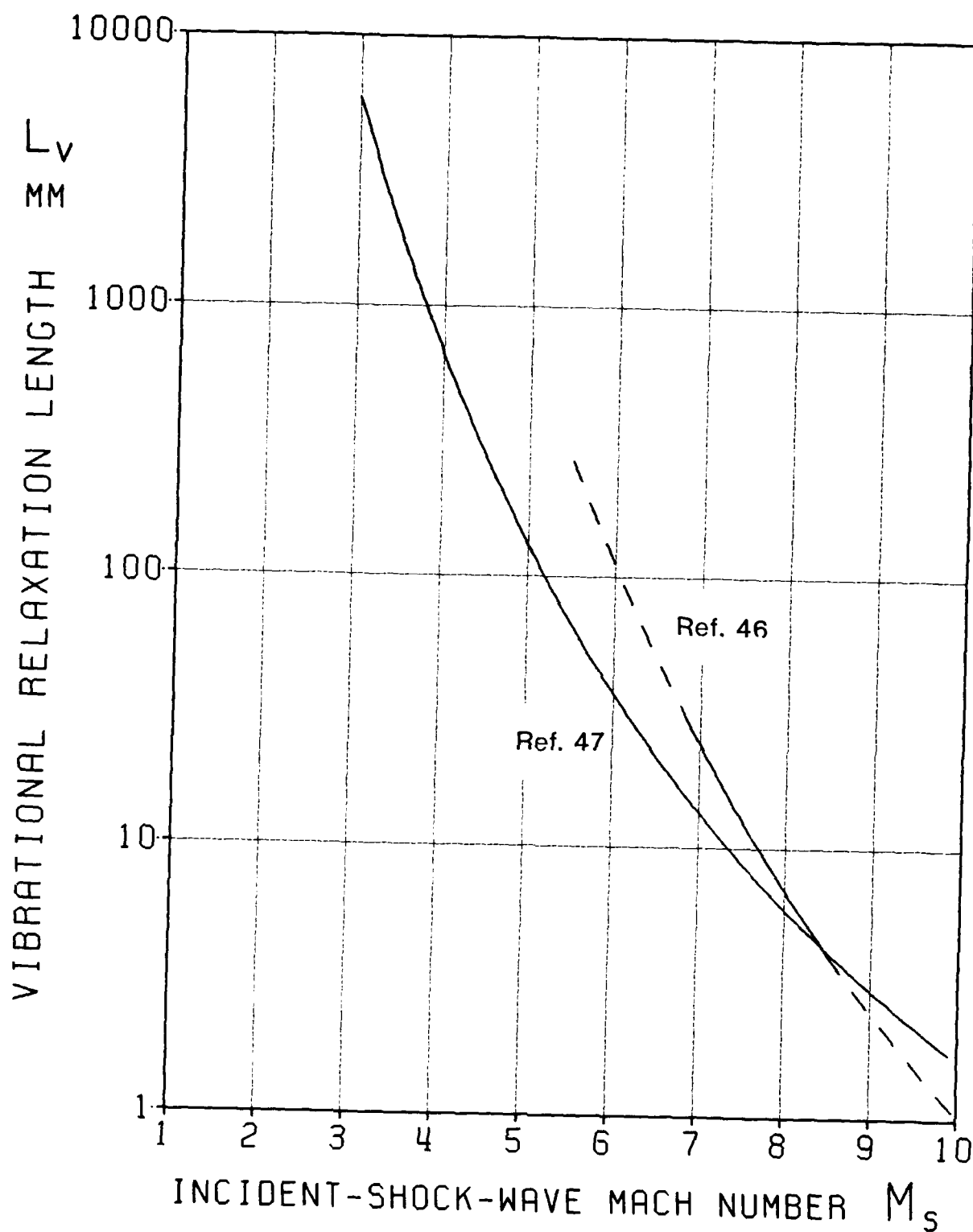
Figure C-2: Vibrational relaxation length of N_2 behind a normal shock wave with $T_0 = 300$ K and $p_0 = 2.0$ kPa

Appendix D

LAMINAR-BOUNDARY-LAYER EQUATIONS

This appendix outlines the basic technique used in calculating the boundary-layer profile behind a moving shock wave. This method of solution is based on work done by Mirels [37,38]. Recent, more precise methods of solution exist [48, 49] but were not used due to complexity. The reference frame is attached to the shock wave, as shown in Fig. D-1, so that the flow $(U_s - U_1)$ is steady, and the wall moves with a velocity U_s.

The equations which govern the flow in the boundary layer are the same as those for the external flow; continuity, momentum, energy and an equation of state. The boundary-layer equations include terms for viscosity μ and heat conduction k, and in this solution it is assumed that no pressure gradient exists. For a more general explanation of the equations and their physical meaning, see Schlichting [50].

The boundary layer equations are:

$$\frac{\partial}{\partial x}(\rho u) + \frac{\partial}{\partial y}(\rho v) = 0 \qquad \text{Continuity} \qquad (D.1)$$

$$u\frac{\partial u}{\partial x} + v\frac{\partial u}{\partial y} = \frac{1}{\rho}\frac{\partial}{\partial y}\left(\mu\frac{\partial u}{\partial y}\right) \qquad \text{Momentum} \qquad (D.2)$$

$$\rho c_p\left(u\frac{\partial T}{\partial x} + v\frac{\partial T}{\partial y}\right) = \frac{\partial}{\partial y}\left(k\frac{\partial T}{\partial y}\right) + \mu\left(\frac{\partial u}{\partial y}\right)^2 \qquad \text{Energy} \qquad (D.3)$$

$$p = \rho RT \qquad \text{Equation of State} \qquad (D.4)$$

with boundary conditions:

$$u(x,0) = u_w \qquad (D.5a)$$

$$u(x,\infty) = u_e \qquad (D.5b)$$

$$v(x,0) = 0 \qquad (D.5c)$$

$$T(x,0) = T_w \qquad (D.5d)$$

$$T(x,\infty) = T_e \qquad (D.5e)$$

D1

Since the flow is continuous, a stream function ψ exists such that

$$\frac{\partial \psi}{\partial y} = \frac{\rho u}{\rho_r} \qquad (D.6a)$$

$$-\frac{\partial \psi}{\partial x} = \frac{\rho v}{\rho_r} \qquad (D.6b)$$

Introduce a similarity parameter

$$\eta = \sqrt{\frac{u_e}{2x\nu_r}} \int_0^y \frac{T_r}{T}\, dy \qquad (D.7)$$

and rewrite the stream function

$$\psi = \sqrt{2u_e x\nu_r}\; f(\eta) \qquad (D.8)$$

It should be noted that

$$\frac{u}{u_e} = f' \qquad (D.9a)$$

$$\frac{v}{u_e} = -\frac{T}{T_r}\sqrt{\frac{\nu_r}{2xu_e}}\left(f + 2xf'\,\frac{\partial \eta}{\partial x}\right) \qquad (D.9b)$$

As a simplification, it is assumed that the viscosity and the thermal conductivity are directly proportional to the temperature.

$$\mu = \frac{\mu_r}{T_r}\, T \qquad (D.10a)$$

$$k = \frac{k_r}{T_r}\, T \qquad (D.10b)$$

The choice of reference temperature for viscosity and thermal conductivity is somewhat arbitrary at this point. A wise choice of reference temperature may minimize error caused by this simplification [38], and will be discussed later.

When equations D.8, D.9, and D.10 are substituted into the momentum equation, it becomes

$$f'' + ff''' = 0 \tag{D.11}$$

with boundary conditions

$$f(0) = 0 \tag{D.11a}$$

$$f'(0) = u_w/u_e \tag{D.11b}$$

$$f'(\infty) = 1 \tag{D.11c}$$

Substitution of equations D.9, D.9, and D.10 into the energy equation yields:

$$T'' + \sigma f T' = -\sigma (\lambda-1) M_e^2 (f'')^2 \tag{D.12}$$

assuming the Prandtl number σ is constant.

From equation D-12, the temperature distribution can be expressed as

$$\frac{T}{T_e} = 1 + \frac{\gamma-1}{2}\left[\left(\frac{u_w}{u_e} - 1\right) M_e\right]^2 r(\eta) + \left(\frac{T_w - T_{w,i}}{T_e}\right) s(\eta) \tag{D.13}$$

where $r(\eta)$ satisfies

$$r'' + \sigma f r' = -\frac{2\sigma}{\left(\frac{u_w}{u_e} - 1\right)^2} (f'')^2 \tag{D.14}$$

$$r'(0) = 0 \tag{D.14a}$$

$$r(\infty) = 0 \tag{D.14b}$$

$s(\eta)$ satisfies

$$s'' + \sigma f s' = 0 \tag{D.15}$$

$$s(0) = 1 \tag{D.15a}$$

$$s(\infty) = 0 \tag{D.15b}$$

and

$$\frac{T_{w,i}}{T_e} = 1 + \frac{\gamma-1}{2}\left[\left(\frac{u_w}{u_e} - 1\right) M_e\right]^2 r(0) \tag{D.16}$$

D3

The temperature distribution is in fact a combination of 2 solutions; the solution for the case of an insulated wall, plus one for addition of heat transfer through the wall. $T_{w,i}$ is the temperature which would occur at the wall if it were insulated, and $r(0)$ is a recovery factor for the recovery temperature T_r at the wall, which is less than the adiabatic total temperature.

To get y in terms of η, equations D.7 and D.13 are combined, giving

$$y = \sqrt{\frac{2x\nu_r}{u_e}} \; \frac{T_e}{T_r} \left\{ \eta + \frac{\gamma-1}{2} \left[\left(\frac{u_w}{u_e} - 1 \right) M_e \right]^2 \int_0^\eta r \, d\eta + \frac{T_w - T_{w,i}}{T_e} \int_0^\eta s \, d\eta \right\} \qquad (D.17)$$

Another parameter of interest is

$$\delta^\star = 2x \frac{T_e}{T_r} \sqrt{\frac{\nu_r}{2xu_e}} \left\{ \lim_{\eta \to \infty} (\eta - f) + \frac{\gamma-1}{2} \left[\left(\frac{u_w}{u_e} - 1 \right) M_e \right]^2 \int_0^\eta r \, d\eta \right.$$

$$\left. + \frac{T_w - T_{w,i}}{T_e} \int_0^\eta s \, d\eta \right\} \qquad (D.18)$$

The distribution of $\delta^\star$ with axial distance is of the form:

$$\delta^\star = C_1 \, x^{\frac{1}{2}} \qquad (D.19)$$

The angle at which flow enters the boundary layer is determined by the rate at which $\delta^\star$ grows. The boundary-layer flow entry angle is defined by:

$$\tan(\theta_{bl}) = \frac{d}{dx}(\delta^\star) = \frac{1}{2} C_1 \, x^{-\frac{1}{2}} \qquad (D.20)$$

Solution of equations D.11 to D.11c and D.14 to D.15b gives a non-dimensional profile of the boundary layer. The rest of the equations can then be applied to get velocity and temperature profiles.

The wall temperature used is that of the wall before the shock passes. This was shown to be quite valid [38] as the conductivity of the wall is much higher than that of the air, and the wall acts as a large heat sink.

Viscosity and heat conduction do not vary linearly with temperature and the assumption that they do will only be approximate. To minimize the effects of this approximation, a specific reference temperature is used. The reference temperature

$$T_r = 0.5 \ (T_w + T_e) + 0.22 \ (T_{w,i} - T_e) \qquad (D.19)$$

will minimize the error in heat transfer and shear stress at the wall [38].

The method of solution for the non-dimensional profiles is as follows:

1. Solve for the distribution of f

   (a) Set boundary conditions D.11a and D.11b for f(0) and f'(0)

   (b) Guess f''(0) and use a Runge-Kutta method to integrate equation D.11 from $\eta = 0$ to $\eta = 6$ ($\eta = 6$ is a close approximation to $\eta = \infty$)

   (c) Compare f(6) to boundary condition D.11c

   (d) Repeat steps b and c until convergence is achieved

2. Solve for the distribution of r

   (a) Set f(0), f'(0), f''(0) obtained in step 1

   (b) Set boundary condition D.14a for r'(0)

   (c) Guess r(0) and use a Runge-Kutta method to integrate equations D.11 and D.14 from $\eta = 0$ to $\eta = 6$.

   (d) Compare r(6) to boundary condition D.14b

   (e) Repeat steps c and d until convergence is achieved.

3. Solve for the distribution of s

   (a) Set f(0), f'(0), f''(0) obtained in step 1

   (b) Set boundary condition D.15a for s(0)

   (c) Guess s'(0) and use a Runge-Kutta method to integrate equations D.11 and D.15 from $\eta = 0$ to $\eta = 6$.

   (d) Compare s(6) to boundary condition D.15b

   (e) Repeat steps c and d until convergence is achieved.

The complete Fortran program for the solution of the boundary layer equations is listed in Appendix E.
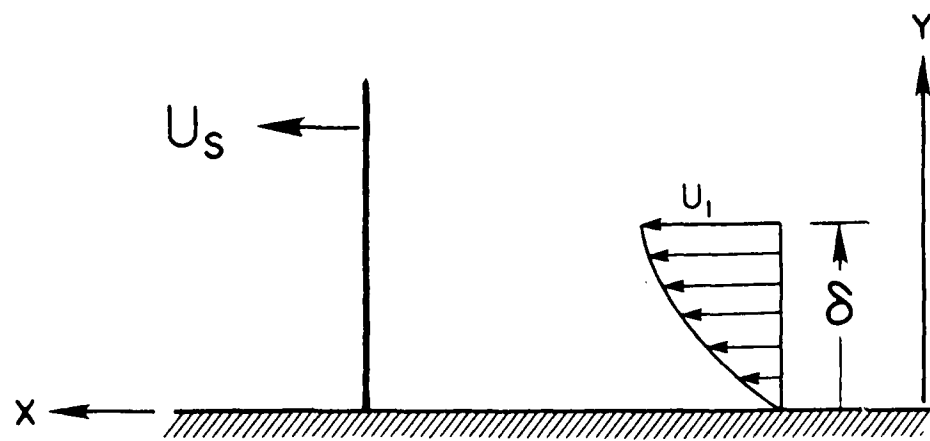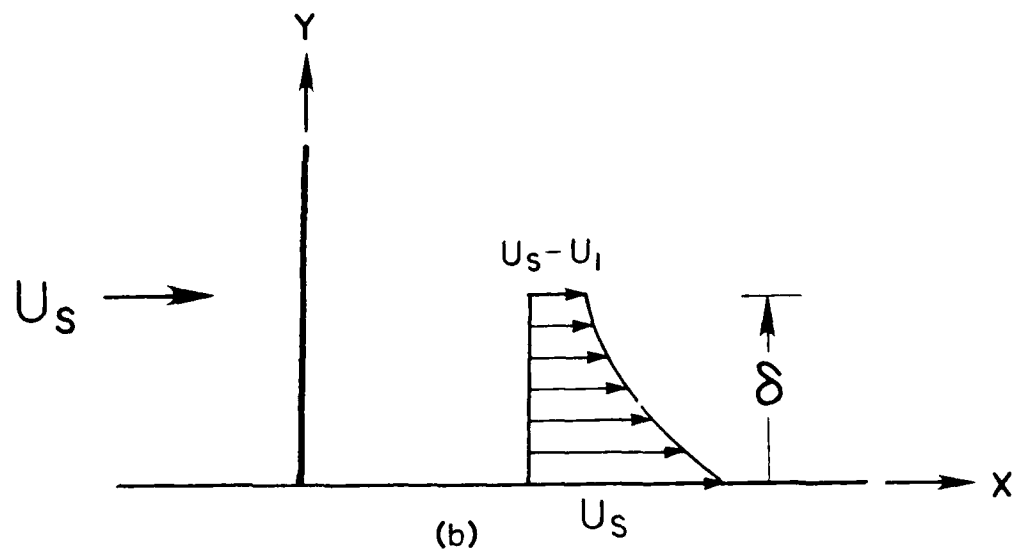
Figure D-1: Laminar-boundary-layer velocity distribution in
two different reference frames

(a) Laboratory-fixed reference frame

(b) Shock-fixed reference frame

Computer Program for the Solution of the

Laminar-Boundary-Layer Equations

```
      SUBROUTINE BLAYER(PE, TE, UE, TW, UW, REYN, DELTA, DELSTAR, THETAD,
     1IOUT)
C
C  THIS SUBROUTINE SOLVES FOR THE BOUNDARY LAYER BEHIND A PLANE
C  NORMAL SHOCK WAVE MOVING INTO STILL AIR
C  IT IS BASED ON NACA TN 3401 AND NACA TN 3712 BY H. MIRELS
C
      REAL ME, NUW, NUREF, A(301,6)
      REAL Y(5), WK(100), BLP(301,7)
      INTEGER IWK(5)
      COMMON /C/ PR, C1
      EXTERNAL FCN, FCNJ
C
C  INITIALIZE DATA
C
      PR=0 72
      C1=0 0
      RAIR=287 074
      GAIR=1 4
      PW=PE
C  CLENGTH IS AN ARBITRARILY CHOSEN CHARACTERISTIC LENGTH
      CLENGTH=1 0E-03
C
C  CALCULATE SOME FLOW PROPERTIES
C
      AE=SQRT(GAIR*RAIR*TE)
      ME=UE/AE
      RHOE=PE/RAIR/TE
      RHOW=PW/RAIR/TW
      NUW=VISCO(TW)/RHOW
      UWUE=UW/UE
C
C  ******** SOLUTION OF BOUNDARY LAYER DIFFERENTIAL EQUATIONS
C
C  Y(1) = F
C  Y(2) = F
C  Y(3) = F''
C  Y(4) = R  OR S  DEPENDING ON WHICH IS BEING SOLVED FOR
C  Y(5) = R' OR S' DEPENDING ON WHICH IS BEING SOLVED FOR
C
C  ***********************************************
C  * SOLVE FOR THE DISTRIBUTION OF F *
C  ***********************************************
C
      L=0
C
```

```fortran
C    INITIALIZE DATA FOR IMSL SUBROUTINE 'DGEAR'
C    'DGEAR' INTEGRATES THE BOUNDARY LAYER EQUATIONS USING RUNGE-KUTTA
C
C    H, N, TOL, METH, AND MITER ARE PARAMETERS FOR 'DGEAR'
C
      N=5
      TOL=.000001
      METH=2
      MITER=3
C
C    SET THE INITIAL CONDITIONS
C
C    FPPZ IS F"(0)
C
      FPPZ=-0.124425*(UWUE**2)-0.77505*UWUE+1.0287
   10 X=0.0
      Y(1)=0.0
      Y(2)=UWUE
      Y(3)=FPPZ
      Y(4)=0.0
      Y(5)=0.0
      H=.000001
      INDEX=1
C
C    SOLVE FOR F-PRIME AT INFINITY (FPI)
C
      DO 20 I=1,300
      XEND=.02*I
      CALL DGEAR(N,FCN,FCNJ,X,H,Y,XEND,TOL,METH,MITER,INDEX,IWK,WK,IER)
   20 IF(IER.NE.0) WRITE(6,*) 'IER IS ',IER
C
      FPPZNEW=FPPZ
      FPINEW=Y(2)
      IF(IOUT.EQ.2) WRITE(6,*) 'FPINEW IS ',FPINEW,FPPZ
      L=L+1
      IF(L.GT.15) STOP
      IF(L.GT.1) GO TO 30
      FPPZ=FPPZNEW+0.05
      GO TO 40
C
C    CALCULATE A NEW F"(0) -- FPPZ
C
   30 IF(ABS(FPINEW-1.0).LT.1.0E-05) GO TO 100
      FPPZ=FPPZNEW+(1.0-FPINEW)/(FPINEW-FPIOLD)*(FPPZNEW-FPPZOLD)
   40 FPPZOLD=FPPZNEW
      FPIOLD=FPINEW
      GO TO 10
C ************************************
C * SOLVE FOR THE DISTRIBUTION OF R  *
C ************************************
C
C
  100 L=0
      C1=-2.0*FP/((UWUE-1.)**2)
```

```
C
C    INITIALIZE DATA FOR IMSL SUBROUTINE 'DGEAR'
C
      N=5
      TOL=.000001
      MCTH=2
      MITER=3
C
C    SET THE INITIAL CONDITIONS
C
C    RZ IS R(0)
C
      RZ=-0.000625*(UWUE**2)+0.01155*UWUE+0.8799
 110  X=0.0
      Y(1)=0.0
      Y(2)=UWUE
      Y(3)=FPPZ
      Y(4)=RZ
      Y(5)=0.0
      H=.000001
      INDEX=1
C
C    SOLVE FOR R AT INFINITY (RI)
C
      DO 120 I=1,300
      XEND=.02*I
      CALL DGEAR(N,FCN,FCNJ,X,H,Y,XEND,TOL,METH,MITER,INDEX,IWK,WK,IER)
C    STORE THE NON-DIMENSIONAL BOUNDARY LAYER PARAMETERS FOR LATER USE
      BLP(I+1,1)=Y(1)
      BLP(I+1,2)=Y(2)
      BLP(I+1,3)=Y(3)
      BLP(I+1,4)=Y(4)
      BLP(I+1,5)=Y(5)
 120  IF(IER.NE.0) WRITE(6,*) 'IER2 IS ',IER
C
      RZNEW=RZ
      RINEW=Y(4)
      IF(IOUT.EQ.2) WRITE(6,*) 'RINEW IS ',RINEW,RZNEW
      L=L+1
      IF(L.GT.15) STOP
      IF(L.GT.1) GO TO 130
      RZ=RZNEW+0.05
      GO TO 140
C
C    CALCULATE A NEW R AT ZERO (RZ)
C
 130  IF(ABS(RINEW-0.0).LT.1.0E-05) GO TO 200
      RZ=RZNEW+(0.0-RINEW)/(RINEW-RIOLD)*(RZNEW-RZOLD)
 140  RZOLD=RZNEW
      RIOLD=RINEW
      GO TO 110
C
```

```
C  ************************************
C  * SOLVE FOR THE DISTRIBUTION OF S *
C  ************************************
C
  200   REC=RZ
        L=0
        C1=0.0
C
C   INITIALIZE DATA FOR IMSL SUBROUTINE 'DGEAR'
C
        N=5
        TOL=.000001
        METH=2
        MITER=3
C
C   SET THE INITIAL CONDITIONS
C
C   SPZ IS S'(0)
C
        SPZ=0.006725*(UWUE**2)-0.17255*UWUE-0.533
  210   X=0.0
        Y(1)=0.0
        Y(2)=UWUE
        Y(3)=FPPZ
        Y(4)=1.0
        Y(5)=SPZ
        H=.000001
        INDEX=1
C
C   SOLVE FOR S AT INFINITY (SI)
C
        DO 220 I=1,300
        XEND=.02*I
        CALL DGEAR(N,FCN,FCNJ,X,H,Y,XEND,TOL,METH,MITER,INDEX,IWK,WK,IER)
        BLP(I+1,6)=Y(4)
        BLP(I+1,7)=Y(5)
  220   IF(IER.NE.0) WRITE(6,*) 'IER3 IS ',IER
C
        SPZNEW=SPZ
        SINEW=Y(4)
        IF(IOUT.EQ.2) WRITE(6,*) 'SINEW IS ',SINEW,SIOLD,SPZ
        L=L+1
        IF(L.GT.15) STOP
        IF(L.GT.1) GO TO 230
        SPZ=SPZNEW+0.05
        GO TO 240
C
C   CALCULATE A NEW S-PRIME AT ZERO (SPZ)
C
  230   IF(ABS(SINEW-0.0).LT.1.0E-05) GO TO 300
        SPZ=SPZNEW+(0.0-SINEW)/(SINEW-SIOLD)*(SPZNEW-SPZOLD)
  240   SPZOLD=SPZNEW
        SIOLD=SINEW
        GO TO 210
  300   CONTINUE
C
```

E4

```
C    LOAD THE BLP MATRIX FOR THE ROW CORRESPONDING TO ETA = 0
C
       BLP(1,1)=0.0
       BLP(1,2)=UWUE
       BLP(1,3)=FPPZ
       BLP(1,4)=REC
       BLP(1,5)=0.0
       BLP(1,6)=1.0
       BLP(1,7)=SPZ
C
       IF(IOUT.NE.2) GO TO 320
C
C    OUTPUT THE MATRIX OF NON-DIMENSION BOUNDARY LAYER PARAMETERS
C
       DO 310 I=1,301,5
       ETA=.02*(I-1)
       WRITE(6,1000) ETA,(BLP(I,J),J=1,7)
 310   CONTINUE
C
C
C    ********************************************************************
C    * USE BOUNDARY LAYER PROFILE TO DO CALCULATIONS *
C    ********************************************************************
C
C
C    INITIALIZE SOME OF THE BOUNDARY LAYER PARAMETERS
C
 320   RDN=0.0
       SDN=0.0
       YOLD=0.0
       C1=(GAIR-1.)/2.*((UWUE-1.)*ME)**2
       TWI=TE*(1.+C1*REC)
C
C    REFERENCE TO A MEAN TEMPERATURE TO GET A BETTER SOLUTION
C    SEE NACA TN 3712
C
       TREF=0.5*(TW+TE)+0.22*(TWI-TE)
       RHOREF=RHOE*TE/TREF
       NUREF=VISCO(TREF)/RHOREF
C
C    CALCULATE THE BOUNDARY LAYER DATA
C
       DO 400 K=2,301
       ETA=.02*(K-1)
       FP=BLP(K,2)
       R=BLP(K,4)
       S=BLP(K,6)
       RDN=RDN+(BLP(K,4)+BLP(K-1,4))/2.*.02
       SDN=SDN+(BLP(K,6)+BLP(K-1,6))/2.*.02
C
       T=TE*(1.+C1*R+(TW-TWI)/TE*S)
       RHO=RHOE*TE/T
       C2=TE/TREF*(ETA+C1*RDN+(TW-TWI)/TE*SDN)
       YNEW=SQRT(2.*NUREF/UE)*C2
       DY=YNEW-YOLD
       YOLD=YNEW
```

```
        U=UE*FP
        C3=(U-UW)/(UE-UW)
        IF(C3 LT. .99) N=K
C
C   LOAD UP THE OUTPUT ARRAY - WHILE CALCULATING Y AT CHAR. LENGTH
C
        A(K,1)=ETA
        A(K,2)=YNEW*SQRT(CLENGTH)
        A(K,3)=U
        A(K,4)=T
        A(K,5)=C3
        A(K,6)=(T-TW)/(TE-TW)
  400   CONTINUE
C
C   LOAD THE OUTPUT ARRAY FOR THE ROW CORRESPONDING TO ETA = 0
C
        A(1,1)=0.0
        A(1,2)=0.0
        A(1,3)=UW
        A(1,4)=TW
        A(1,5)=0.0
        A(1,6)=0.0
        IF(IOUT.EQ.2) WRITE(6,*) 'RDN AND SDN ARE ',RDN,SDN
C
C   CALCULATE DELTASTAR AT X = 1MM
C
        DELSTAR=2.0*CLENGTH*TE/TREF*SQRT(NUREF/2./CLENGTH/UE)
       1*(ETA-BLP(301,1)+C1*RDN+(TW-TWI)/TE*SDN)
C
C   CALCULATE DELTA AND REYNOLDS NUMBER
C
        DELTA=(.99-A(N,5))/(A(N+1,5)-A(N,5))*(A(N+1,2)-A(N,2))+A(N,2)
        REYN=CLENGTH*(UW-UE)/NUW
C
C   NOW TO CALCULATE THE DISPLACEMENT ANGLE
C   IT WILL BE A POSITIVE NUMBER BY CONVENTION
C
        THETAD=-0.5*ATAN(DELSTAR/CLENGTH)
C
        IF(IOUT.EQ.0) RETURN
C
C   FULL OUTPUT OF BOUNDARY LAYER PROFILE
C
        WRITE(6,2000)
        WRITE(6,2100) UE,TE
        WRITE(6,2200) UW,TW
        WRITE(6,2300) UWUE,TREF
        WRITE(6,2400) UE+AE
        WRITE(6,2500) REYN
        WRITE(6,2550) -DELSTAR*1000.
        WRITE(6,2600) THETAD*57.2958
        WRITE(6,2700)
        WRITE(6,2800)
        WRITE(6,2900)
C
```

E6

```
         DO 410 K=1,301,5
  410    WRITE(6,3000) A(K,1),A(K,2)*1000 ,A(K,3),A(K,4),
        1A(K,2)/DELTA,A(K,5),A(K,6)
C
C
         RETURN
C
C
C    FORMAT STATEMENTS
C
1000     FORMAT(1H ,F4.1,7(5X,F7.4))
2000     FORMAT(1H1,'***BOUNDARY LAYER PROFILE DATA*** --- VERSION 3',/)
2100     FORMAT(1H ,'UE    = ',F7.1,' M/SEC',T42,'TE = ',F7.1,' DEG K')
2200     FORMAT(1H ,'UW    = ',F7.1,' M/SEC',T42,'TW = ',F7.1,' DEG K')
2300     FORMAT(1H ,'UW/UE =    ',F4.2,T40,'TREF = ',F7.1,' DEG K')
2400     FORMAT(1H ,'UE+AE = ',F7.1,' M/SEC')
2500     FORMAT(1H0,'REYNOLDS NUMBER (L=1MM) = ',E9.4)
2550     FORMAT(1H0,'DISPLACEMENT THICKNESS    (L=1MM) = ',F5.4,' MM')
2600     FORMAT(1H ,'DISPLACEMENT WEDGE ANGLE (L=1MM) = ',F6.3,' DEG')
2700     FORMAT(/,1H ,'           ETA           Y           U   ',
        1'           T           Y           U-UW        T-TW')
2800     FORMAT(   1H ,                         '(MM)        (M/SEC)',
        1'          (DEG K)         DELTA       UE-UW       TE-TW')
2900     FORMAT(1H ,' ------------------------------------------------',
        1'-----------------------------------------------')
3000     FORMAT(1H ,8X,F3.1,10X,F6.5,6X,F7.1,6X,F7.1,10X,F6.4,6X,F6.4,
        16X,F6.4)
C
         END
C
C    'FCN' DEFINES THE EQUATIONS TO BE SOLVED BY 'DGEAR'
C
         SUBROUTINE FCN(N,X,Y,YPRIME)
         COMMON /C/ PR,C1
         INTEGER N
         REAL Y(N),YPRIME(N),X
         YPRIME(1)=Y(2)
         YPRIME(2)=Y(3)
         YPRIME(3)=-Y(1)*Y(3)
         YPRIME(4)=Y(5)
         YPRIME(5)=C1*Y(3)**2-PR*Y(1)*Y(5)
         RETURN
         END
C
C
C    'FCNJ' IS A DUMMY SUBROUTINE FOR THE SOLVER 'DGEAR'
C
         SUBROUTINE FCNJ(N,X,Y,PD)
         INTEGER N
         REAL Y(N),PD(N,N)
         RETURN
         END
C
```

```fortran
      REAL FUNCTION VISCO(TEMP)
C
C  THIS CALCULATION USES EQUATION 68 FROM NASA TECHNICAL REPORT
C  TR R-50
C
      VISCO=1.462E-06*SQRT(TEMP)/(1.+112./TEMP)
C
      RETURN
      END
```

END
1-81
DTIC